predictive mineral discovery
COOPERATIVE RESEARCH CENTRE

pmd*CRC

Final Report

Targeting new mineral deposits in western Victoria

Project T1

editor: C.J.L Wilson

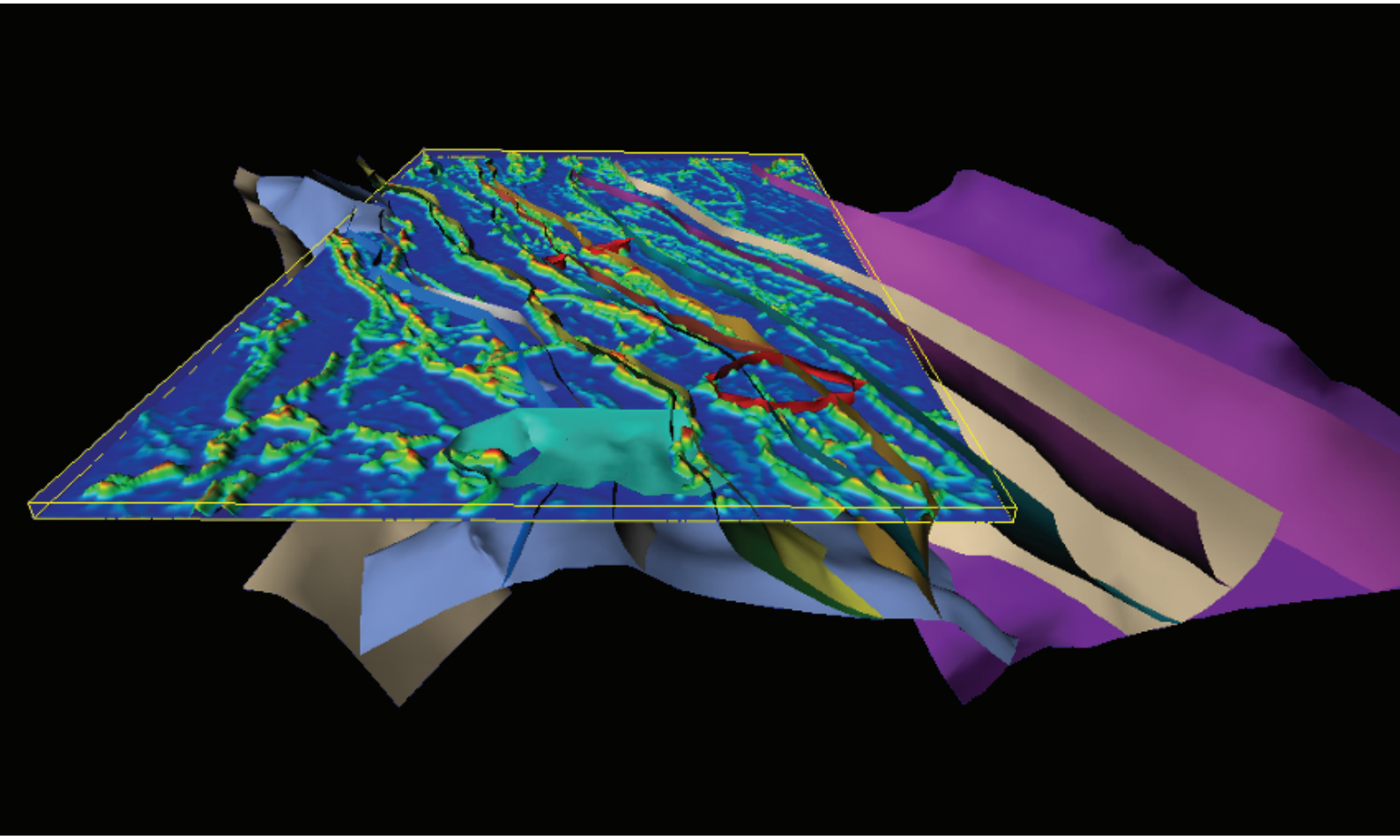

CSIRO
AMIRA INTERNATIONAL
Australian Government
Geoscience Australia
MONASH University
THE UNIVERSITY OF MELBOURNE
JCU James Cook University
THE UNIVERSITY OF WESTERN AUSTRALIA

Project T1 - Targeting new mineral deposits in western Victoria

Final Report (2001 to 2005)

August 2005

The ***pmd****CRC* T1 project was set up in 2001 with the following initial aim:

To create realistic 3D and 4D models of the sub-surface geology and fluid flow history of the Stawell Belt at various scales in order to develop and refine methodologies for ore-body targeting and help predict the location of major ore.

Role	Name	Affiliation
Program Coordinator	Dr Russell Korsch	Geoscience Australia
Team Leader	Prof Chris Wilson	University of Melbourne
Industry Leader	Jon Dugdale	Leviathan Resources (MPI Mines)
Team Members	Dr Tim Rawling	University of Melbourne
	Dr Barry Murphy	University of Melbourne
	Dr Peter Schaubs	CSIRO Mining and Exploration
	Dr John Miller	University of Melbourne
	Dr Bob Musgrave	Monash University
	Marta Vega	La Trobe University
Industry Contributors	Robert Smith	Greenfields Geophysics
	Kim Frankcombe	Southern Geoscience Consultants
	Bruce Godsmark	Leviathan Resources
	Darren Holden	Fractal Geosciences (Fractal Graphics)
	Don Emerson	Systems Exploration
Government Contributor	Ross Cayley	Geoscience Victoria
Honours Students	Julia Grewar (2004)	University of Melbourne
	Lawrence Leader (2004)	University of Melbourne
	Daniel Henry (2004)	University of Melbourne

Table of Contents

T1 : Targeting new mineral deposits in western Victoria

Executive Summary

C.J.L. Wilson

Introduction

Western Victoria is host to several world class sediment-hosted gold deposits (e.g. Stawell, Ballarat, Bendigo) that have been studied on an individual basis, generally without reference to a well-constrained regional structural and stratigraphic framework. The configuration and availability of fluid conduits (shear zones or other structural settings and appropriate host lithologies) over time is clearly an important factor in the formation of these mineral deposits but the distribution and profiles of fluid pathways with increasing crustal depth are often imprecisely known. It is also probable that the mineralising fluids were not locally sourced, but travelled long distances from their point of origin, making it imperative that all potential fluid conduits be mapped in 3D so that any sub-surface linkages or networks of fluid pathways be identified. These pathways then need to be incorporated into the 3D regional framework so that the key conduits and structures can be further investigated to establish their precise role in either controlling or sustaining fluid flow over geological time scales appropriate for the formation of a major ore-body. The Stawell Zone in western Victoria is ideally placed for such a case study because it contains sequences that relate to the mineralisation types found in Tasmania and those identified in central Victoria and NSW.

Project goals and deliverables

The TI project is a predictive mineral discovery Cooperative Research Centre (pmd*CRC) collaborative project between University of Melbourne, CSIRO Exploration and Mining and MPI Mines (later Leviathan Resources Limited). The principal goal of the T1 project was to integrate field, geochronological and geophysical data in a collaborative effort, to develop 3 and 4-dimensional geological models of the crust at a range of scales to predict the location of new mineral deposits in western Victoria.

In order to achieve the primary pmd*CRC project goal, four key deliverables were designed:

- Establish links between structural studies of crustal rock associations to sub-surface geophysical data. In particular how aeromagnetic/gravity anomalies were related to mineralisation processes by empirical and theoretical rock-magnetic (magnetic petrophysics) studies of rocks from mineralised versus non-mineralised;
- Petrophysics interpretation of magnetics and gravity data:
- Develop 3-dimensional predictive models of the crust on three scales:

(1) Drillcore scale petrophysics - Magnetic susceptibility, density, electrical properties, radiometrics, seismic properties.
(2) Prospect scale trials - electrical methods and detailed gravity.
(3) Prospect and larger scale modelling - of magnetics and gravity.
(4) Larger scale - "Worming" images of gravity/magnetic data sets, teleseismic tomography and seismic interpretation and modelling of deeper crustal structure in western Victoria (from Delamarian Orogen to Avoca Fault).

- Fluid flow modelling of hydrothermal processes to predict key fluid flow sites at the time of mineralisation on three scales:
  (1) Prospect scale– 3-dimensional.
  (2) Belt scale – 2- and 3-dimensional.
  (3) Regional scale – 2- and 3-dimensional

How does the project fit with CRC vision

This project focused on an entire mineralising system with a strategy of understanding some "type localities" within the Stawell Corridor in order to understand the processes that operate at crustal or lithospheric scale in western Victoria. Addressing the problem of ore-body formation at this scale requires integration of regional data-sets from multiple sources and disciplines into one seamless whole to produce a 4D model. Understanding the 3D architecture of the mineralising system in combination with geochronology are the key to identifying which geological elements are critical for ore formation and where it is likely to occur in western Victoria. This multidisciplinary project drew together researchers from a wide range of disciplines and backgrounds, including academia, exploration industry and the Victorian Geological Surveys, in line with CRC goals and aspirations. In order to build a coherent model for the Stawell Belt there was an integration of different data inputs, 3D models and fluid flow models as in the flow chart below:

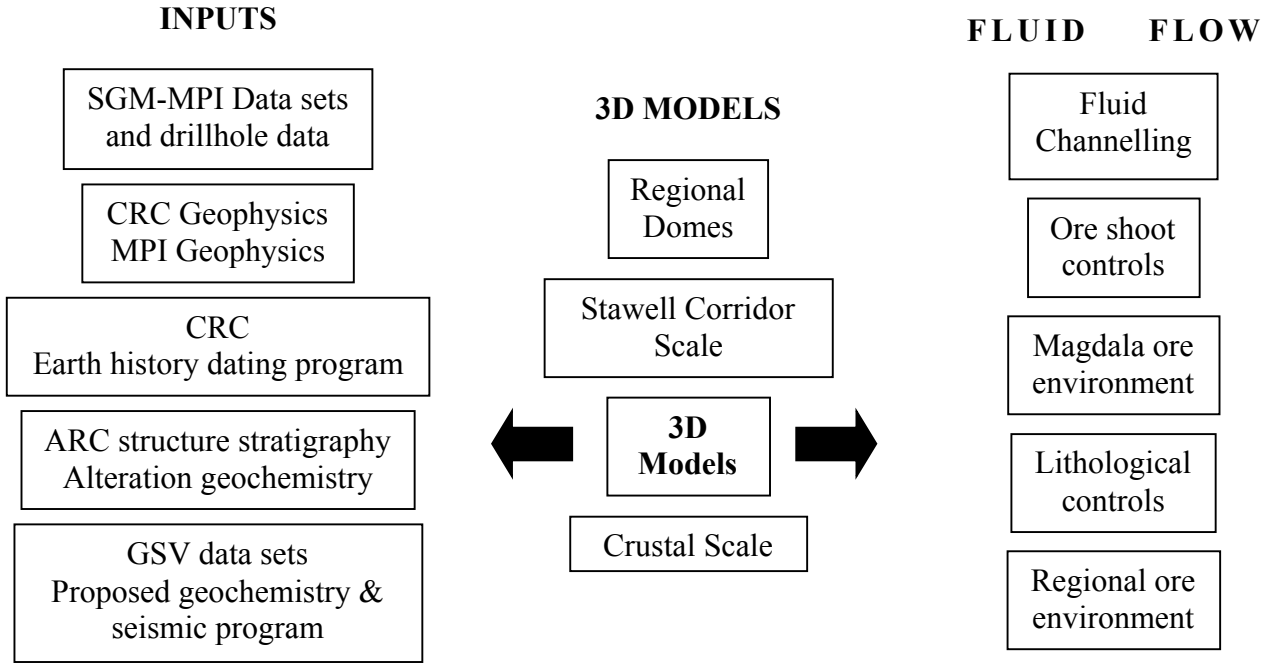

The problem being addressed

Western Victoria is host to several world class sediment-hosted gold deposits (e.g. Stawell, Ballarat, Bendigo) that have been studied on an individual basis, generally without reference to a well-constrained regional structural and stratigraphic framework. The configuration and availability of fluid conduits (shear zones or other structural settings and appropriate host lithologies) over time is clearly an important factor in the formation of these mineral deposits but the distribution and profiles of fluid pathways with increasing crustal depth are often imprecisely known. It is also probable that the mineralising fluids were not locally sourced, but travelled long distances from their point of origin, making it imperative that all potential fluid conduits be mapped in 3D so that any sub-surface linkages or networks of fluid pathways be identified. These pathways then need to be incorporated into the 3D regional framework so that the key conduits and structures can be further investigated to establish their precise role in either controlling or sustaining fluid flow over geological time scales appropriate for the formation of a major ore-body. The Stawell Zone in western Victoria is ideally placed for such a case study because it contains sequences that relate to the mineralisation types found in Tasmania and those identified in central Victoria and NSW.

The gold orebodies at Stawell are predominantly hosted by sulphide and iron-chlorite altered sedimentary rocks formerly known as the "volcanogenics" now termed the Magdala Facies (Dugdale & Wilson, submitted) that envelope a 1km wide dome-like basalt extrusion, the Magdala Basalt. Surrounding the Magdala Facies are less altered turbidites of the Albion Formation and overlying Leviathan Formation (formerly the Eastern Schist, Mine Schist, and Wonga Schist of Watchorn and Wilson, 1989). In this final report both the new and old lithostratigraphical units will used. The main gold lodes at Stawell formed during the 440Ma mineralisation event and were subsequently off-set by a series of faults. In reconstructing the geological models the effect of this faulting has been carefully removed and is based on the observations described in Miller & Wilson (2002; 2004). At the start of this project there was a recognition that the Stawell ore-body (>6 million ounces of gold endowment) is part a large gold system that is situated within a geological corridor, interpreted via aeromagnetics, to continue under Murray Basin cover the north. This lead the MPI (Leviathan) exploration team to embrace new ways to reduce the time and cost to discovery through the multidisciplinary approach undertaken during this project.

Project achievements

The pmd*CRC project operated for a little over three years, and in this time interacted with the H4 *pmd**CRC History project to establish absolute timing relationships in the Stawell Zone. The T1 research project was funded by MPI Mines Limited and by the *pmd**CRC as a "Flagship Project" and this final report brings together a vast wealth of new knowledge, information and data, and is accompanied by a DVD that presents the 3D- Models developed for western Victoria. Results have been collated and presented in this volume as a series of papers that will be supplemented with a further series of papers from a complimentary ARC-Linkage Project; together these papers will be published as a thematic issue of the *Australian Journal of Earth Sciences in 2006*.

The report is structured around the application of multi-disciplinary predictive techniques that have resulted in the discovery of at least two new mineralised systems

under barren cover, at Wildwood and Kewell. Chapter 1 sets the geophysical scene that has been used in interpreting the geology and building the 3D models. Chapter 2 summarises some of the petrophysical results and implications for interpretation of aeromagnetic anomalies. Chapter 3 shows that the most important control on the formation of the Stawell ore-bodies is the geometry and properties of the Magdala Basalt dome and its effect on the localisation of hydrothermal fluid flow during the ore forming hydrothermal event. Chapter 4 elaborates on the workflow and correlation of modelling results with real geometries that have been used to construct the 3D models both on a mine scale and regionally. Chapter 5 describes a crustal-scale model for western Victoria. Chapter 6 summarises structural mapping and the use of 2.75 forward modelling to constrain the 3D geometry of regionally significant faults.

The T1 project was a learning exercise for all involved and as the current mine at Stawell provided the best geological constraints on the origin of the gold shoots, this was selected as the first test area and will be described in detail in Chapters 3 and 4. Where "Dome scale" modelling was used to simulate zones of enhanced fluid flow that matches the overall distribution of the Magdala and Golden Gift ore shoots (Figure 1).

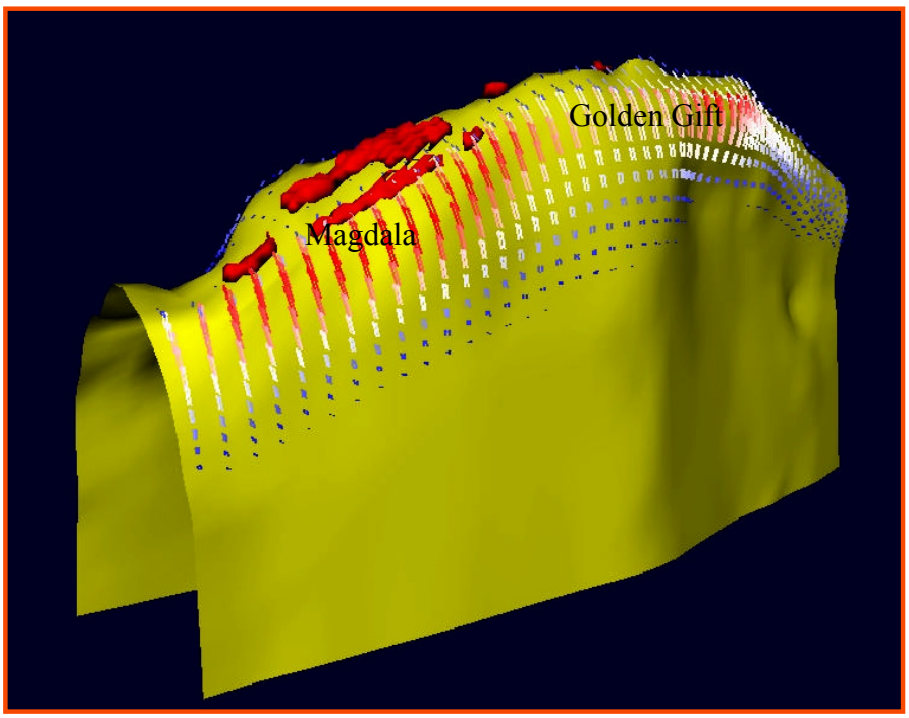

Figure 1: Interpretation of the Magdala dome prior to any post-mineralisation faulting, viewed from the west. Arrows represent predicted fluid flow vectors and red zones represent dilation sites.

It was recognised by the Leviathan Resources exploration group that successful exploration for other buried domes within the Stawell Corridor would require a well researched predictive model. The first stage in the development of regional predictive models for new ore systems in western Victoria was the characterisation of the key geological elements of the Stawell ore system. Additional geophysical data was collected over key prospects. In particular, detailed gravity data proved an effective filter for basalt domes versus other magnetic features. Inversion modelling of gravity

and magnetics assisted construction of 3-dimensional basalt dome models. 3D models were then constructed for numerical simulation modelling of fluid flow and dilation at the time of mineralisation on surfaces that were restored to geometries that existed prior to any post-mineralisation faulting (Chapters 3 and 4). Stress orientations and rock properties were as determined through previous and concurrent ARC funded research. The combined results of ENE-WSW + E-W compression, based on Stawell structural history (Miller & Wilson 2002; 2004) simulated high fluid flow on the upper shoulders of the domes, particularly the shallow plunging WSW flank and steeply plunging ENE flank (e.g. Figure 2). Predicted dilation was concentrated on the upper shoulders of the dome. The intersection of these areas of high fluid flow and dilation with the eroded Murray Basin interface is a 1.6km long zone on the SW flank and a smaller zone on the northern end of the Kewell basalt (Figure 2). These zones are coincident with elevated aircore geochemistry.

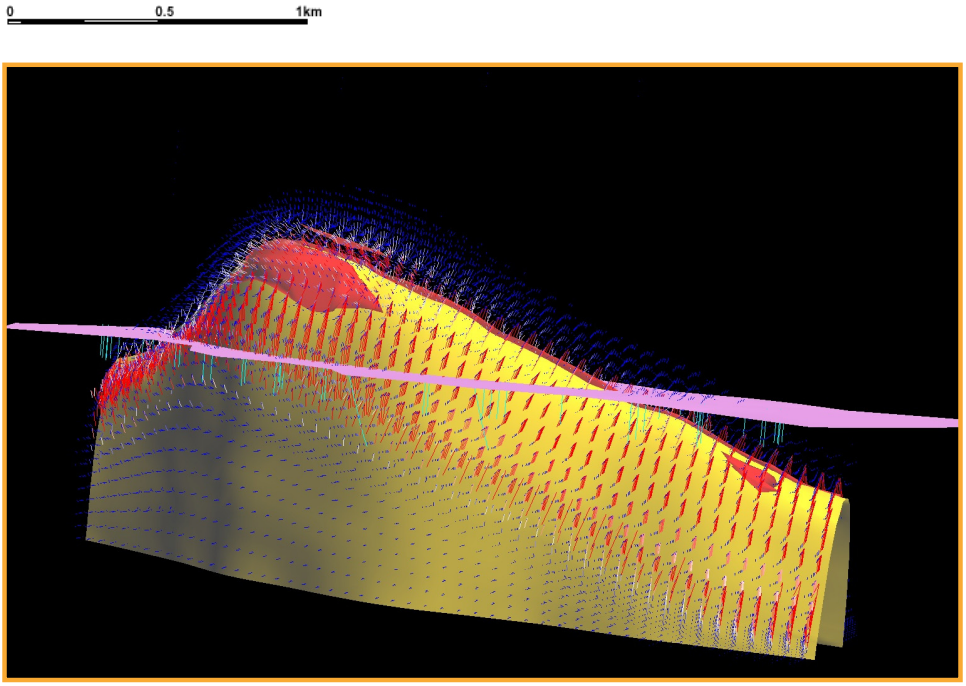

Figure 2: Interpretation of the Kewell dome prior to any post-mineralisation faulting, viewed looking north. Yellow surface is the basalt, red surface are shear strain contours, red arrows represent predicted fluid flow vectors, mauve surface is ground level and green lines are drill holes.

The results of the geochemical characterization (through an ARC project) and fluid flow/dilation modelling were combined to produce specific diamond drilling targets. The first target selected for drilling was the southern end of the Kewell dome on section 5967600mN (Figure 3). Drill hole KD003 intersected a brecciated quartz lode followed by a thick section of mineralised volcanogenics including a basalt bound "Waterloo" with visible gold, on a shallow west dipping basalt contact. Intersections included 4.2m @ 3.46 g Au/t from the hangingwall lode and 4.1m @ 12.6 g Au/t from the Waterloo (Figure 3). Subsequent drilling results included 6.25m @ 10.2 g Au/t in KD005 (Figure 3).

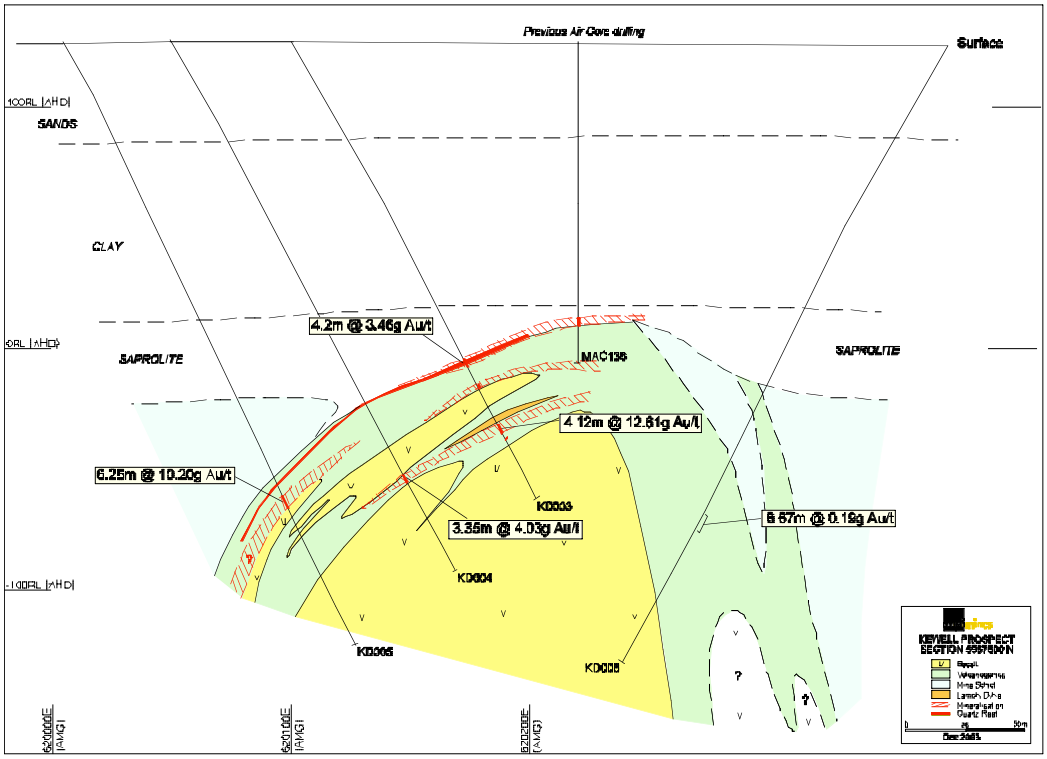

Figure 3: Interpretation of the Kewell dome December 2004 in section 5967600mN.

Similar modelling and targeting has also been undertaken at the Wildwood prospect with initial results including an intersections in WRC076 of 10m @ 12.7g Au/t. Further drilling is in progress and time will tell whether Kewell and Wildwood are significant new discoveries. However, these are example of a step change in an exploration strategy with a significant reduction in time and cost to discovery through a multidisciplinary approach to predictive mineral discovery.

The question of the crustal architecture and whether there are deep penetrating faults along which mineralised fluids could enter the western Victorian crust has been tackled via a 3D geological model (Chapter 5). Embedded within this are existing gold deposits, prospects and targets. Through a combination of geophysical forward modelling (as in Chapter 6), numerical simulation and existing seismic data, the 3D model was developed to inform the explorationist on prioritising resource opportunities in the region. The model largely affirms the major boundaries, as determined by the GSV mapping, some changes in fault positions are warranted (e.g. the Moyston Fault, south of Stawell) and there are changes in emphasis regarding the relative dominance of some structures – for example, the Pleasant Creek Fault is modelled as a major break that significantly impacts on the 3D architecture as much as, if not more than, the Moyston Fault.

The Coongee Fault, being a locus for gold mineralisation, represents a major steep west-dipping boundary, separating low grade from substantially high grade metamorphic rocks to the west. In the model, it appears to have formed as a back-thrust to a major ramp developed in the basal detachment geometry. It has undergone later strike slip sinistral reactivation.

References

Dugdale A.L. & Wilson C.J.L. Hydrothermal alteration of an atypical turbidite-hosted orogenic gold deposit: the Magdala system, Stawell, western Victoria, Australia, *Australian Journal of Earth Sciences,* submitted.

Miller, J. McL. and Wilson. C.J.L., 2002. The Magdala Lode System, Stawell, southeastern Australia: structural style and relationship to gold mineralisation across the western Lachlan Fold Belt. *Economic Geology* **97**, 325-349.

Miller, J. McL. and Wilson. C.J.L., 2004. Application of structural analysis to faults associated with a heterogeneous stress history: the reconstruction of a dismembered gold deposit, Stawell, western Lachlan Fold Belt, Australia. *Journal of Structural Geology*, **26**, 1231-1256.

Squire R.J. & Wilson C.J.L., 2005. Interaction between collisional orogenesis and convergent-margin processes: evolution of the Cambrian proto-Pacific margin of East Gondwana. *Journal of the Geological Society of London*, **162** 749-761.

Acknowledgements

The team leader thanks all the T1 *pmd**CRC team members for their hard work, perseverance and enormous contributions over the 4 years of the project. We acknowledge the support of the pmd*CRC in funding and promoting this "Flagship" project. The project would not have come together without the strong support of Jon Dugdale, Geoff McDermott, the Stawell geological team and John Rowe's initial support. The project has come a long way after a very slow start and our early attempts at coming to grips with the problems and putting together 3D data with geological concepts.

The support of the Directors of MPI Mines and Leviathan Resources in providing financial support and encouragement to undertake this project is gratefully acknowledged. Stawell Gold Mines are thanked for providing access to all available datasets and locations and for having the confidence in the results of this work to drill the proposed targets thus testing the validity of the process. Carol Durant is also thanked for her capable and invaluable efforts in providing us with digital data sets and our requests for sections.

Chapter 1: The role of geophysical methods applied to mapping mineral systems under the Murray Basin cover.

R.J. Smith and K. Frankcombe

Summary

This paper reviews the role that geophysical methods have played in mapping mineral systems beneath Murray Basin cover, in the Stawell corridor of western Victoria. North of Stawell, the Stawell corridor has been shown to extend more than 100 Km to the north-northwest, beneath increasing thicknesses of Murray Basin sediments. Based on a geological model developed at Stawell, geophysical methods have played an essential role in mapping new mineral systems in the belt beneath this transported cover. Regional geophysical data (principally magnetics and gravity) has been supplied by GeoScience Victoria and supplemented by company surveys for more detail in selected areas. In addition, various electrical methods have been tested for direct detection of mineralisation beneath deep conductive cover. The results have led to the detection of several mineralised systems many kilometres from outcrop, and with no surface expression. Petrophysical measurements on core samples and geophysical logging of drillholes have been essential to the interpretation of geophysical data and they have also contributed to further understanding of the mineralising processes.

Introduction

The Stawell Goldfield is situated about 245 Km northwest of Melbourne within the Delamarian Fold Belt (Miller *et al*. submitted). Most gold production has come from Magdala type deposits that lie in a corridor that extends both north-northwest and south-southeast from Stawell (see Figure 1-1). Although the geology is well understood around the Magdala mine, outcropping rocks of the Delamarian Fold Belt extend only a short distance north of Stawell before disappearing beneath recent (transported) sediments of the Murray Basin. These sediments increase in thickness to the north and exploration in this area relies almost completely on geophysics and drilling.

The geological model developed at Magdala has been used as a basis for further exploration guided by geophysics and extensive drilling and this approach has resulted in some significant successes. This paper will discuss the model developed at Magdala and the role geophysical methods have played in exploring similar mineralised systems at Wildwood and Kewell (Figure 1-1). The geophysical expression of these systems will be illustrated and some guidelines for ongoing exploration in the area will be developed.

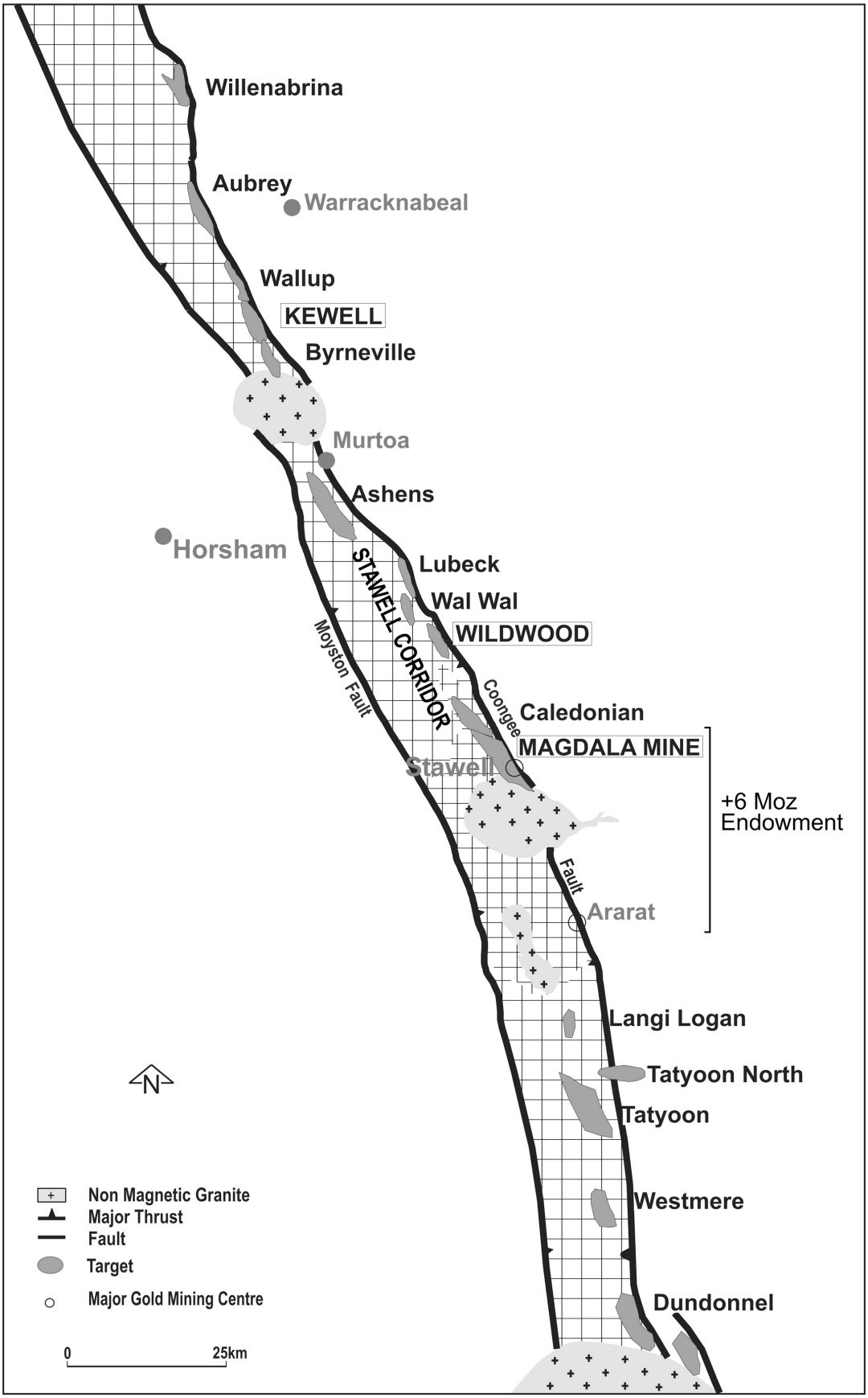

Figure 1-1: Locality plan, Stawell Corridor, Western Victoria and location of exploration targets

Regional geophysical investigations in the area included deep seismic reflection profiling as part of the 1997 crustal seismic research program conducted by Geoscience Australia and the Australian Geodynamics CRC (Korsch et al. 2002). The results have been used to develop a structural framework for the Stawell corridor (Murphy et al. this volume), but they are not relevant to direct mapping of mineral systems beneath cover and will not be discussed further in this paper.

Geological outline

Only a brief outline of the geology is included here as several other papers in this volume will review the geological evolution of the area in much more detail (e.g. Miller et al. 2005). The country rocks surrounding the Stawell Goldfield are Cambrian sediments that have experienced low-grade metamorphism (Dugdale et al. this volume). These have been intruded by (non magnetic) granites of early Devonian age (e.g. the Stawell Granite Figure 1-1). They are overlain by flat lying Tertiary Murray Basin sediments to the north and partly overlain by Tertiary basalts to the south.

Gold mineralisation at Stawell occurs mainly in a highly deformed and altered sedimentary sequence (termed the Magdala Facies) on the western flank of the Magdala basalt dome (Dugdale et al. 2005). Sulfides (pyrrhotite) and magnetite within the Magdala Facies contribute to distinctive electrical properties and the basalt itself is both magnetic and more dense than the surrounding sediments.

Exploration for similar deposits in the area has focussed mainly on the location of similar basalt 'domes' beneath cover, followed by drill testing. Several similar basalt 'domes' have been located and investigated, including Wildwood and Kewell (Figure 1-1) which will be discussed in more detail later in this paper. Detailed modelling of the basalt 'domes' has contributed to locating optimal areas for the identification of areas of alteration and associated gold mineralisation. In addition, some geophysical methods have been tested for direct detection of the equivalent of the Magdala Facies beneath cover.

Petrophysics

The earliest reported petrophysical measurements at Stawell were made on 7 oriented samples submitted to the Rock Magnetism Section of the CSIRO Division of Exploration Geoscience (Schmidt 1990; Robson 1990). The samples were basalt, Magdala Facies and possibly Albion Formation, primarily from Magdala and Wildwood. Most samples showed a high Koenigsberger Ratio, with stable magnetic remanence close to the plane of foliation. Some samples showed reversed magnetisation but all were approximately in line with the earth's present field. Although insufficient samples were tested to give totally reliable results, these suggest that the main effect of the remanent magnetisation would be to modify the amplitude rather than change the shape of observed magnetic responses at Magdala and Wildwood.

Additional petrophysical data has been collected at several stages during the current exploration program. This work has included laboratory measurements on samples, downhole logging with a range of tools and also indirect determination of some physical properties by inversion of geophysical data. Initially the principal interest was to improve definition of the magnetic properties of the main lithologies, but

subsequently the specific gravity, electrical properties and dynamic elastic properties have also been determined.

A suite of 66 core samples from various lithologies (principally at Magdala, Wildwood and Kewell) was selected and submitted to the PALM (Palaeo, Archaeo and Litho Magnetism Laboratory) at Latrobe University in August 2002, for the determination of specific gravity, magnetic susceptibility and remanence. Results were reported in Musgrave and Vega (2003a,b) and mean values for the results are summarised in Table 1-1.

Lithology	SG (# samples)	K (# samples)	Q (# samples)
Basalt	2.94 (26)	718 (26)	5.03 (26)
Magdala Facies	3.06 (28)	2317 (26)	9.29 (26)
Albion Formation	2.77 (6)	322 (6)	76 (6)
Leviathan Formation	2.76 (4)	28 (4)	0.21 (4)

Table 1-1 – Summarised petrophysical results from Musgrave (2003a, b). SG is Specific Gravity (gm.cm-3), K is Magnetic Susceptibility (SI.10-5), Q is Koenigsberger Ratio.

Clearly the main anomalous magnetic and gravity responses are likely due to the basalt and/or Magdala Facies, with a possible contribution from the Albion Formation. They show a significant contrast with the Leviathan Formation, which is considered typical of the background response from the more sandy 'country rocks'. Samples of Albion Formation exhibited highly variable magnetic properties, which may correlate with alteration (Dugdale et al. this volume), but they are not yet well understood. This extreme variability in magnetic properties was also noted in the basalt and Magdala Facies, but they were more widely sampled and the results are considered reasonably representative.

It is particularly important to note that, as previously observed by Schmidt (1990) and Robson (1990), the magnetic lithologies also have a very high Koenigsberger Ratio (Q) so that the observed magnetic signature is likely to be dominated by remanence. Musgrave and Vega (2003a) also noted 'moderate to very high' magnetic susceptibility anisotropy (AMS) in most samples with observed paleoremanences aligned close to the susceptibility foliation plane. Although the observed magnetic data at Magdala and Wildwood do look relatively 'normal', observed magnetic responses at Kewell, appear more complex and difficult to explain by normal induced magnetisation.

A subset of these samples was also submitted to Systems Exploration (NSW) Pty Ltd for the determination of electrical properties (in addition to SG and magnetic susceptibility). Samples were basalt (with or without visible pyrrhotite), mineralised Magdala Facies and one sample of mineralised Albion Formation. Results were reported in Emerson (2003) and they are summarised in Table 1-2.

Lithology	SG (# samples)	K (# samples)	Q (# samples)	σ (# samples)	M (# samples)
Basalt	2.91 (10)	1533.89 (9)	2.67 (10)	0.00 (10)	10.90 (10)
Basalt with pyrrhotite	3.28 (1)	1972.00 (1)	13.30 (1)	400.00 (1)	227.00 (1)
Magdala Facies	3.16 (20)	3228.83 (18)	8.82 (20)	2296.65 (20)	158.40 (20)
Albion Formation	2.82 (1)	132 (1)	30.4 (1)	1 (1)	4 (1)

Table 1-2 - Summarised petrophysical results from Emerson (2003a). SG is Specific Gravity (gm.cm-3), K is magnetic susceptibility (SI. 10-5), Q is Koenigsberger Ratio, σ is conductivity (Siemens metre-1), M is chargeability (milliseconds).

These results were consistent with the values of Specific Gravity, magnetic susceptibility and Koenigsberger Ratio determined by Musgrave (Table 1-1). One sample of basalt with visible pyrrhotite showed a significant increase in Specific Gravity, magnetic susceptibility and Koenigsberger Ratio; but this is not considered typical. There was also only one sample of Albion Formation which, although not statistically significant, gave values consistent with Musgrave (2003).

In addition these measurements confirmed that the presence of pyrrhotite was closely associated with a significant increase in conductivity and chargeability. When no visible pyrrhotite was present, both the conductivity and chargeability were extremely low and unlikely to be detectable in field measurements. Although it might be anticipated that black shales (possibly graphitic) could also cause high conductivities and chargeabilities, no samples were available for confirmation.

It was concluded that electrical measurements of conductivity and/or chargeability should be effective in locating pyrrhotite mineralisation (with or without gold) in either Magdala Facies or Albion Formation, provided they can effectively penetrate the overlying conductive Murray Basin sediments. There may be some other spurious sources of electrical anomalies (e.g. black shale) but they have not been confirmed to date.

A second suite of 15 samples of basalt and altered sediments similar to the Magdala Facies from Wildwood and Kewell was submitted to PALM for further analysis of remanence, and results were summarised in Musgrave (2004). Further analysis of the results from Kewell was undertaken by Grewar (2004). Unfortunately, all samples in this set were affected by a stable remanence component oriented close to the core axis, which is considered to be an artefact. It was probably imposed on the core by exposure to strongly magnetised drill pipe or core barrels, and is not considered likely to represent the rock properties in situ. The origin and orientation of remanence in the magnetic lithologies within the Stawell corridor remains an important problem and better understanding is likely to contribute significantly to more detailed magnetic interpretation.

Wire line logging to determine magnetic susceptibility, inductive conductivity, natural gamma and density has been useful at Magdala, and several newer prospects, including Wildwood and Kewell (Figure 1-1). A typical sample log with the complete suite of tools is included in Figure 1-2. The magnetic susceptibility and conductivity

logs are presented in linear and logarithmic scales to highlight both their broad dynamic range and subtle variations.

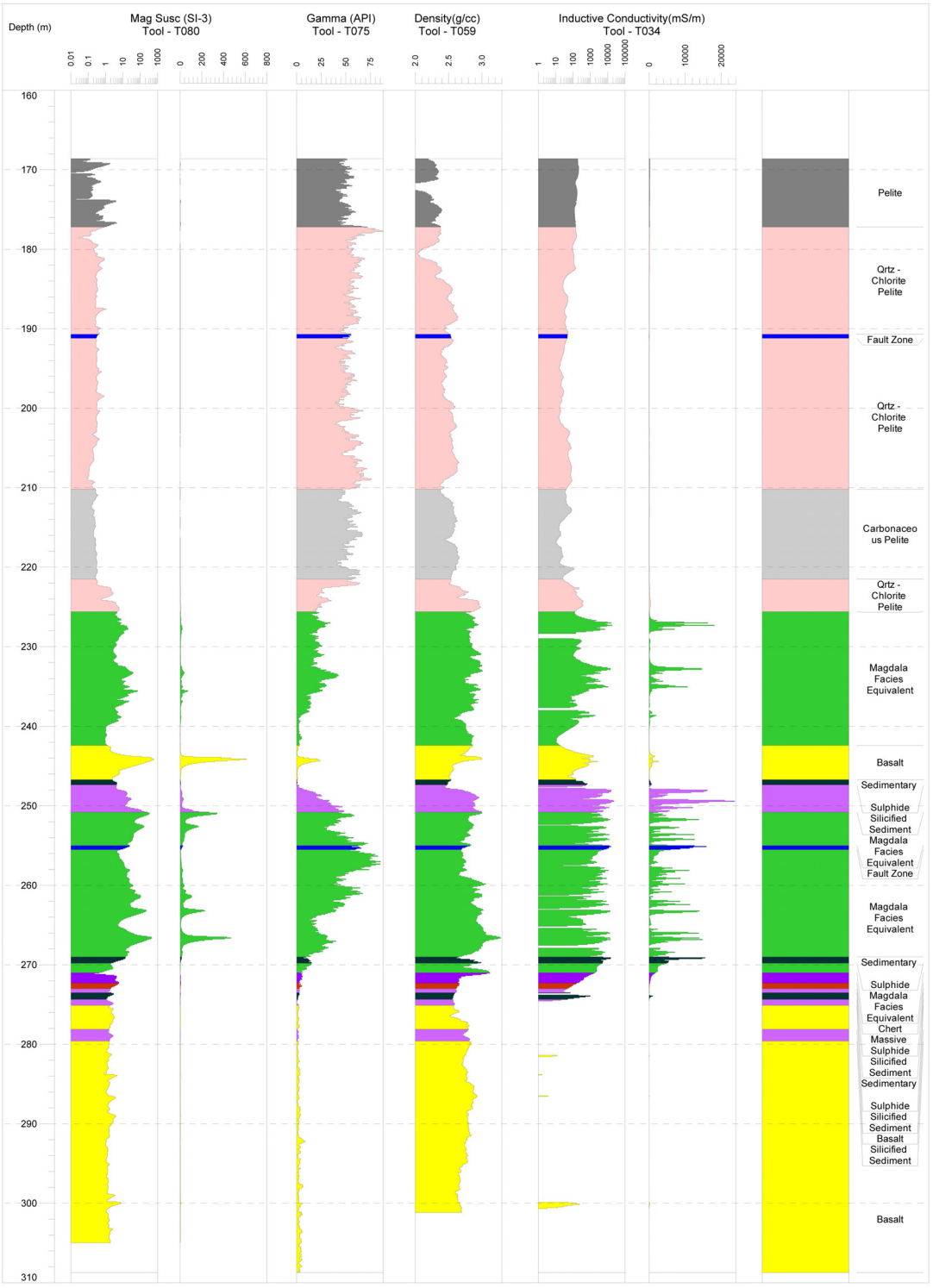

Figure 1-2: 2003 Down hole wireline geophysical log of hole KD038 from Kewell

The results show a clear increase in magnetic susceptibility and density in the basalt and Magdala Facies and these together are considered to be the main source of magnetic and gravity anomalies. The only significant conductivity anomalies are

associated with Magdala Facies or adjacent sediments (Albion Formation). Natural gamma logs are very low in the basalt, but generally increase in the alteration zone and the adjacent sediments. Detailed examination of the logs has shown some evidence of high gamma activity associated with alteration and mineralisation in and adjacent to faults, but this is not yet well understood.

Regional Geophysics

Regional geophysical data sets (from GeoScience Victoria and Geoscience Australia) include aeromagnetic and radiometric coverage. The most recent used 60 to 80 m terrain clearance and a line spacing of between 200 m and 250 m. Although radiometric data were collected with the magnetic data, the Murray Basin cover masks the emissions from the rocks of the Delamerian Fold Belt and it is therefore of little use when exploring for blind ore bodies hosted within them. This regional coverage has been supplemented in the specific areas of interest by detailed aeromagnetic surveys flown at 35 m terrain clearance on 50 m spaced lines. An image of the resulting data is shown in Figure 1-3(a). The trace of the Moyston Fault is clearly evident to the north of the Stawell granite as is the dominant response from the Stavely volcanics to its west. At right angles to the northwest-southeast grain of the Delamerian Fold Belt strings of Lower Devonian Diorite intrusions produce discrete, high intensity, ovoid magnetic anomalies. The narrow ridges running north-south across the grain of the image are strand lines in the Murray Basin cover. The increasing thickness of Murray Basin sediments north of the Stawell granite causes the character of the image to become smoother to the north, while the high frequency 'chatter' to the south of Stawell, around Ararat, is due to Tertiary basalts.

GeoScience Victoria has in filled the Geoscience Australia country wide 12 km gravity mesh with a 1.5 km network of stations over much of Victoria. This produces a magnificent base from which to target areas for exploration and is provided at no cost. This 1.5 km coverage has been further in filled over the prospect areas with a 50 m by 200 m detailed grid. An image showing a residual gravity data set created from these combined data is presented in Figure 1-3(b). Again the Moyston Fault is evident but now can be easily traced to the south of the Stawell granite. The Coongee Fault is more clearly represented on the gravity image than its magnetic counterpart as is the relatively low density Stawell granite. The northeast-southwest trending cross faults that have controlled the emplacement of the Lower Devonian Diorites are also evident on the gravity image highlighting their deep seated nature.

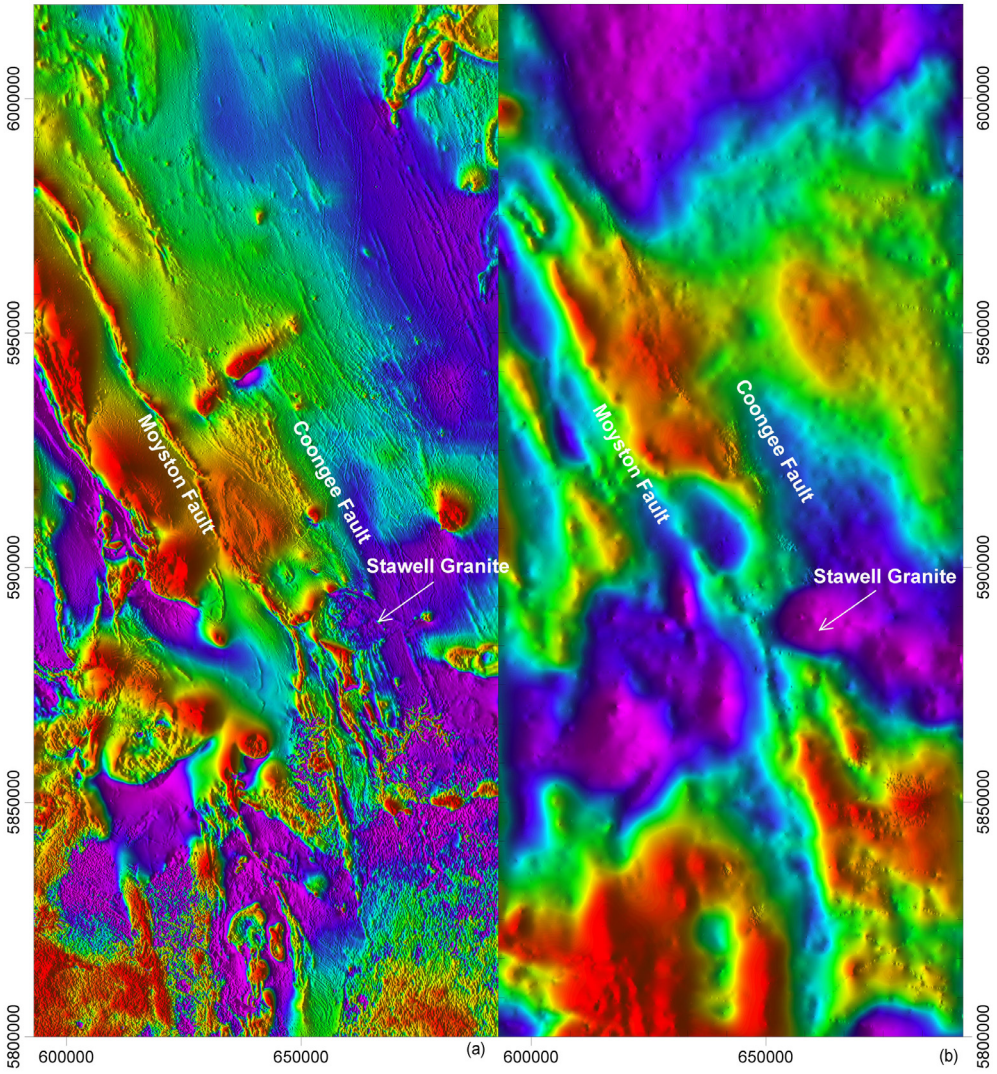

Figure 1-3: (a) Image of Total Magnetic Intensity illuminated from the west.(b) Image of Residual Bouguer Gravity after removal of a 40 km regional computed at a density of 2.67 T/m3. Regional aeromagnetic and gravity data from GeoScience Victoria and Geoscience Australia and detailed surveys provided by Metex and Levithan resources.

Prospect Scale Geophysics

Having used the regional gravity and aeromagnetics to select the prospects, geophysical techniques can then be used to help define drill targets within them. At a prospect scale, three main areas will be discussed. Magdala is the "type" area where the exploration model was initially developed and where physical properties were measured on samples and in drillholes. Secondly, Wildwood was located beneath relatively shallow cover, a few kilometres north of Stawell. Finally, Kewell will be discussed. This prospect is located 85 km north northwest of Stawell beneath about 120 metres of transported and highly conductive Murray Basin sediments.

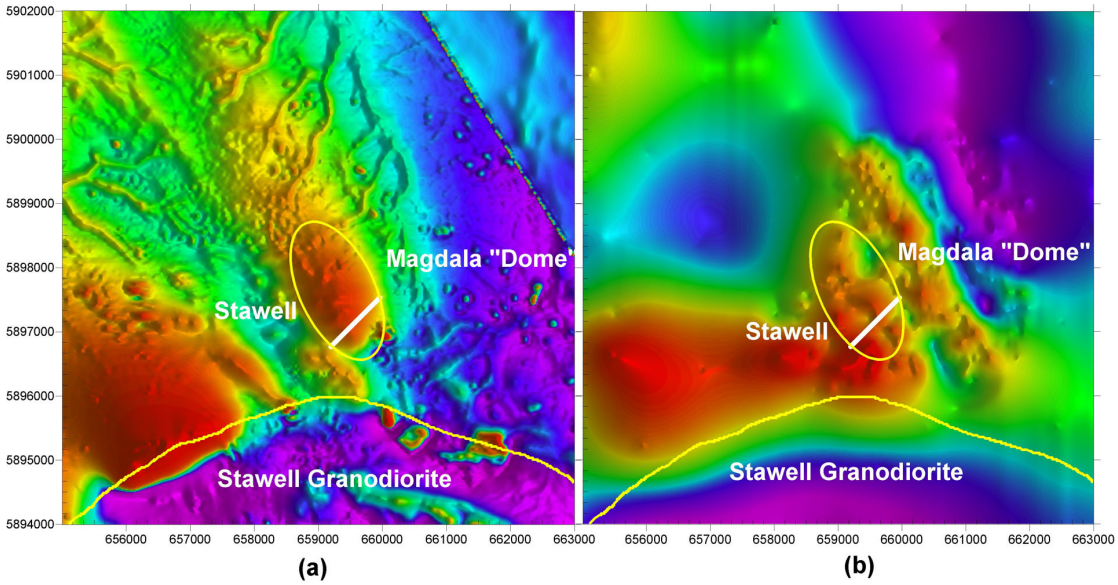

Figure 1-4: Images of TMI (a) and Residual Gravity (b) over Magdala. Illuminated from the east. The position of Line 254 is shown in white and Line 320 in green.

Figure 1-4a illustrates side lit total magnetic intensity (TMI) and residual gravity images over the Magdala 'Dome'. The arcuate zone denoted near the southern margin of the figure outlines the northern extent of the Stawell Granite. The town of Stawell is marked and the ovoid magnetic high near the centre of the figure outlines the approximate location of the Magdala 'Dome'. The dendritic patterns to the northeast and west of the Magdala Dome are the magnetic response from Tertiary palaeochannels containing maghemite and sometimes alluvial gold. A subtle blurring of the magnetic image over the township of Stawell is due to the increased terrain clearance required by the civil aviation authorities. The large semi-circular anomaly to the south west of Stawell is caused by a magnetic diorite intrusive which postdates the relatively non magnetic, low density Stawell granite. A number of small high frequency magnetic anomalies on the edge of the Stawell granite, to the south of Magdala, are due to cultural interference (town rubbish tip etc.) The gravity image suffers from the irregular sampling, however the gravity ridge over the denser basalts at Magdala is still apparent as is the parallel ridge to the east over the Brown's prospect (Figure 1-4b).

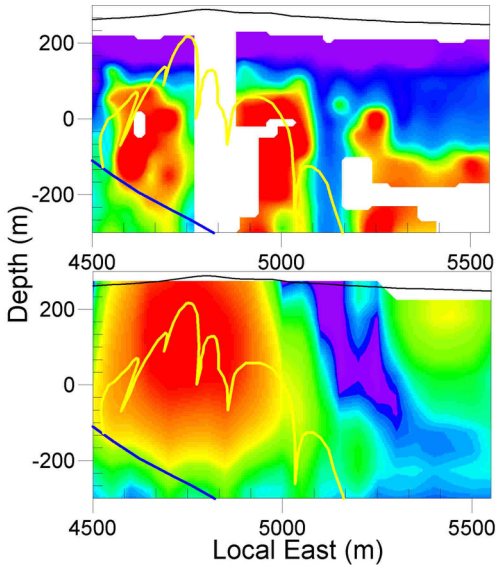

Figure 1-5: TEM CDI (top) and slice from 3D magnetic inversion (bottom) over Magdala, Line 254. Warm colours are conductive (top) or magnetic (bottom). Overlay of interpreted geology, basalt (yellow), South fault (blue) and ground surface (black)

The mineralised Magdala Facies at Magdala are cut by pyrrhotite veins up to 20cm thick. Pyrrhotite is an excellent conductor and this is reflected in the measured conductivity values for the Magdala Facies shown in Table 1-2 and the wireline log of Figure 1-2. The petrophysical results relate to hand specimens selected from drill core that would not necessarily include samples of the massive pyrrhotite from the veins. Any electromagnetic response will be biased by the pyrrhotite veins and thus the measured response should be expected to be greater than that predicted from the petrophysical data alone. A trial line of in-loop Transient ElectroMagnetics (TEM) was acquired over the deposit on Line 254, (Figure 1-4). A conductivity depth image (CDI) generated from the TEM data is presented in Figure 1-5a along with a section through a 3-D inversion model of the aeromagnetic data. Unfortunately the density of gravity coverage over this section is inadequate for inversion at this scale and no gravity inversion model is included. Overlain on both images are outlines of the basalt (yellow) and the South Fault (blue) interpreted from drilling and mining. A high tension power line running to the mine corrupted the TEM data for 100 m at the crest of Big Hill, hence the data gap in the TEM CDI, near 4900. The CDI presented here is based on a 1-D direct approximation developed by Nekut (1987) and as such is not designed to provide an accurate representation of the conductivity in a 2-D or 3-D environment. Never-the-less it does indicate conductive zones coincident with the thicker parts of the thin layer of conductive Magdala Facies overlying the basalt. The significance of the conductive zone on the eastern side of the CDI is open to interpretation and is yet to be determined by drilling. A clear break is evident in both sections around 5100, this is interpreted as Albion Formation. Both the magnetic inversion and the CDI appear to have imaged the South Fault remarkably well. This is probably entirely coincidental as these methods are not usually expected to image the base of thick conductors and magnetic units with any precision. This trial line of TEM provided the encouragement to undertake additional surveys on the prospects to the north.

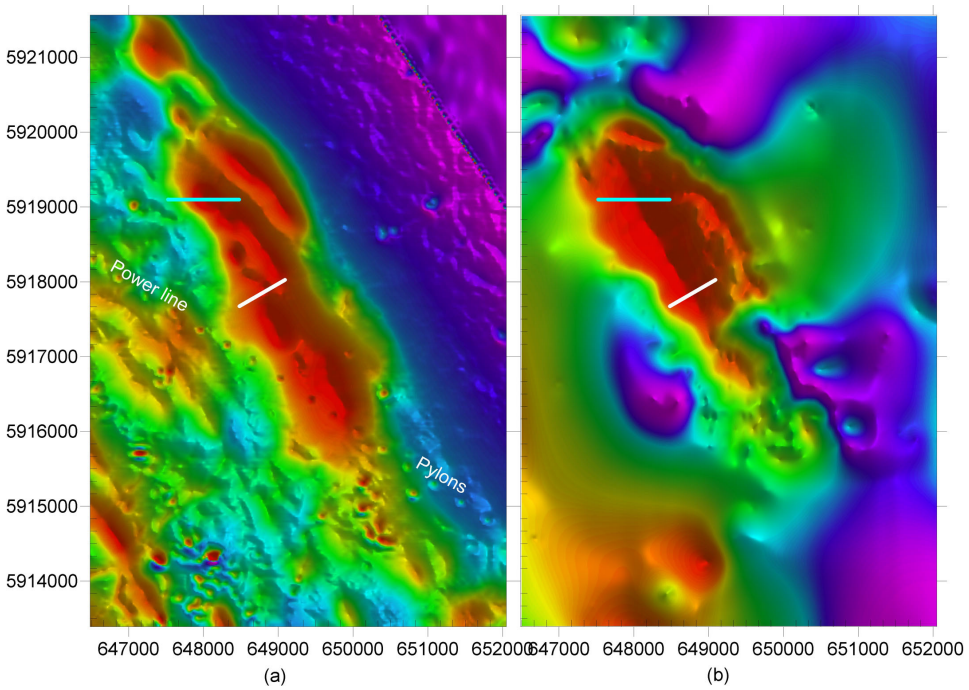

Figure 1-6: Images of Wildwood TMI (a) and residual Gravity anomaly (b) both illuminated from the SW. Position of EM line (while) and IP/AMT line (blue)

Side lit images of TMI and residual gravity over Wildwood (Figure 1-6) illustrate the detailed nature of the aeromagnetics with the trail of small circular anomalies due to high tension power line pylons crossing the image. Again the variability in the station interval is evident in the gravity image. It is immediately clear that the gravity and magnetic anomalies are different both in overall shape and fine detail. This is interpreted to be due to the presence of magnetic sediments (Albion Formation equivalent) which are not as dense as the basalt/alteration package. These sediments extend the magnetic anomaly to the south of the gravity anomaly and account for much of the difference in detail between the two.

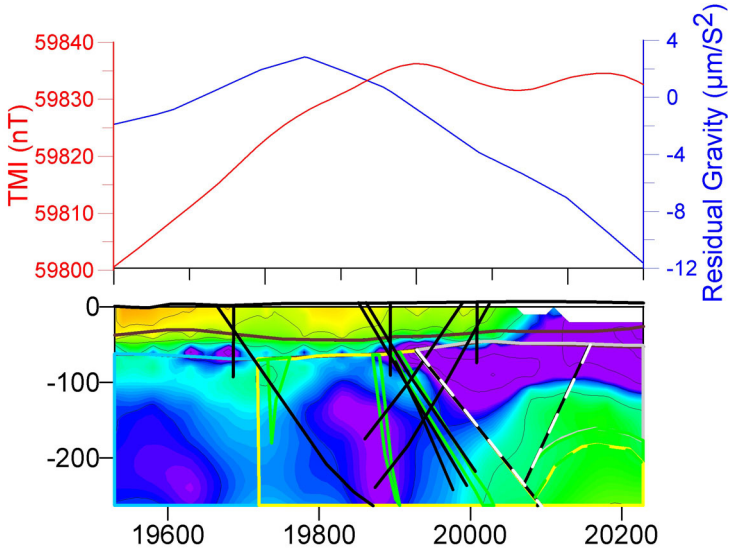

Figure 1-7: Wildwood Line 75200 TEM CDI, geological interpretation and drilling alligned with profiles of TMI and residual gravity. Basalt (yellow), Volcanogenics (green), Sulphides (white) and base of transported cover (brown)

Following the apparent success of the trial EM line over Magdala a second trial line was acquired over a weakly mineralised section at Wildwood. Figure 1-7 shows a CDI created from in-loop TEM data with the current geological interpretation overlain. Also shown in Figure 1-7 are profiles of the aeromagnetic response (red) and residual gravity (blue). Inspection of Figure 1-6 indicates that the TEM line was close to an interpreted, approximately east-west trending fault which appears to truncate the basalt and offset the magnetic sediment. This is clearly not the 1-D environment assumed by the CDI algorithm, never-the-less it shows conductive zones which correspond with the shallow sulfide intersections at 19730 and 19920. It also does an excellent job of mapping the base of the conductive overburden until it becomes too thin to resolve at 20100. The conductive, magnetic and slightly more dense unit at the eastern end of the section has not been intersected by drilling but it is interpreted to be sediment, probably Albion Formation equivalent, as it does not appear to be dense enough for basalt or Magdala Facies.

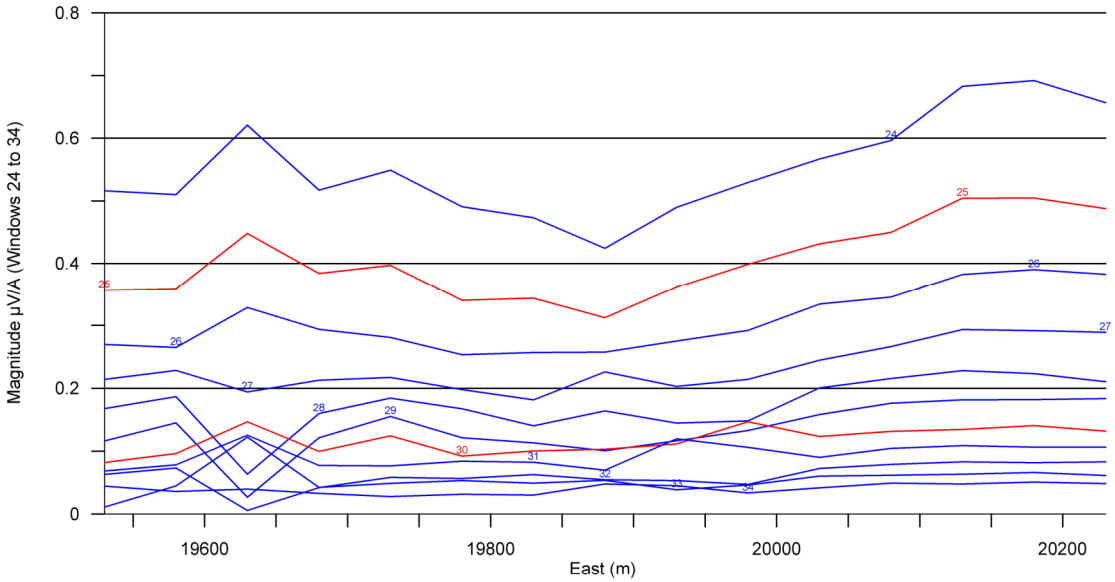

Figure 1-8: Stacked profiles of window amplitude, Line 75200, windows 24 to 34, 14.67 mSec to 126.08 mSec

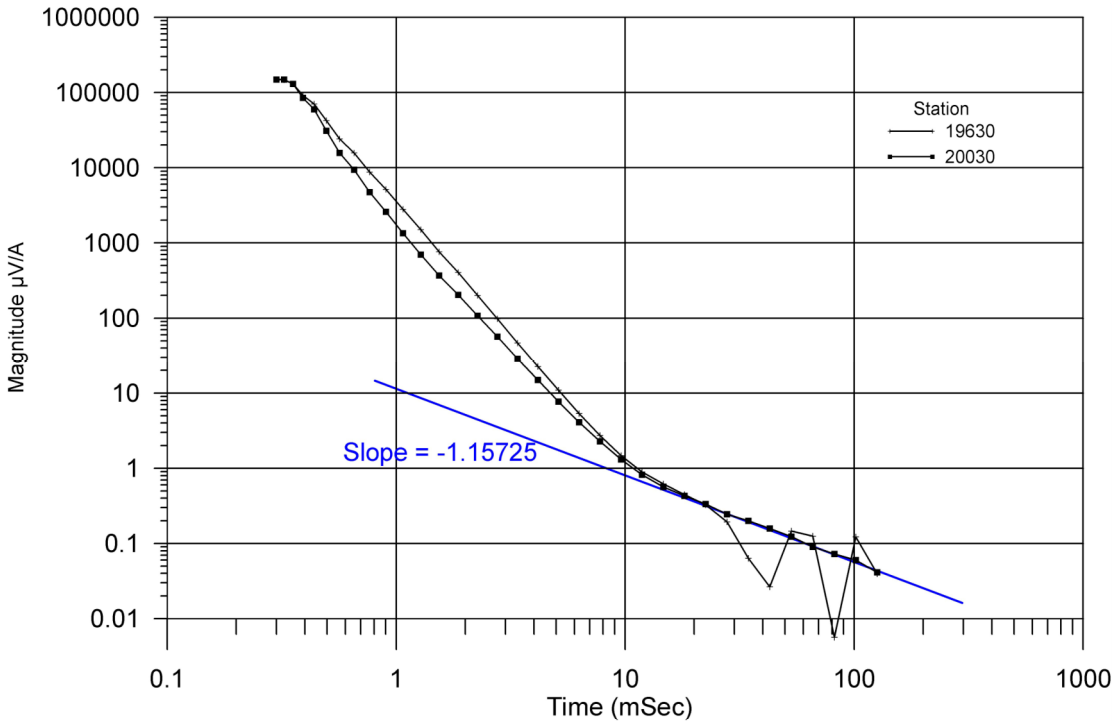

Figure 1-9: Decay plots for stations 19630 and 20030 from Wildwood line 75200. Overlain with best fit late time power law decay.

An alternative interpretation ascribes the apparent conductor at depth beneath 20000E and 20200E to a superparamagnetic (SPM) effect from near surface maghemite (Buselli, 1982). TEM profiles for the later time channels (channels 24 to 34) are shown in Figure 1-8. Clearly, the data west of about 20000E is noisy and channels after 26 were not included in the CDI transform. East of 20000E, the profiles are much more regular and increase in amplitude in the later channels. This is what has caused the apparent conductor at depth. Figure 1-9 shows a decay curve for station 19630E, an obviously noisy point on the profile, overlain on the decay for station 20030E, where the late time decay is more regular. Also shown in the figure is a late time, power law fit to the decay for station 20030E, which indicates a decay constant of 1.157. This is close to the theoretical value of 1 caused by superparamagnetism (SPM), an effect usually ascribed to surficial maghemite. Subsequent field inspection at Wildwood confirmed the presence of significant maghemite in the soil, and an observable increase in maghemite towards the eastern end of the line was noted. It is rare to observe such SPM effects in central loop TEM data, since they are usually most pronounced close to the transmitter loop. Nevertheless, such a slow rate of decay (t^{-1}) cannot be explained by normal inductive processes and SPM effects are the most likely explanation.

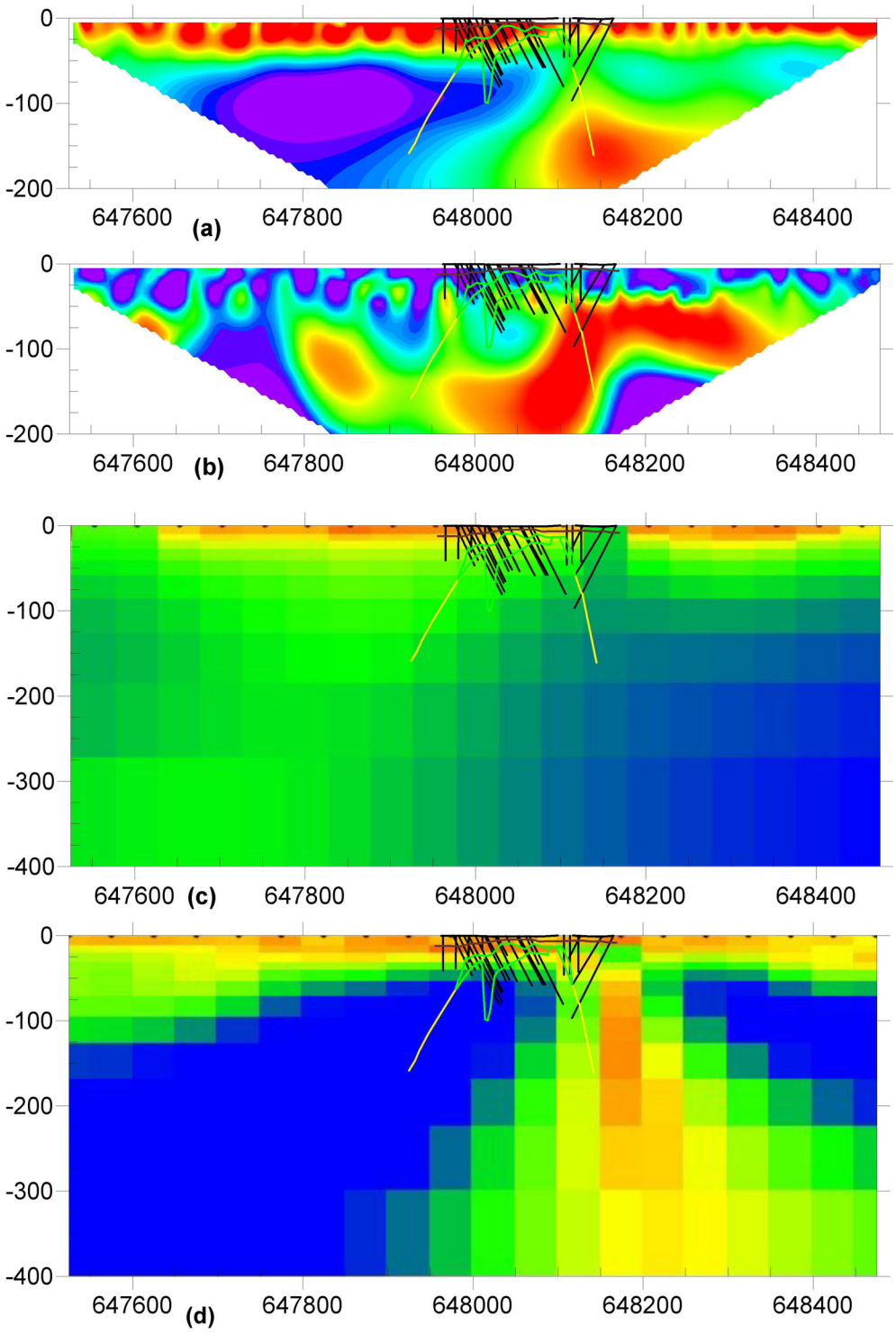

Figure 1-10: Wildwood line 5919100N, stacked sections from 2D inversion of (a) dipole-dipole resistivity, (b) dipole-dipole chargeability, (c) AMT TE mode, (d) AMT TM mode with geological interpretation overlain Basalt (yellow), volcanogenics (green), base of transported cover (brown). Note Dipole-dipole resistivity has warm colours for low resistivity.

Although sulfide mineralisation at Wildwood was not extensive, the depth of cover was also limited and a trial line of IP & resistivity and AMT (Figure 1-6) was surveyed in 2004. The survey was conducted with dipole-dipole array and 50 m dipoles, using the MIMDAS system operated by GRS Pty Ltd (Ritchie, 2004). Results

are summarised in Figure 1-10. The top two panels show 2-D inversion models for resistivity and chargeability respectively. The depth of conductive cover is clearly shown in the resistivity model. Neither of the IP and resistivity models showed a significant response to the sulfide mineralisation known from drilling. It is assumed that this is due to the relatively small volume of sulfides present. A deep conductive zone is indicated near the eastern contact of the basalt and sediments and a pronounced chargeable zone coincides with it and extends further to the east. The TE mode AMT model maps the conductive cover quite well but does not detect any conductors at depth. The TM mode AMT also maps the conductive cover but also indicates a deeper conductor near 648200E, coincident with the conductive and chargeable zone detected by the IP survey. This area has not been extensively drill tested and the source is not known although it has been suggested that it may be due to weakly disseminated sulfides or graphite in Albion Formation equivalent.

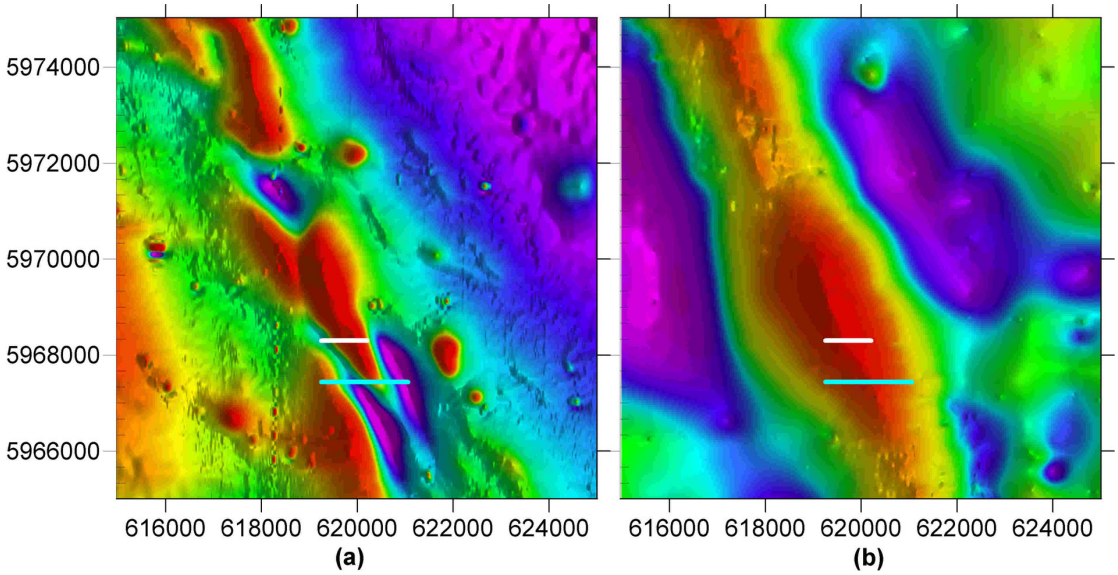

Figure 1-11: Kewell, images of TMI (a) and Residual Gravity (b) illuminated from the east. Location of TEM line shown in white and IP/AMT line in blue.

Figure 1-11 shows side lit images of the TMI and Residual Gravity over the Kewell Prospect. The main magnetic trend in Figure 1-11(a) is a complex combination of positive and negative magnetic anomalies, whereas the gravity image (Figure 1-11(b)) shows a single, relatively uncomplicated ridge. The complex magnetic responses are likely to be caused by remanently magnetised sediments and/or an alteration envelope equivalent to the Magdala Facies. These sediments are also foliated and exhibit magnetic anisotropy with maximum susceptibility close to the plane of foliation. At the southern end of the Kewell 'dome', south from about 5967440N, the sediments and alteration envelope have been shown to extend continuously across the top of the basalt and its flanks. Further north, the top has been removed and only the flanks remain. The complex magnetic responses at Kewell are not yet fully understood and work is continuing. Bordering the central magnetic corridor are a number of discrete semi-circular anomalies due to Devonian Diorite intrusions, as well as lines of high frequency features coincident with power lines.

In-loop TEM data were collected over targets along the gravity ridge. Figure 1-12 shows a CDI of one of these lines as well as sections through the 3-D inversion

models of magnetics and gravity over the same line. The TEM has again done a good job of mapping the base of the conductive overburden and even appears to be responding to the unsaturated Loxton sands higher in the section, indicated as a near surface resistor. The source of the weak bedrock conductive zone within the basalt, near 619800E, has not been confirmed by drilling but corresponds with an apparent decrease in density, shown in the gravity inversion. It may be due to fracturing in the basalt or deeper weathering increasing the porosity and thus increasing the relative concentration of saline ground water in this area. Only minor sulfide mineralisation was known on this line and the TEM does not appear to have responded to the mineralisation.

The 3-D magnetic and gravity inversion models were constrained to include no magnetic or density variations within the Murray Basin sequence hence the upper levels of the model are blank. Despite remanence dominating the response along strike, at this locality the magnetic inversion outlines the basalt very well.

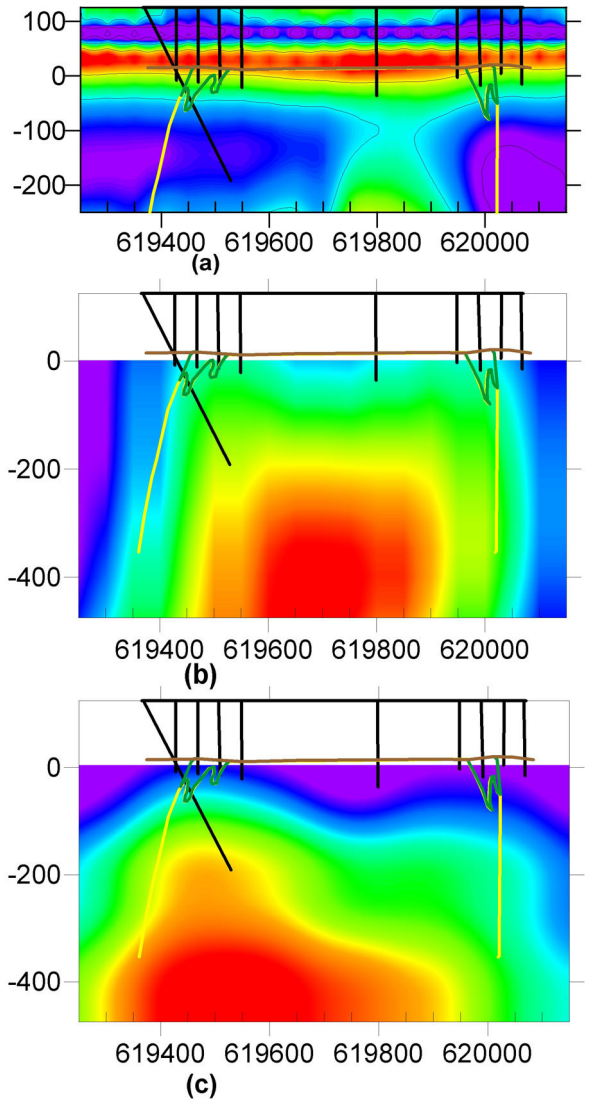

Figure 1-12: Kewell Line 5968300N sections of TEM CDI (a), 3D magnetic inversion (b) and 3D gravity inversion (c) overlain by the geological interpretation from drilling. Basalt shown in yellow, volcanogenics (green) and base of transported cover (brown)

A trial of IP, resistivity and AMT was conducted on Line 5967440N at Kewell (Figure 1-13). The method used was similar to measurements at Wildwood, but 100 m dipoles were used in an attempt to penetrate beneath the thicker (approximately 120 m) surficial layer of conductive sediments. The IP and resistivity inversion models both show near surface horizontal layering due to the Murray Basin sediments, but the thickness is exaggerated. The resistivity model shows a similar two layer (resistive overlying conductive) to that shown in the CDI (Figure 1-12(a)) but with an apparent deeper conductive zone near 620200E. This coincides with an extensive layer of sulphide alteration equivalent to the Magdala Facies extending across the top of the basalt dome. The chargeability model also shows a coincident chargeable zone, but it is not clearly defined. In this case, chargeability measurements were affected (at high n spacings) by both telluric noise and EM coupling due to the conductive overburden. Although corrections were made, some residual effects remain and would have limited the resolution. The IP survey only penetrated effectively over a short central section of the survey line, extending over about 500 m, where measurements were made to a dipole spacing of >10.

Both TE and TM mode AMT models show a conductive near surface layer, with the base close to that known from drilling. They also both indicate a deeper conductive zone near 620200E, coincident with the known sulfide mineralisation, but it is only poorly defined in the TE model. No other deep conductors were detected over approximately 2000 metres of line surveyed.

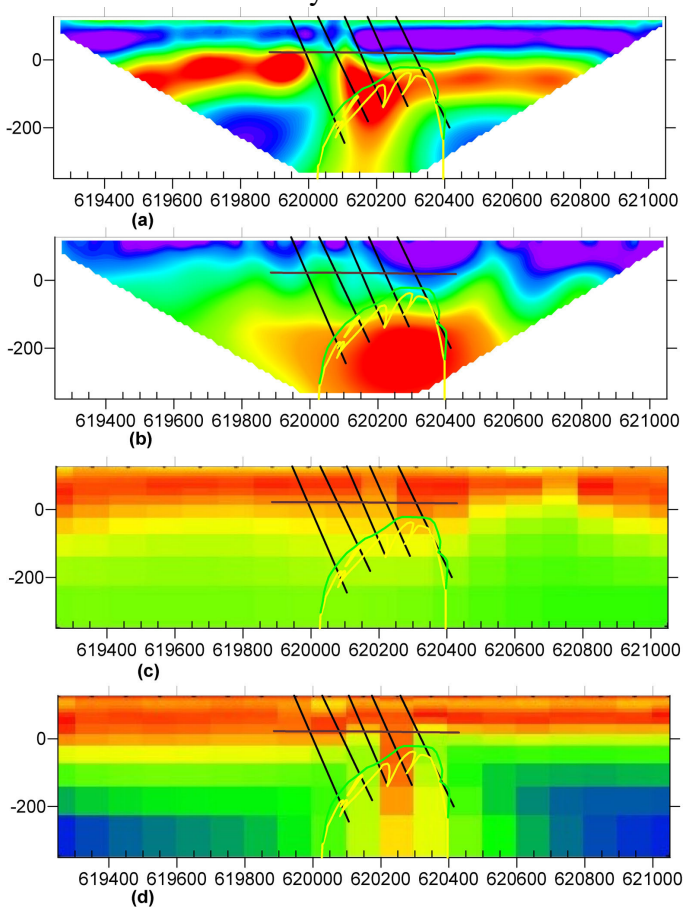

Figure 1-13: Kewell line 5967440N 2D inversions of (a) resistivity (hot colours for low resistivity), (b) chargability, (c) AMT TE mode, (d) AMT TM mode with geological interpretation and drilling overlain. Basalt (yellow), Volcanogenics (green) and base of Murray Basin (brown)

Conclusions

Regional aeromagnetic and gravity data are essential tools in target selection beneath the Murray Basin cover. The data is readily available and it has been shown to lead directly to the detection of basalt 'domes' and associated alteration beneath >100 metres of transported cover, at distances of up to 100 Km from any outcrop.

At a prospect scale, detailed aeromagnetics and gravity play an important role in lithological mapping. A good understanding of the physical properties of the target and host lithologies is critical for drill targeting at this stage. Electrical methods (EM, IP and AMT) can be applied effectively although their usefulness decreases as the cover thickens. Although tests at Kewell were not conclusive, they were encouraging. In particular, AMT measurements appeared to be the most effective in penetrating thick conductive cover and detecting the known mineralisation.

Petrophysical measurements on samples and down-hole wireline logging provide a valuable adjunct to visual geological mapping of core and chips as well as providing base values for modelling of the surface geophysical data.

More work is required to fully understand the complex magnetic properties of the ore environment and how they may relate to the ore forming processes. Direct detection of alteration haloes beneath thick conductive cover by electrical methods appears possible, but it remains a challenging task which will receive more attention in the future.

References

Buselli G. 1982. The effect of near surface superparamagnetic material on electromagnetic measurements. *Geophysics*, Society of Exploration Geophysicists 47, 1315-1324, 1982.

Dugdale A.L. & Wilson C.J.L. 2005. Evolution of a complex hydrothermal alteration system associated with a sediment-hosted orogenic gold deposit: Stawell, western Victoria. *Australian Journal of Earth Sciences* (submitted).

Emerson D.W. 2003. Report on petrophysical results; Systems Exploration (NSW) Pty Ltd; Project #08/2003, (unpublished).

Grewar J. 2004. The stratigraphic, structural, alteration and rock magnetic variations across a basalt-high, Kewell, western Victoria. B. Sc. (Hons) thesis, The University of Melbourne, Melbourne (unpublished).

Korsch R.J., Barton T.J., Gray D.R., Owen A.J. & Foster D.A. 2002. Geological interpretation of a deep seismic-reflection transect across the boundary between the

Delamerian and Lachlan Orogens, in the vicinity of the Grampians, western Victoria. *Australian Journal of the Earth Sciences*, V 49/6, December 2002, 1057-1075.

Miller J.McL., Wilson C.J.L. and Dugdale L.J., 2005. Ordovician to Early Devonian structural evolution of the western Victorian gold deposits. *Australian Journal of Earth Sciences* (submitted)

Murphy, F. C., Rawling, T., Wilson, C. J. L., Dugdale L. J., and Miller, J. McL. 2005. 3-D Structural Framework of Western Victoria and implications for targeting gold mineralisation. *Australian Journal of Earth Sciences* (this volume)

Musgrave R.J., 2004. Report on remanence analysis of second set of Kewell/Wildwood samples. Report to pmd*CRC, dated March 4, 2004 (unpublished).

Musgrave R.J. & Vega M., 2003a. Magnetic petrophysics report; Stawell Project. Report to pmd*CRC, dated August 31, 2003 (unpublished).

Musgrave R.J. & Vega M., 2003b. Stawell Magnetic Petrophysics Study Remanence Report. Report to pmd*CRC, dated December 1, 2003 (unpublished).

Musgrave R.J., Grewar J. & Vega, M., 2005. Rock-magnetic assessment of the significance of remanence in Stawell gold field magnetic anomalies, *Australian Journal of Earth Sciences* (this volume)

Nekut A. G., 1987. Direct inversion of time-domain electromagnetic data (short note). *Geophysics*, Society of Exploration Geophysicists, **52**, 1431-1435.

Ritchie T.J. 2004. Recent developments in electrical exploration. Proceedings of PACRIM 2004 (The AusIMM, Melbourne).

Robson D.F. 1990. Measurement of magnetic remanence from selected rock samples in the Stawell area. Memorandum to Western Mining Corporation Ltd, dated September 11, 1990 (unpublished).

Schmidt P.W. 1990. Magnetic properties of mineralised samples from Stawell. CSIRO Report PS2-1, August 1990 (unpublished).

Chapter 2 : Significance of remanence in Stawell goldfield aeromagnetic anomalies

R.J. Musgrave, J. Grewar and M. Vega

Summary

Gold in the Stawell goldfield is hosted by a sequence of sulfide-mineralised metasediments (the Stawell Facies and Albion Formation) overlying chloritised basalts. Aeromagnetic anomalies in the northwestern part of the Stawell corridor display intense negative and positive lobes: at the Kewell prospect, these take the form of an axial high flanked by paired negatives. Such a pattern requires that remanence dominates magnetisation, and that the magnetisation must vary in direction across strike. Remanence demagnetisation analysis confirms the dominance of remanence over induction in the pyrrhotite-dominated Stawell Facies and Albion Formation, and indicate the presence of both normal and reversed remanence, with directions strongly controlled by the dominant S_2 foliation. A minor proportion of the Stawell Facies, Albion Formation and basalts that display coarse-grained, secondary magnetite are dominated by magnetic induction. Oriented samples from the Kewell prospect were overprinted during core recovery, precluding direct measurement of the directions of remanence. Hysteresis analysis, a well established rock-magnetic technique which previously has had very little application to aeromagnetic interpretation, provides a model to understanding remanence at Kewell. Samples from throughout the Stawell corridor group in two populations, which define two parallel domain-state mixing curves on a plot of hysteresis parameters. Population A comprises samples from the pyrrhotite-bearing basalts, and population B from the Stawell Facies. We speculate that the distinction between the two populations reflects differences in the pyrrhotite arising from contrast between high fluid flow in the high permeability volcanogenics and lower fluid flow in the basalts. Fluid-flow modelling at Kewell has emphasised the influence of high fluid flow on the flanks of the basalt structure on the location of gold mineralisation; these high fluid flow regions underlie the negative lobes of the aeromagnetic anomaly, and are characterised by samples that fall in hysteresis population B. From this we infer that the fluid flow regime has a direct control on remanence polarity at Kewell, either by resetting remanence at the time of mineralisation, or by changing the response of the high fluid flow regions to later remagnetisation processes.

Introduction

Exploration over the northwestern part of the Stawell corridor, where Murray Basin sediments cover the mineralised rocks of the Lachlan and Delamerian Orogens to a depth of more than 100 m, is structured around potential field geophysical data. Smith et al. (this volume) review these data, and point to the crucial role of contrasts in style between gravity and magnetic anomalies in interpreting structure and mineralisation. Aeromagnetic anomalies in the north-western sector of the belt, extending across the

Byrneville target, the Kewell and Wallum prospects, and north beyond the Cannum target, display linear positive anomalies (Figure 2-1) that are flanked by very intense negative lobes on one side (5984000 to 5992000 mN) or both (5965000 to 5968000 mN – the southern end of the Kewell prospect). Simple magnetic modelling, in which the contribution of remanence is neglected, cannot simulate these aeromagnetic features. It is possible to match the observed data with models including palaeoremanence (i.e., a remanence with a direction significantly different from the present field direction); in the case of the double negative anomaly at Kewell, this is only possible if either the direction or the proportion of remanence varies across strike. We set out to understand the distribution of remanence across the Stawell corridor, and to determine what constraints this could place on the structure and mineralisation of the Kewell prospect.

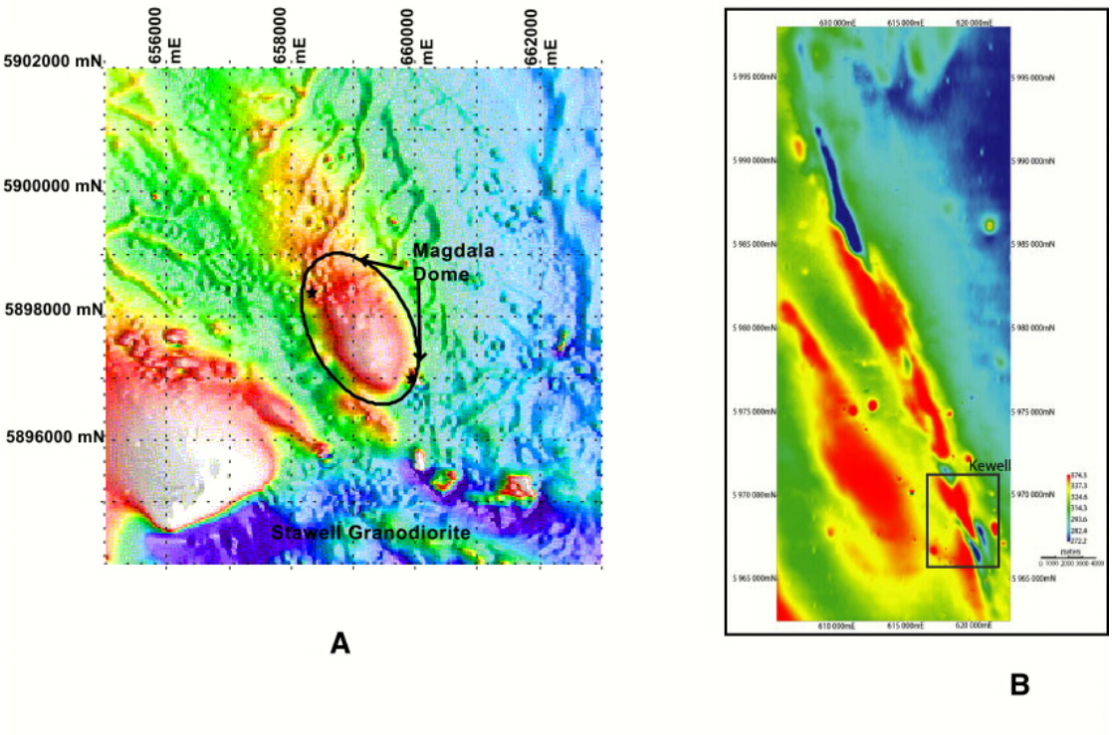

Figure 2-1. Aeromagnetic total field anomalies in the Stawell corridor. (A) Stawell region (colour drape with eastern illumination), showing position of the Magdala dome; (B) north-western part of the corridor, from the Byrneville target to north of the Cannum target; location of the Kewell prospect is boxed.

To do so, we undertook a suite of magnetic petrophysics measurements on two sets of drill-core samples. Our aim was not only to measure the more familiar rock-magnetic parameters of susceptibility (k) and the intensity and direction of undemagnetised remanence (somewhat misleadingly referred to as natural remanent magnetisation, NRM), but also to assess the relative in-situ contributions of induction and remanence. For this purpose, the conventional index, the Königsberger ratio (Q) of NRM intensity to induced magnetisation, is insufficient. Remanence, as measured on core samples (often after long storage), may comprise the sum of multiple components: these may include viscous remanence (VRM) acquired continuously and normally oriented towards the present field, coring and storage overprints, and one or more palaeoremanences acquired at various stages of the rock's history, with

directions significantly different from the present field. Of particular significance is the ratio of the intensities of VRM and the palaeoremanence; where VRM dominates, the resulting remanence is for practical purposes indistinguishable from the induced magnetisation, and anomaly inversion is relatively straightforward.

Determination of the magnitude and direction of the components of remanence can be achieved through the familiar palaeomagnetic technique of stepwise demagnetisation analysis. However, in addition to being relatively slow, the method suffers from the need to conduct measurements on small subsamples, typically cubes or cylinders with a volume of about 10 cm^3. Many mineralised rocks are highly heterogeneous on this scale, and are difficult to characterise from small samples of this type. In addition, remanence analysis requires oriented samples, often unavailable from core repositories.

Hysteresis analysis, conducted on splits of crushed samples, provides an alternative approach to assessing the contribution of remanence that can average out local inhomogeneity and does not require oriented samples. Hysteresis does not directly measure remanence, but rather determines the bulk magnetic domain state of the sample. Domain state controls the stability of remanence, that is, the extent to which palaeoremanence will have been replaced by VRM. Hence, hysteresis analysis provides a rapid means of characterising, for large numbers of samples, the extent to which we might expect remanence-dominated anomalies.

We began our analysis with a suite of samples from the core library maintained by Leviathan Resources at the Magdala mine; these included material from three lodes within the Magdala deposit (Magdala, East Magdala, and Golden Gift), supplemented by material from the Wildwood, Kewell, Caledonian, Ashens, and Wonga prospects. These samples were from unoriented core, although in many cases the plunge of the hole had been recorded, allowing partial orientation of the core relative to the core axis. Fully oriented core was provided by a new drilling campaign at the Wildwood and Kewell prospects.

Stawell Corridor Geology

The Stawell Zone, bounded to the west by the Moyston Fault and to the east by the Avoca Fault, forms the westernmost division of the Lachlan Orogen (VandenBerg et al., 2000). Tight to isoclinally folded Cambrian turbidites of the St Arnaud Group characterise the Stawell Zone and overlie the tholeiitic Magdala Basalt (Squire & Wilson, 2005), and are intruded by Early Devonian granitoids. Ductile deformation in the Stawell corridor peaked during D_2 at about 504-500 Ma (Miller et al., 2003), and followed or accompanied the metamorphic maximum. Goldfields within the Stawell Zone are concentrated in a corridor west of the Coongee Fault, termed the Stawell-Ararat Fault Zone (Wilson *et al.*,1992). Exploration to the northwest of Stawell at Wildwood and Kewell has focussed on equivalent rocks below Murray Basin cover (Jupp, 2003; Kaufman, 2003).

At Stawell, the Magdala Basalt forms a north-west trending, doubly-plunging dome, bounded by a pair of southwest dipping faults, the Coongee Fault to the northeast and the Stawell Fault to the southwest (Miller & Wilson, 2002). The dome is faulted on its flanks and repeated at depth by the late generation South Fault. Approaching the

contact with the overlying metasediments, the basalts are altered to chlorite-ankerite and ankerite-muscovite grades (Dugdale & Wilson, submitted); pillowed intervals frequently exhibit pyrrhotite mineralisation. Alteration has introduced a zone of mineralisation by coarse-grained, xenomorphic magnetite near the upper boundary of the basalt, best developed at the East Magdala lode.

Overlying the basalt, the Albion Formation comprises turbidites dominated by sulfidic black mudstone, and is succeeded by the dominantly psammitic Leviathan Formation. At the base of the Albion Formation, a 5-70 m thick interval of mudstone displays chlorite-stilpnomelane alteration and abundant recrystallised sulfides, including pyrrhotite. Structural fabric in this zone, which envelopes the Magdala Volcanics, is less clearly defined than in the overlying schists of the remainder of the Albion and Leviathan formations. Contrasts between this alteration envelope and the rest of the Albion Formation led earlier workers to attribute the distinct mineralogy of this zone to a volcanogenic sediment parentage, leading to the use of the name "Magdala Volcanogenics" (Watchorn & Wilson, 1989). Less altered parts of the Albion Formation, displaying a strongly developed crenulation cleavage, were termed the Mine Schist; this informal division extended to include parts of the Leviathan Formation in the footwall of the Stawell Fault. Psammitic rocks in the hanging wall of the Stawell Fault were termed Wonga Schist. Although now superseded (Squire & Wilson, in press), this terminology persists in much of the discussion of the exploration environment in the Stawell Corridor, and we will maintain it here.

A similar sequence of basalt, Albion Formation, and Leviathan Formation is present in drill core from the Kewell locality. Similar alteration zones to those at Magdala can be recognised, including chlorite-actinolite alteration of the basalt, and a similar chlorite-stilpnomelane-sulphide zone above the basalt. Again, informal usage refers to "volcanogenics" and "Mine Schist".

In broad form, the Kewell prospect resembles Magdala Dome: a lobate, elongate, dome-like structure surrounded by the St Arnaud Group sediments. Results of initial drilling, and inferences from gravity data, suggested that the Magdala model, a doubly-plunging antiformal dome, applied equally to Kewell (Kaufman, 2003). However, cleavage vergence in drill core is consistently to the east across the structure, and the sedimentary sequence passes eastwards from pelitic to psammitic without repetition. On this basis Grewar (2004) reinterpreted the Kewell structure as a depositional feature comprising a basaltic seamount and onlapping sediments, in which the series of basalt lobes represent tongues of individual flows rather than an anticlinorium.

Previous Studies

Western Mining Corporation commissioned a rock magnetic study of drill core samples from mineralised localities in the Stawell corridor. Five samples of pyrrhotitic Albion Formation schists and "volcanogenics" were collected at Stawell and Glenorchy, and two samples of "mafics" (presumably basalt) were taken at Wildwood (Schmidt, 1990; Robson, 1990). High Königsberger ratios, averaging 5.2 in the metasediments and 10.6 in the basalts, indicate that remanence should dominate the magnetic anomaly produced by these rocks. Anisotropy of magnetic susceptibility (AMS) is also high in both lithologies (average degree of anisotropy of 1.37 for the

metasediments and 1.11 for the basalts), and the susceptibility foliation plane is roughly parallel to the NW striking, steeply inclined S_2 cleavage which defines the dominant structural grain of the Stawell corridor (Watchorn & Wilson, 1989). NRM (i.e., remanence measured without demagnetisation) had a roughly uniform, intermediate direction in five of the seven samples (mean: declination = 250.4°, inclination = -79.5°, a_{95} = 22°), but it is unclear how faithfully this direction represents the *in situ* remanence.

Clark and Tonkin (1994) investigated the susceptibility, AMS, NRM, and demagnetisation behaviour of pyrrhotite-bearing rocks from the Cobar area of New South Wales. Intense remanence and high Königsberger ratios (frequently >5) characterised the samples, and remanence was dominated by palaeoremanences acquired during past thermal events. Magnetic anisotropy was also strongly anisotropic, averaging 1.46. Magnetic anomalies at the Elura and Magnetic Ridge localities could only be modelled if the contribution of the palaeoremanence was included.

Methods

Core segments long enough to define the core axis were selected for sampling, and described in hand specimen. Core segments were then split; for the oriented Kewell and Wildwood cores, the saw cut was made along a diameter defined by the orientation mark. One half-core was then scanned on an ordinary flatbed scanner (to give a map against which subsampling could be identified), and subsampled by one or two 2.2 cm diameter minicores drilled perpendicular to the split face for remanence measurements. One split half was cut again, and the resulting quarter core crushed in a Tema mill to fine sand size; this sample was thoroughly mixed and split to produce a representative sample for susceptibility and hysteresis measurements.

Each minicore was marked with an orientation mark relative to the core axis. NRM was measured on a Molspin spinner magnetometer, and bulk susceptibility on a Bartington MS2 susceptibility meter set at 0.46 kHz. After vacuum saturation, the density of the minicore was determined by Archimedes' method, allowing remanence and susceptibility to be defined in both volume- and mass-normalised terms. Anisotropy of magnetic susceptibility (AMS), expressed as the magnitude and direction of the principal axes of the susceptibility ellipse, was assessed on a AGICO KLY-3 Kappabridge.

Hysteresis and isothermal remanence analyses were conducted on a split of the crushed sample in a Molspin Nuvo vibrating sample magnetometer (VSM). After subtraction of the paramagnetic contribution, we determined saturation magnetisation (M_s), saturation remanence (M_{rs}), coercivity (H_c), and coercivity of remanence (H_{cr}). Bulk domain states were determined by plotting hysteresis results on a Day plot (Day et al., 1977). Magnetic stability was also assessed by the index D_{JH}, the ratio of the two axes of the Day plot (Housen & Musgrave, 1996).

The Königsberger ratio (Q) was calculated from the susceptibility and the NRM intensity, assuming an ambient field of 50,000 nT. Where this exceeded 0.5, we proceeded with remanence analysis by stepwise demagnetisation. Thermal

demagnetisation at 50° intervals from 100°C to 500°C was conducted with a Magnetic Measurements MMTD shielded furnace on one minicore from each core sample. A selection of samples were demagnetised by the alternating field (AF) method in a Molspin AF demagnetiser, at 5 mT intervals to 50 mT.

Vector data: remanence and AMS

Fully oriented samples

Samples oriented by the spear method from MPI Mines diamond drill holes KD3, KD5, and KD6 at Kewell, and WWD3 and WWD5 at Wildwood, were demagnetised thermally. Without exception, demagnetised remanence in these samples was either chaotic, or dominated by a component aligned on, or within 20° of, the uphole direction of the core axis (Figure 2-2). Orientation of individual core pieces with

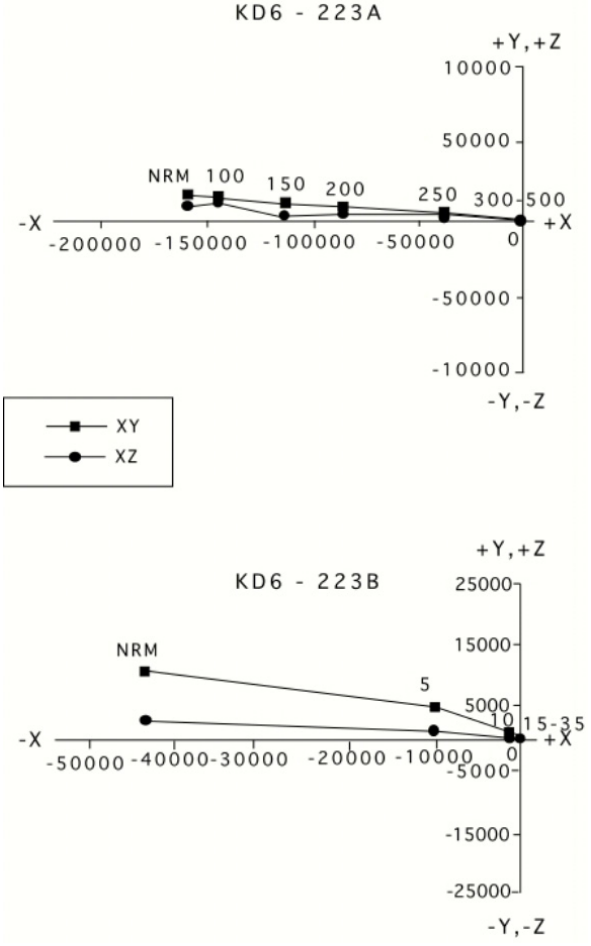

Figure 2-2. Zijderveld plots showing overprinted remanence in two specimens of a fully oriented sample: upper plot shows thermal demagnetisation (temperatures in °C); lower plot AF demagnetisation (peak field in mT). Orientation is with respect to core fiducial mark: x-axis is the downhole core axis, y-axis is towards the fiducial mark, z axis is perpendicular to the core splitting plane, which was cut through the fiducial line. Axes show remanence intensity in mA/m.

different duplicate samples from core pieces from KD5 and KD6 produced similar results, distinguished only in that demagnetisation was achieved in fewer steps than by the thermal method.

The remanence is clearly an artefact, rather than an in-situ component. None of the likely sources of systematic measurement errors (bias in the spinner magnetometer signal, acquisition of a partial thermoremanence in the demagnetising furnace, or anhysteretic remanence in the AF demagnetiser) is consistent with the observed behaviour. Overprints of this sort have frequently been observed in drill cores, and are usually ascribed to an isothermal remanence acquired by exposure to strongly magnetised core-barrels, possibly enhanced by shock magnetisation resulting from repeated impacts of the core barrel on the drill pipe during core recovery (Shi and Tarling, 1999). Magnetisation occurs along the long axis of the cylindrical barrel, and in the local ambient field, which is inclined at about –68°, this will result in the observed alignment of the overprint upwards along the core axis.

Overprinting also makes determination of in-situ remanence intensity uncertain; the remanence intensity measured prior to demagnetisation – normally regarded as the best estimate of in-situ NRM – will exceed the in-situ remanence by an unknown amount. Königsberger ratios will also be exaggerated. Nevertheless, measured NRM (Appendix 2-1) indicates that remanence in both the basalt and volcanogenics at Kewell and Wildwood varies widely in intensity. Many volcanogenic samples from Kewell have intensities > 10,000 mA/m; even allowing for overprinting, this suggests very intense remanence characterises much of the volcanogenic facies at Kewell.

Axially oriented samples

In contrast, samples from the Stawell core library demagnetise along well-defined paths that define characteristic remanences at a range of angles to the core axis (Figure 2-3). Thermal and alternating field demagnetisation on duplicate specimens produce similar demagnetisation paths. The absence of an axial overprint in these samples presumably may be ascribed to the use of other, less magnetised core barrels, or possibly to decay of the overprint over the time the cores have remained in storage.

The lack of oriented core places severe limits on our ability to interpret orientation for remanence in the samples. Axially oriented samples can be fully oriented where the demagnetisation path indicates two (or more) magnetisation components, with the assumption that the magnetically softer component is a VRM. In this procedure, the sample is rotated around the core axis to align the VRM with the present day field, which it should parallel *in situ*. However, very few samples showed such a clear two-component remanence, and only one sample, a pyrrhotite-bearing basalt from Golden Gift (sample code B360A, from hole MD2880AW1 at 362m depth) had a VRM well-enough isolated to allow orientation of the stable remanence. The resulting orientation is declination 142°, inclination +42°, which is clearly reversed polarity.

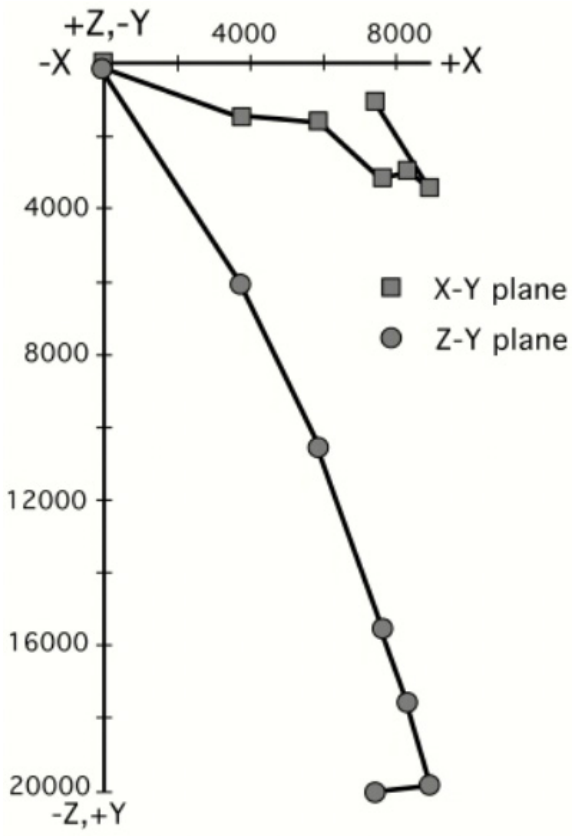

Figure 2-3. Zijderveld plots showing characteristic remanence in axially oriented sample B417 (Golden Gift volcanogenics). Z-axis is core axis, downhole positive; X and Y axes are arbitrary.

Remanence in other samples can be restricted to cones (small circles on the stereoplot) around the hole plunge with semi-apical angles given by the solid angle between the core axis and the remanence direction in core co-ordinates. Absolute orientation of vector data – both remanence and AMS axes – is not possible in these samples; however, vector directions can be defined in co-ordinates relative to an arbitrary fiducial mark on the side of the cylindrical minicore samples. AMS of most samples is moderate to very high (even amongst the so-called "unaltered" basalts). Where a mineral foliation is visible to the naked eye in individual samples, the AMS foliation is parallel to it (Figure 2-4).

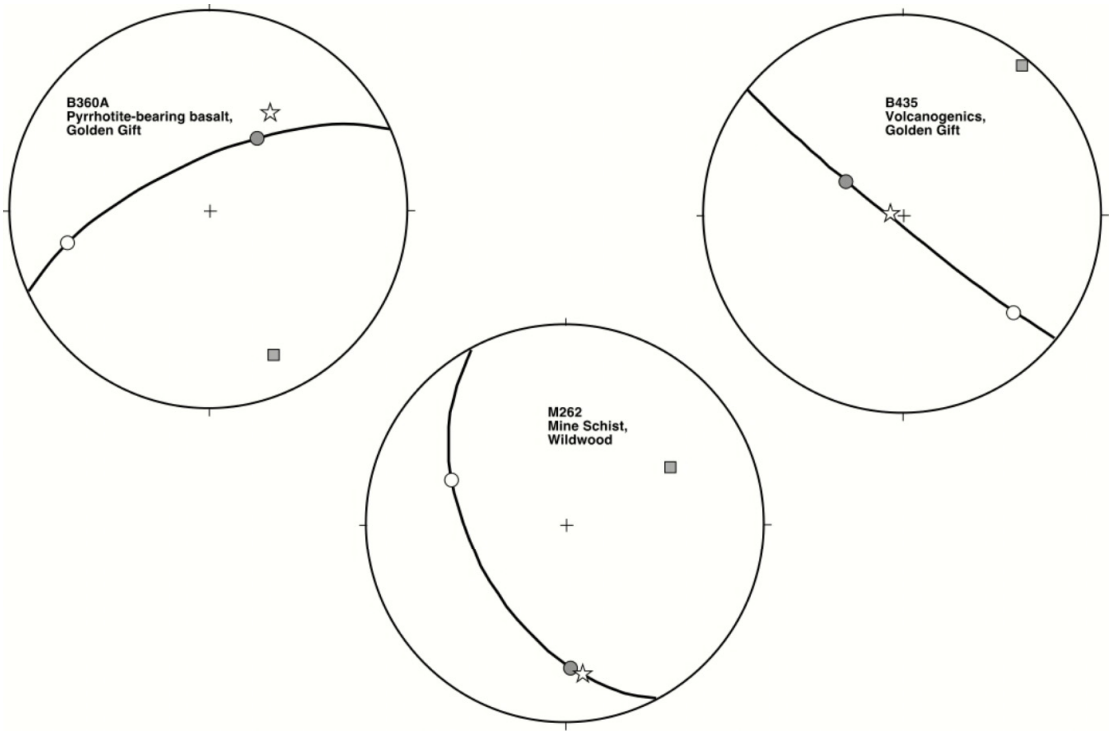

Figure 2-4. Stereographic plots showing relationship between remanence and AMS foliation and lineation in pyrrhotite-bearing samples. Susceptibility axes: filled circle = major axis (k_1); open circle = intermediate axis (k_2); filled square = minor axis (k_3). Major and intermediate axes define plane of magnetic foliation. Star = remanence direction. Directions are in arbitrary sample co-ordinates.

One set of samples, distributed across the massive basalt and magnetite-bearing volcanogenics from East Magdala and Wildwood, is defined by remanence cones that intersect, or pass within about 20° of, the present-day field, suggesting normal polarity (Figure 2-5). Königsberger ratios in these samples range from 3.7 to 19, and remanences range from 382 to 3477 mA/m with an average of 2800 mA/m. These magnetite-bearing lithologies will produce significant, remanence-dominated anomalies, but the direction of the remanence results in anomalies which are indistinguishable in form (if stronger in amplitude) from anomalies due to induction alone. Many of these samples are characterised by coarse-grained magnetite mineralisation identifiable in hand specimen; none display visible sulfides.

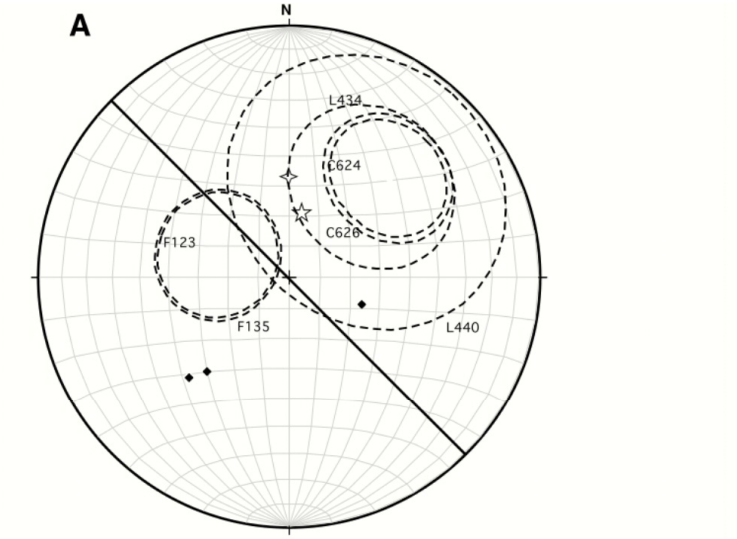

☆ Present day magnetic field (declination= 10.5°, inclination= -68.7°)

✧ Axial geocentric dipole field (declination= 0°, inclination= -56.4°)

◆ Hole plunge

Open symbols indicate upper hemisphere and closed symbols lower hemisphere

Vertical plane striking at 315° represents the regional vertical foliation

Remanence small circles for individual samples are shown solid when in the lower hemisphere, dashed when in the upper.

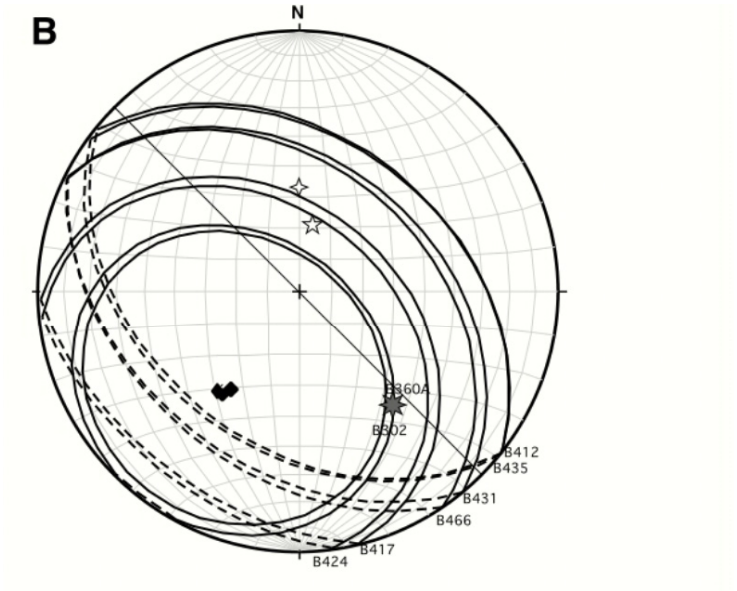

✸ Oriented remanence (declination= 142° , inclination= 42°)

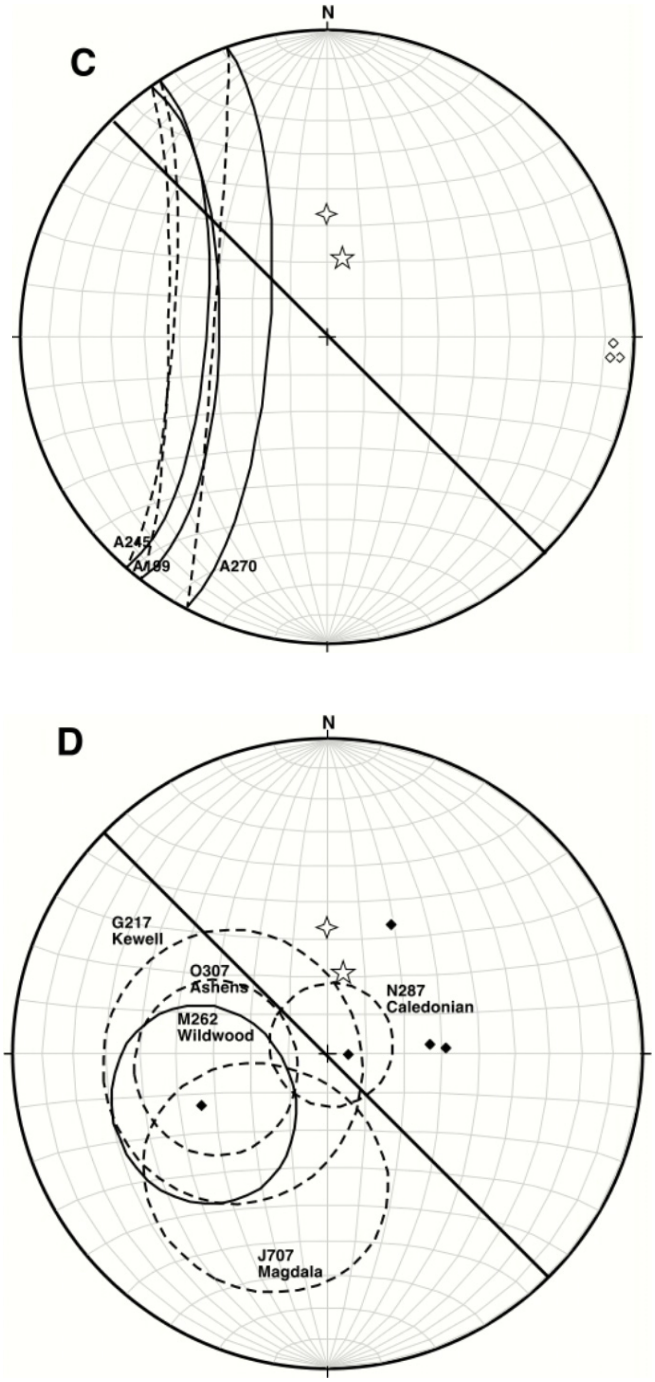

Figure 2-5. Stereographic plots of demagnetised remanence in axially oriented samples: geographic co-ordinates. (A) East Magdala and Wildwood magnetite-bearing basalts and volcanogenics, normal polarity; (B) Golden Gift, reversed polarity; (C) Magdala volcanogenics and basalts, indeterminate normal or intermediate polarity; (D) Mine Schist from Kewell (normal), Magdala and Ashens (normal to intermediate), and Wildwood (reversed).

In contrast, remanences in pyrrhotite-bearing basalts and volcanogenics from the Golden Gift lode plot on small circles distant from the present field. Remanence in most of these samples lies within 15°-20° of the AMS foliation plane, and in several cases is close to parallel to the magnetic lineation axis. Intersection of a plane representing the regionally dominant S_2 foliation, which corresponds to the AMS foliation plane, with the remanence small circles from samples from the Golden Gift

lode gives reverse polarity directions in good agreement with the oriented remanence from sample B360A. Remanence in these samples ranges up to very high intensity (NRM intensity average = 6670 mA/m, ranging from 30 to 21744 mA/m), and Königsberger ratios are also high (Q average = 4.2, ranging from 0.65 to 10.3).

Pyrrhotite-bearing volcanogenics and basalts from the Magdala lode also have small circles intersecting the foliation plane, but it cannot be determined whether their remanence is upward to the northwest (effectively a normal polarity) or downwards to the northwest (an intermediate direction, which will produce a remanence anomaly which is neither clearly normal nor reversed). Remanence in these samples averages 2900 mA/m, and Q averages 1.69 .

Mine Schist samples were collected from a variety of locations (Magdala, Wildwood, Kewell, Caledonian, and Ashens). All are characterised by $Q > 1$, and in most cases $Q \geq 30$, indicating that remanence dominates their magnetisation. Mine Schist from Magdala has a moderate NRM intensity (mean = 511 mA/m), but the sole sample from Kewell has a very large remanence exceeding 30,000 mA/m, comparable to the remanence measured in many of the volcanogenic samples from the same locality. Remanence small circles from samples from Kewell and Caledonian intersect the present field, and remanence is clearly normal, while remanence in samples from Magdala and Ashens is further from the present field, but would still be classed as normal to intermediate. Only the single Mine Schist sample from Wildwood yields a reversed remanence. In stark contrast to the Mine Schist, the Wonga Schist has very low susceptibility and NRM, and so will not give rise to a significant anomaly.

Summary

Remanence is high to very high in many of the basalt, volcanogenic, and Mine Schist samples from the Stawell corridor. In the basalts, this reflects addition of pyrrhotite or authigenic magnetite during mineralisation; unmineralised basalts are weakly magnetised, reflecting dissolution of magnetite associated with the pervasive chloritic alteration. The intensity and pervasiveness of alteration, and the clear control of the S_2 fabric on the direction of remanence, restrict the timing of acquisition of the current remanence to after the peak D_2 deformation, and presumably during or after the principal mineralisation event. At least part of the pyrrhotite-bearing basalts and volcanogenics carry a remanence that is distinctly different to the present field, and clearly reversed in the case of the Golden Gift lode. Lithologies dominated by secondary magnetite, even when strongly and stably magnetised, have normal remanences close to the present field. Mine Schist is magnetised variably from moderate to very high intensity, but at most localities the remanence is normal to intermediate, and the resulting anomaly will be difficult to distinguish from an induction anomaly.

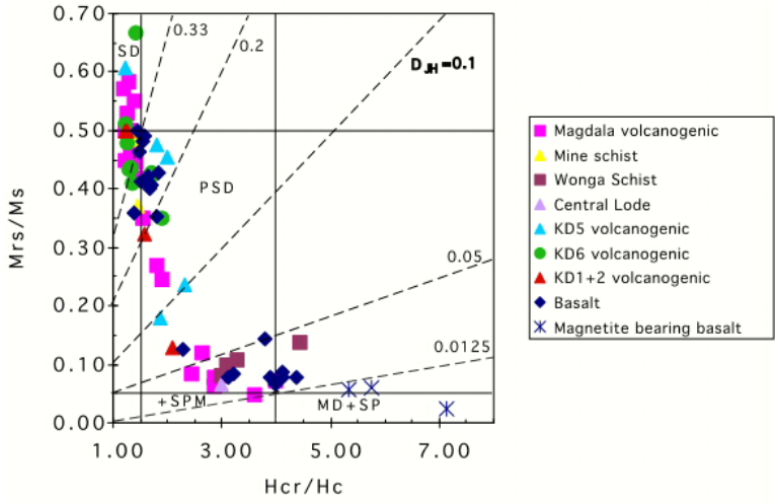

Figure 2-6. Day plot of hysteresis parameters for all samples. Fields for populations of ferrimagnetic grains are indicated: SD = single domain, PSD = pseudo-single domain, MD = multidomain, SPM = superparamagnetic. Dashed lines are contours of D_{JH}.

Magnetic petrophysics

Magnetic petrophysics ("rock magnetic") techniques, which do not require sample orientation, allowed us to supplement the limitations of the remanence analysis (Appendix 2-2). Figure 6 presents a Day plot of hysteresis results, broken up by lithology. The concentration of a high proportion of the samples in or near the single-domain (SD) field suggests that much of the sampled material should be magnetically very stable, and so should preserve a palaeoremanence which will dominate the magnetisation. Multidomain (MD) samples should be magnetically soft, much more susceptible to overprinting by VRM, and commonly with $Q \leq 1$.

Collectively, the samples define a curve very similar in form to that characteristic of mixed populations of single-domain and multi-domain magnetite (Dunlop, 1986). To our knowledge, this is the first publication of such a Day plot mixing curve for a suite of rocks in which pyrrhotite is the dominant magnetic phase, although Clark (1984) and Dekkers (1988) did list hysteresis properties for a set of size-sorted isolates of monoclinic pyrrhotite. Basalt samples group in two clusters near the SD and MD ends of the mixing curve. The more stable, SD cluster comprises the pyrrhotite-bearing pillow basalts, and some of the massive basalt. Magnetite-bearing and chloritic basalts cluster at the magnetically unstable, MD end of the curve. Volcanogenic samples are distributed along most of the length of the curve, but are concentrated near the SD end; these include the most magnetically stable material encountered in the study, with D_{JH} values exceeding 0.4.

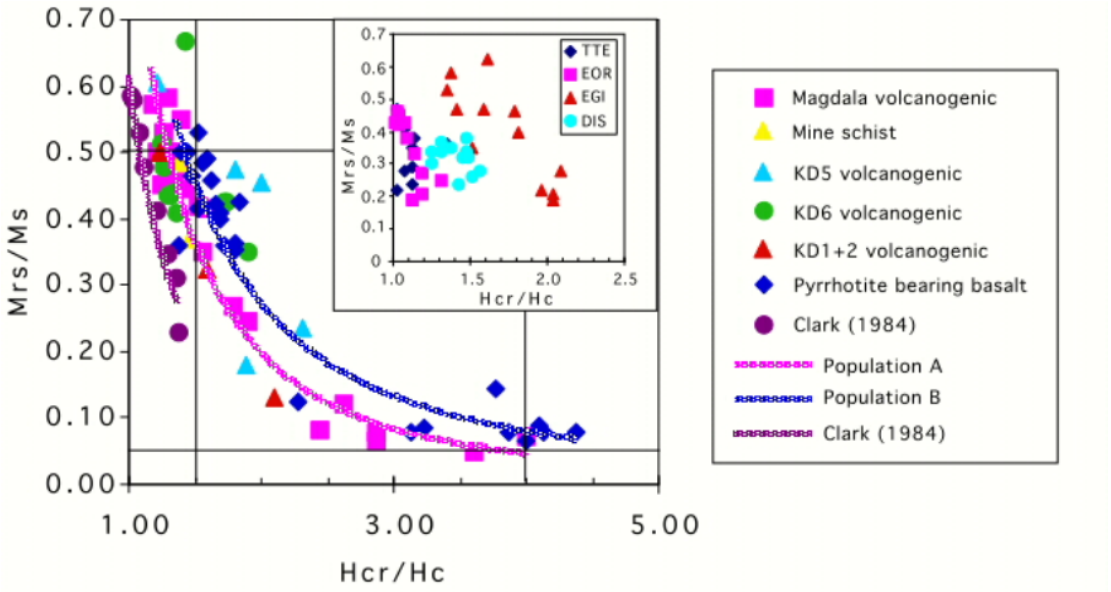

Figure 2-7. Day plot of pyrrhotite-bearing samples. Curves are best-fit power trends for populations A and B, and for Clark's size-sorted pyrrhotite isolates. Inset shows data from four suites of size-sorted isolates analysed by Dekkers (1988).

Within the pyrrhotite-bearing basalts, volcanogenics, and Mine Schist, there appear to be two distinct mixing trends (Fig. 7). Magdala volcanogenics, from the Magdala, Golden Gift, and East Magdala lodes ("population A"), define a path paralleling that of Clark's sorted pyrrhotite isolates, but displaced to higher H_{cr}/H_c ratios. Most basalt samples cluster around a second parallel trend ("population B"), displaced to still higher H_{cr}/H_c. Two basalt samples fall within population A. Mine Schist samples are spread over the two populations.

Volcanogenics from Kewell are distributed in a pattern related to the location of the drill hole. Samples from holes KD1 and KD2, drilled on the western flank of the Kewell structure, fall on the Magdala volcanogenic trend. Six samples from hole KD6, drilled into volcanogenics (Albion Formation) on the eastern flank of the structure, likewise fall in population A; the remaining four samples plot with the pyrrhotitic basalts in population B. Samples from the crest of the structure, cored in drill hole KD5, are spread widely; two fall in population A, one in population B, while the remaining two are displaced to even higher H_{cr}/H_c.

Interpretation

Both at Magdala and at Kewell, pyrrhotite-bearing volcanogenics, basalts, and Mine Schist carry intense remanences that dominate magnetisation and so set the style of the local magnetic anomaly. At Magdala, the Golden Gift lode is characterised by reversely-polarised remanence; this has little influence on the aeromagnetic anomaly, however, because its contribution is overwhelmed by the overlying normal- to intermediately-polarised basalts, volcanogenics and Mine Schist. Differences in polarity between the Magdala and Golden Gift lodes may reflect resetting of the remanence of the Golden Gift lode during a later thermal event associated with thrusting on the South Fault.

At Kewell, the intensely negative lobes of the aeromagnetic anomaly suggest that the flanks of the structure must have a reversely polarised remanence. Models of fluid expulsion during deformation at Kewell (Rawling *et al.*, 2004) mark the upper flanks of the structure (partly decapitated by erosion) as sites of high flow rates (Fig. 9). Modelled flow concentrates in the volcanogenics because of their higher permeability; the model has been successful in predicting the location of gold mineralisation in the high-flow upper flanks, evidenced by gold intersections in Hole KD3. This begs the question: is there a causal link between the patterns of remanence polarity and flow rate at Kewell?

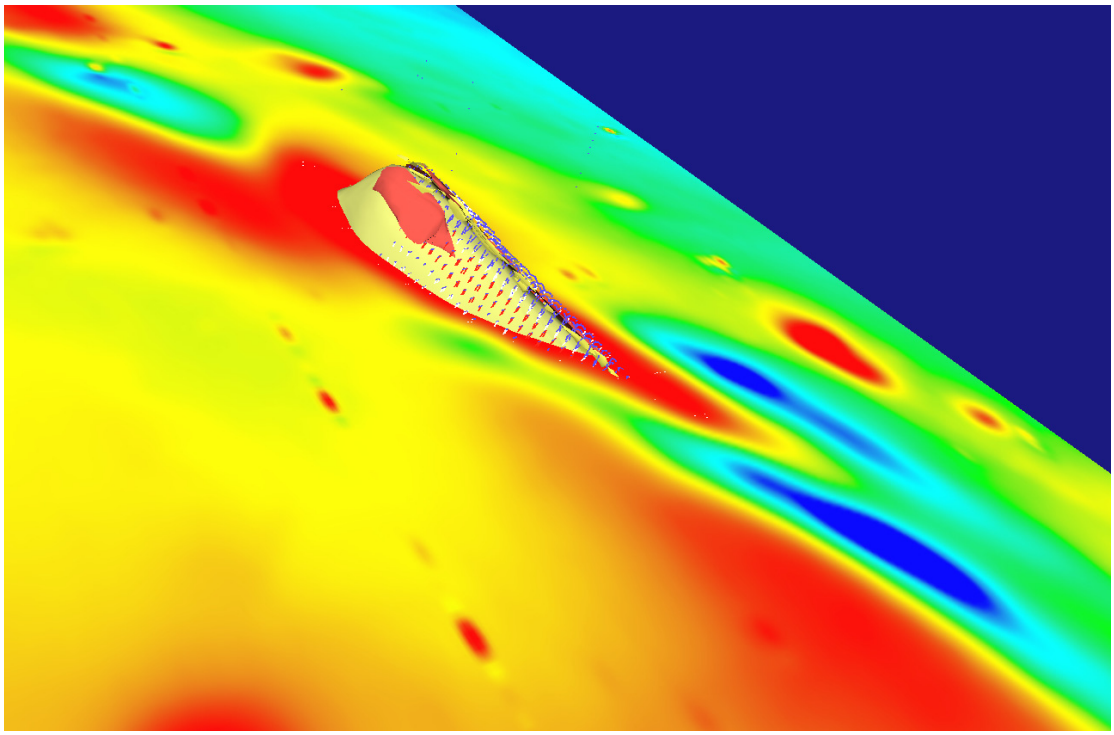

Figure 2-8. Overlay of aeromagnetic TMI map on Kewell fluid flow model of Rawling *et al.* (2004), looking from the southwest and below the surface. Areas of high (red) and low (blue) fluid flow are indicated, as are positions of diamond drill holes KD1, KD2, KD5 and KD6.

Remanence-dominated lithologies from the Stawell belt have secondary (or at least, recrystallised) pyrrhotite as the magnetic phase; alteration of both basalts and volcanogenics is so intense that little or none of the depositional magnetic mineralogy has survived. Variations in Day plot trends between population A volcanogenics and population B pyrrhotitic basalts must reflect systematic differences in the pyrrhotite characterising each. Given the influence of mineralising fluids on the formation and recrystallisation of this pyrrhotite, we hypothesise that the controlling factor is fluid-flow rate, which is partly controlled by the permeability contrast between the volcanogenics and the basalts.

Domain state will vary with changes in grain size or shape, but we would expect such changes to result in movement along a mixing curve. Offsets between mixing curves presumably require some other distinction between the two populations, and we speculate that this is a result of variations in the Fe:S ratio in the pyrrhotite, resulting in differing approximations to the Fe_7S_8 formula of the ferrimagnetic, monoclinic

form. Dekkers (1988) attributed systematic, grain-size independent variations in hysteresis properties in natural pyrrhotites to changes in the atomic percentage of Fe detected by microprobe analysis. Variations in fluid mobility are a plausible cause of differences in the Fe:S ratio.

At Kewell, samples from the high-flow upper flanks in holes KD1 and KD2 are restricted to population A, consistent with our hypothesis. Holes KD5 and KD6 sample a mix of populations A and B, which in terms of our model suggests zones of high and low flow, consistent with, if more complex than, the simple flow modelling. KD5, nearest the low-flow zone at the crest, has a higher proportion of population B samples, and samples displaced furthest to the high H_{cr}/H_c side of the population B trend.

How could the variation in hysteresis behaviour between the two populations at Kewell express itself as differences in anomaly polarity? Remanence must have been acquired at different times in the two populations; this could be the results of one of a number of mechanisms. Reversed remanence in population A could represent extensive recrystallisation in the high-fluid-flow zone during fluid migration, with pyrrhotite in the low flow parts of the volcanogenics, and throughout the less-permeable basalts, maintaining an existing polarity trough this event. Alternatively, changes in coercivity between the two populations may have made the less-stable, population A pyrrhotite more sensitive to thermal or viscous remagnetisation.

Distribution of the negative anomalies reflects the concentration of population A volcanogenics along the two upper flanks of the body, while the axial positive anomaly results from a combination of the proximity to the surface of the low-permeability, population B basalt, and the presence of a higher proportion of population B volcanogenics.

Conclusions

Rock magnetic and remanence measurements establish the control that remanence born by pyrrhotite has on aeromagnetic anomalies in the Stawell corridor. Remanence polarity, and hence anomaly style, is influenced by two features: timing of thermal events, and modifications to pyrrhotite under high- and low-flow regimes. At Kewell, negative aeromagnetic anomalies delineate high-flow regions on the flanks of the structure. We speculate that other negative anomalies along the Stawell corridor – the major flanking low northwest of the Cannum target, and smaller negative elliptical features set within the main positive trend at the northern end of the Kewell structure and at 5974000 and at 5977500 mN – may also prove to be sites of concentrated fluid flow, magnetised by the same event and at the same time as the southern flanks at Kewell.

More generally, we commend the application of combined hysteresis and remanence analysis to support aeromagnetic interpretation in mineralised zones characterised by pyrrhotite.

References

CLARK D.A.1984. Hysteresis properties of sized dispersed monoclinic pyrrhotite grains. *Geophysical Research Letters* **11**, 173-176.

CLARK D.A. & TONKIN C. 1994. Magnetic anomalies due to pyrrhotite: examples from the Cobar area, N.S.W., Australia. *Journal of Applied Geophysics* **32**, 11-32.

DAY R., FULLER M.D. & SCHMIDT V.A. 1977. Hysteresis properties of titanomagnetites: grain size and composition dependence. *Physics of the Earth and Planetary Interiors* **13**, 260–272.

DEKKERS M.J. 1988. Magnetic properties of natural pyrrhotite Part I: Behaviour of initial susceptibility and saturation-magnetization-related rock-magnetic parameters in a grain-size dependent framework. *Physics of the Earth and Planetary Interiors* **52**, 376-393.

DUGDALE A.L. & WILSON C.J.L. Hydrothermal alteration of an atypical turbidite-hosted orogenic gold deposit: the Magdala system, Stawell, western Victoria, Australia, submitted.

DUNLOP D.J. 1986. Hysteresis properties of magnetite and their dependence on particle size: A test of pseudo-single-domain remanence models. *Journal of Geophysical Research* **91**, 9569-9584.

GREWAR J. 2004. The stratigraphic, structural, alteration and rock magnetic variations across a basalt-high, Kewell, western Victoria. BSc Hons, Thesis, University of Melbourne, Melbourne (unpubl.). 95p.

HOUSEN B.A. & MUSGRAVE R.J. 1996. Rock magnetic signature of accretionary prism sediments. *Earth and Planetary Science Letters* **139**, 509-519.

JUPP B. 2003. Hydrothermal alteration and lithogeochemistry of the Kewell and Wallup prospects and their comparison with the Magdala gold, Stawell, Victoria. BSc Hons, Thesis, University of Melbourne, Melbourne (unpubl.), 193 p.

KAUFMAN A. 2003. The volcano-sedimentary and structural evolution of the Wildwood prospect, western Lachlan Orogen. BSc Hons, Thesis, University of Melbourne, Melbourne (unpubl.), 85 p.

MILLER J.McL. & WILSON C.J.L. 2002. The Magdala lode system, Stawell, southeastern Australia: structural style and relationship to gold mineralization across the western Lachlan fold belt. *Economic Geology* **97**, 325-349.

MILLER J.McL., PHILLIPS D., WILSON C. & DUGDALE J. 2003. $^{40}Ar/^{39}Ar$ dating in western Victoria: implications for the evolution of the Lachlan and Delamerian orogens. *In*: Reddy S.M., Fitzsimons J.C.W. & Collins A.S. (eds*) SGTSG Field Meeting, Kalbarri, 22-26 September 2003*. Abstracts, Geological Society of Australia, **72**, 73

RAWLING T., SCHAUBS P., DUGDALE J. & WILSON C. 2004. Development of new mineral targeting strategies using 3D modelling and numerical fluid flow simulation techniques in western Victoria. *In*: McPhie J. & McGoldrick P. (eds) *Dynamic Earth: Past, Present and Future, 17th Australian Geological Convention, Hobart, Australia, 8-13 February 2004*. Abstracts, Geological Society of Australia, **73**, 113

ROBSON D.F. 1990. Measurement of magnetic remanence from selected rock samples in the Stawell area. *Western Mining Corporation Limited, Exploration Division – Minerals (Australasia), Eastern Region, Memorandum* Reference XPR90/40

SCHMIDT P.W., 1990. Magnetic properties of mineralised samples from Stawell. *CSIRO internal report*.

SHI H. & TARLING D.H. 1999. The origin of bore-core remanences: mechanical-shock-imposed irreversible magnetizations. *Geophysical Journal International* **137**, 831-838.

SMITH R. J. & Frankcombe, K. The role of geophysical methods applied to mapping mineral systems under the Murray Basin cover (this volume).

SQUIRE R.J. & WILSON C.J.L. Interaction between collisional orogenesis and convergent-margin processes: evolution of the Cambrian proto-Pacific margin of East Gondwana. *Journal of the Geological Society of London*, in press.

VANDENBERG A.H.M., WILLMAN C.E., MAHER S., SIMONS B.A., CAYLEY R.A., MORAND V.J., TAYLOR D.H., MOORE D. & RADOJKOVIC A. 2000. The Tasman Fold Belt System in Victoria. *Geological Survey of Victoria Special Publication*, Melbourne.

WATCHORN R.B. & WILSON C.J.L. 1989. Structural setting of gold mineralization at Stawell, Victoria. *Economic Geology Monograph* **6**, 292-309.

WILSON C.J.L., WILL T.M., CAYLEY R.A. & CHEN S. 1992. Geological framework and tectonic evolution in western Victoria, Australia. *Tectonophysics* **214**, 93-127.

Appendix 2-1: Susceptibility and remanence parameters. AMS: L = lineation, F = foliation.

Location	Hole No.	Depth	Code No	Rock Type	*k* (x 10-5, SI)	NRM (mA/m)	Königsberger Ratio (Q)	*AMS* L	F
Magdala	MD3407	270	A 270	Basalt	147	92.17	1.31	1.190	1.220
Magdala	MD3407	271.6	A 271	Basalt	59	2.50	0.09	1.006	1.039
Magdala	MD3407	282.7	A 282	Basalt	65	3.93	0.13	1.035	1.035
Golden Gift	MD2880AW1	300	B 300	Basalt	169	43.87	0.54	1.282	2.087
Golden Gift	MD2880AW1	302.1	B 302	Basalt	328	252.01	1.61	1.187	1.452
Golden Gift	MD2880AW1	318.2	B 318	Basalt	62	5.26	0.18	1.016	1.017
Golden Gift	MD2880AW1	335	B 336	Basalt	61	4.16	0.14	1.019	1.016
Golden Gift	MD2880AW1	362	B 360a	Basalt	92	29.90	0.68	1.047	1.083
Golden Gift	MD2880AW1	360.6	B 360b	Basalt	188	47.31	0.53	1.057	1.208
Golden Gift	MD2880AW1	404.7	B 404	Basalt	219	43.49	0.42	1.162	1.082
Golden Gift	MD2880AW1	405.6	B 405	Basalt	164	30.82	0.39	1.045	1.197
Golden Gift	MD2880AW1	410.4	B 410	Basalt	66	4.81	0.15	1.007	1.018
Golden Gift	MD2880AW1	411.5	B 411	Basalt	58	2.34	0.08	1.028	1.023
East Magdala	SD508	624.1	C 624	Basalt	256	2322.84	19.02	1.267	1.904
East Magdala	SD508	625.9	C 626	Basalt	80	382.03	10.02	1.197	1.199
East Magdala	SD508	630.2	C 629	Basalt	1972	12501.46	13.28	1.714	1.361
East Magdala	SD509	369.7	D 369	Basalt	6144	587.98	0.20	1.011	1.743
East Magdala	SD509	373.8	D 373	Basalt	3261	593.25	0.38	1.071	1.577
East Magdala	MD922	339	E 339	Basalt	71	11.30	0.33	1.048	1.017
East Magdala	MD922	340.3	E 340	Basalt	3323	113.93	0.07	1.053	1.049
East Magdala	MD922	343.1	E 343	Basalt	237	9.93	0.09	1.043	1.022
Wildwood	WLWD113	118.3	F 118	Basalt	80	4.94	0.13	1.053	1.075
Wildwood	WLWD113	142.3	F 142	Basalt	78	1.98	0.05	1.084	1.035
Kewell	KD1	263.5	G 263	Basalt	1239	29325.34	49.56	1.281	1.667
Kewell	KD2	175.2	H 175	Basalt	58	5.47	0.20	1.011	1.016
Kewell	KD2	187.1	H 187	Basalt	199	2980.87	31.31	1.110	1.132
Kewell	KD5	247	K5 247	Basalt	105	15.96	30.74		
Kewell	KD6	284	K6 284(a)	Basalt	1293				
Kewell	KD6	284	K6 284(b)	Basalt	232				
Magdala	MD3407	179	A 179	Volcanogenics	459	226.20	1.03	1.333	1.503
Magdala	MD3407	185	A 185	Volcanogenics	273	189.95	1.45	1.138	1.243
Magdala	MD3407	192	A 192	Volcanogenics	75	13.99	0.39	1.057	1.151
Magdala	MD3407	199.1	A 199	Volcanogenics	1435	1639.77	2.39	1.234	1.173
Magdala	MD3407	201.1	A 201	Volcanogenics	6569	5864.19	1.87	1.358	1.320
Magdala	MD3407	245.1	A 245	Volcanogenics	7036	3997.72	1.19	1.055	1.554
Magdala	MD3321	136.2	I 136	Volcanogenics	1623	1160.37	1.50	1.173	1.179
Magdala	SD598CW1	1088.3	J 1088	Volcanogenics					
Golden Gift	MD2880AW1	412.4	B 412	Volcanogeni	661	3250.26	10.30	1.332	1.065

				cs					
Golden Gift	MD2880AW1	417.7	B 417	Volcanogenics	6866	21744.31	6.63	1.325	1.301
Golden Gift	MD2880AW1	424	B 424	Volcanogenics	5491	10703.36	4.08	1.052	1.414
Golden Gift	MD2880AW1	431.3	B 431	Volcanogenics	4427	10606.99	5.02	1.535	1.174
Golden Gift	MD2880AW1	435.3	B 435	Volcanogenics	254	264.24	2.18	1.064	1.073
Golden Gift	MD2880AW1	466.4	B 466	Volcanogenics	3781	6238.16	3.46	1.214	1.263
Golden Gift	MD2880AW1	472.3	B 472	Volcanogenics	207	51.89	0.53	1.076	1.201
Golden Gift	MD2880AW1	487.8	B 487	Volcanogenics	4	1.53	0.85	1.190	1.191
East Magdala	MD923	514.5	K 514	Volcanogenics	1883	250.56	0.28	1.119	1.255
East Magdala	MD923	526	K 526	Volcanogenics	5611	1535.39	0.57	1.091	1.252
East Magdala	MD923	552.2	K 552	Volcanogenics	9307	3358.77	0.76	1.046	1.466
East Magdala	SD507	434	L 434	Volcanogenics	525	3476.75	13.87	1.227	1.660
East Magdala	SD507	440	L 440	Volcanogenics	665	1185.56	3.73	1.022	1.842
Wildwood	WLWD113	121	F 121	Volcanogenics	244	3846.56	33.03	1.027	1.544
Wildwood	WLWD113	123.3	F 123	Volcanogenics	765	3159.84	8.65	1.234	1.201
Wildwood	WLWD113	135	F 135	Volcanogenics	1300	6266.89	10.10	1.088	1.180
Wildwood	WLWD113	137.5	F 137	Volcanogenics	195	644.85	6.94	1.019	1.029
Kewell	KD1	248.5	G 248	Volcanogenics	156	65.59	0.88	1.025	1.094
Kewell	KD1	265	G 265	Volcanogenics			75.00	1.150	1.857
Kewell	KD1	271	G 271	Volcanogenics			52.42	1.414	1.574
Kewell	KD2	184	H 184	Volcanogenics	432	2266.82	11.00	1.020	1.104
Kewell	KD5	201	K5 201	Volcanogenics	63	16.56	0.04		
Kewell	KD5	211	K5 211	Volcanogenics	308	1354.77	9.21		
Kewell	KD5	214	K5 214	Volcanogenics	879				
Kewell	KD5	218.5	K5 2185	Volcanogenics	71	19.63	6.90		
Kewell	KD5	218.9	K5 2189	Volcanogenics	3042	21740.17	0.31		
Kewell	KD6	177.75	K6 17775	Volcanogenics	21	2.17	0.03		
Kewell	KD6	208	K6 208	Volcanogenics	197	201.33	0.65		
Kewell	KD6	211	K6 211	Volcanogenics	5152	42966.76	0.78		
Kewell	KD6	215	K6 215	Volcanogenics	441	118858.10	33.86		
Kewell	KD6	223	K6 223	Volcanogenics	2029	45023.97	462.29		
Kewell	KD6	224	K6 224	Volcanogenics	751	4054.74	177.80		
Kewell	KD6	240	K6 240	Volcanogenics	5894	19085.20	15.00		

Kewell	KD6	259.1	K6 2591	Volcanogenics	470	15326.71	31.28		
Kewell	KD6	259.5	K6 2595	Volcanogenics	874	19943.55	0.07		
Kewell	KD6	259.8	K6 2598	Volcanogenics	1358	29031.65	44.29		
Kewell	KD6	261	K6 261	Volcanogenics	2180	28139.39	38.40		
Magdala	MD3407	75.1	A 75	Mine Schist	994	647.80	1.37	1.932	1.257
Magdala	SD598CW1	707	J 707	Mine Schist	27	373.80	29.49	1.315	1.118
Wildwood	WWD001	262.8	M 262	Mine Schist	278	5562.15	41.86	1.770	1.352
Kewell	KD1	217.5	G 217	Mine Schist	258	32672.29	265.12	1.968	2.699
Caledonian	CAD1	287	N 287	Mine Schist	242	10586.51	91.57	1.346	1.264
Ashens	ASD2	307.9	O 307	Mine Schist	132	1918.12	30.35	1.304	1.806
Magdala	SD612W2	1375.1	P 1375	Wonga Schist	35	2.15	0.13	1.047	1.168
Magdala	SD612W2	1383	P 1383	Wonga Schist	21	2.36	0.24	1.025	1.167
Magdala	SD598C	118	Q 118	Wonga Schist	29	2.86	0.21	1.024	1.109
Wonga	WD410	287	R 287	Wonga Schist	29	3.50	0.25	1.022	1.094
Magdala	SD607	833.3	S 833	Central Lode	9	7.97	1.96	1.220	1.177

Appendix 2-2. Hysteresis parameters

Location	Hole No.	Depth	Code No	Rock Type	H_c	M_{rs}	M_s	H_{cr}	M_{rs}/M_s	H_{cr}/H_c	D_{JH}
					mT	Am^2/kg	Am^2/kg	mT			
Magdala	MD3407	270	A 270	Basalt	21	0.074	0.14	32	0.53	1.52	0.35
Magdala	MD3407	271.6	A 271	Basalt	21	1.98	5.5	36	0.36	1.71	0.21
Magdala	MD3407	282.7	A 282	Basalt	20	2	5.5	36	0.36	1.80	0.20
Golden Gift	MD2880AW1	300	B 300	Basalt	16	0.034	0.074	26	0.46	1.63	0.28
Golden Gift	MD2880AW1	302.1	B 302	Basalt	33	0.11	0.22	46	0.50	1.39	0.36
Golden Gift	MD2880AW1	318.2	B 318	Basalt	8	0.0011	0.014	35	0.08	4.38	0.02
Golden Gift	MD2880AW1	335	B 336	Basalt	9	0.004	0.047	29	0.09	3.22	0.03
Golden Gift	MD2880AW1	362	B 360a	Basalt	16	1.44	4	22	0.36	1.38	0.26
Golden Gift	MD2880AW1	360.6	B 360b	Basalt	19	0.025	0.054	28	0.46	1.47	0.31
Golden Gift	MD2880AW1	404.7	B 404	Basalt	18	0.056	0.116	28	0.48	1.56	0.31
Golden Gift	MD2880AW1	405.6	B 405	Basalt	18	0.029	0.068	33	0.43	1.83	0.23
Golden Gift	MD2880AW1	410.4	B 410	Basalt	14	0.002	0.016	32	0.13	2.29	0.05
Golden Gift	MD2880AW1	411.5	B 411	Basalt	10	0.0007	0.008	41	0.09	4.10	0.02
East Magdala	SD508	624.1	C 624	Basalt	21	0.058	0.14	32	0.41	1.52	0.27
East Magdala	SD508	625.9	C 626	Basalt	19	0.02	0.05	32	0.40	1.68	0.24
East Magdala	SD508	630.2	C 629	Basalt	17	0.047	0.096	27	0.49	1.59	0.31
East Magdala	MD922	339	E 339	Basalt	8	0.002	0.026	25	0.08	3.13	0.02
East Magdala	MD922	343.1	E 343	Basalt	8	0.004	0.06	32	0.07	4.00	0.02
Wildwood	WLWD113	118.3	F 118	Basalt	8	0.0007	0.009	33	0.08	4.13	0.02
Wildwood	WLWD113	142.3	F 142	Basalt	8	0.001	0.013	31	0.08	3.88	0.02
Kewell	KD1	263.5	G 263	Basalt	23	0.11	0.27	39	0.41	1.70	0.24
Kewell	KD2	175.2	H 175	Basalt	18	0.001	0.007	68	0.14	3.78	0.04
Kewell	KD2	187.1	H 187	Basalt	18	0.05	0.1	26	0.50	1.44	0.35
Kewell	KD6(A)	284	K6 284A	Basalt	15.5	0.006	0.017	28	0.35	1.81	0.20
Kewell	KD6(B)	284	K6 284B	Basalt	15.7	0.22	0.52	26	0.42	1.66	0.26

East Magdala	SD509	369.7	D 369	Basalt	3.5	0.0025	0.11	25	0.02	7.14	0.00
East Magdala	SD509	373.8	D 373	Basalt	4.3	0.004	0.07	23	0.06	5.35	0.01
East Magdala	MD922	340.3	E 340	Basalt	4	0.013	0.22	23	0.06	5.75	0.01
Magdala	MD3407	179	A 179	Volcanogenics	20	0.042	0.12	31	0.35	1.55	0.23
Magdala	MD3407	185	A 185	Volcanogenics	19	0.029	0.065	27	0.45	1.42	0.31
Magdala	MD3407	192	A 192	Volcanogenics	19	0.018	0.067	34	0.27	1.79	0.15
Magdala	MD3407	199.1	A 199	Volcanogenics	20	0.27	0.49	28	0.55	1.40	0.39
Magdala	MD3407	201.1	A 201	Volcanogenics	24	2.33	4	31	0.58	1.29	0.45
Magdala	MD3407	245.1	A 245	Volcanogenics	27	3.2	5.6	32	0.57	1.19	0.48
Magdala	MD3321	136.2	I 136	Volcanogenics	20	0.062	0.13	28	0.48	1.40	0.34
Golden Gift	MD2880AW1	412.4	B 412	Volcanogenics	26	0.018	0.04	35	0.45	1.35	0.33
Golden Gift	MD2880AW1	417.7	B 417	Volcanogenics	30	0.015	0.03	39	0.50	1.30	0.38
Golden Gift	MD2880AW1	424	B 424	Volcanogenics	28	0.029	0.058	34	0.50	1.21	0.41
Golden Gift	MD2880AW1	431.3	B 431	Volcanogenics	18	0.013	0.028	24	0.46	1.33	0.35
Golden Gift	MD2880AW1	435.3	B 435	Volcanogenics	27	0.027	0.065	43	0.42	1.59	0.26
Golden Gift	MD2880AW1	466.4	B 466	Volcanogenics	41	0.09	0.17	52	0.53	1.27	0.42
Golden Gift	MD2880AW1	472.3	B 472	Volcanogenics	30	0.011	0.045	57	0.24	1.90	0.13
Golden Gift	MD2880AW1	487.8	B 487	Volcanogenics	8	0.004	0.051	23	0.08	2.88	0.03
East Magdala	MD923	514.5	K 514	Volcanogenics	9	0.02	0.24	22	0.08	2.44	0.03
East Magdala	MD923	526	K 526	Volcanogenics	5	0.023	0.48	18	0.05	3.60	0.01
East Magdala	MD923	552.2	K 552	Volcanogenics	25	0.027	0.06	31	0.45	1.24	0.36
East Magdala	SD507	434	L 434	Volcanogenics	25	0.29	0.58	33	0.50	1.32	0.38
East Magdala	SD507	440	L 440	Volcanogenics	8	0.025	0.39	23	0.06	2.88	0.02
Wildwood	WLWD113	121	F 121	Volcanogenics	14	0.022	0.045	18	0.49	1.29	0.38
Wildwood	WLWD113	123.3	F 123	Volcanogenics	21	0.13	0.31	32	0.42	1.52	0.28
Wildwood	WLWD113	135	F 135	Volcanogenics	8	0.06	0.5	21	0.12	2.63	0.05
Wildwood	WLWD113	137.5	F 137	Volcanogenics	9	0.0025	0.035	36	0.07	4.00	0.02
Kewell	KD1	248.5	G 248	Volcanogenics	22	0.011	0.034	35	0.32	1.59	0.20
Kewell	KD1	265	G 265	Volcanogenics	20	0.09	0.18	25	0.50	1.25	0.40
Kewell	KD1	271	G	Volcanogenics	27	0.08	0.16	33	0.50	1.22	0.41

Kewell	KD2	184	271 H 184	Volcanogenics	10	0.013	0.1	21	0.13	2.10	0.06
Kewell	KD6	208	K6 208	Volcanogenics	21	0.006	0.009	30	0.67	1.43	0.47
Kewell	KD6	211	K6 211	Volcanogenics	17.5	1.305	3	23	0.44	1.31	0.33
Kewell	KD6	215	K6 215	Volcanogenics	13.15	2.6	7.4	25	0.35	1.90	0.18
Kewell	KD6	223	K6 223	Volcanogenics	14	0.64	1.5	24	0.43	1.71	0.25
Kewell	KD6	224	K6 224	Volcanogenics	25	0.041	0.08	31	0.51	1.24	0.41
Kewell	KD6	240	K6 240	Volcanogenics	23	2.1	4.4	29	0.48	1.26	0.38
Kewell	KD6	259.1	K6 2591	Volcanogenics	18.5	0.1	0.23	24	0.43	1.30	0.34
Kewell	KD6	259.5	K6 2595	Volcanogenics	16.5	0.35	0.8	22	0.44	1.33	0.33
Kewell	KD6	259.8	K6 2598	Volcanogenics	11.5	0.28	0.66	20	0.42	1.74	0.24
Kewell	KD6	261	K6 261	Volcanogenics	15.5	0.45	1.1	21	0.41	1.35	0.30
Kewell	KD5	201	K5 201	Volcanogenics	13	0.0008	0.0034	30	0.24	2.31	0.10
Kewell	KD5	211	K5 211	Volcanogenics	39.5	0.2365	0.39	48	0.61	1.22	0.50
Kewell	KD5	214	K5 214	Volcanogenics	16.5	0.325	0.715	33	0.45	2.00	0.23
Kewell	KD5	218.5	K5 2185	Volcanogenics	8.5	0.0065	0.036	16	0.18	1.88	0.10
Kewell	KD5	218.9	K5 2189	Volcanogenics	23.25	0.095	0.2	42	0.48	1.81	0.26
Caledonian	CAD1	287	N 287	Mine Schist	22	0.1	0.27	32	0.37	1.45	0.25
Ashens	ASD2	307.9	O 307	Mine Schist	21	0.043	0.089	29	0.48	1.38	0.35
Magdala	SD612W2	1375.1	P 1375	Wonga Schist	8	0.002	0.025	24	0.08	3.00	0.03
Magdala	SD612W2	1383	P 1383	Wonga Schist	10	0.0025	0.025	31	0.10	3.10	0.03
Magdala	SD598C	118	Q 118	Wonga Schist	7	0.003	0.022	31	0.14	4.43	0.03
Wonga	WD410	287	R 287	Wonga Schist	7	0.006	0.056	23	0.11	3.29	0.03
Magdala	SD607	833.3	S 833	Central Lode	6	0.01	0.15	18	0.07	3.00	0.02

Chapter 3 : Application of 3-D models and numerical simulations as a predictive exploration tool in western Victoria.

T.J. Rawling, P.M. Schaubs, L.J. Dugdale, C.J.L. Wilson & F.C. Murphy

Summary

Three dimensional models and computer based numerical simulations have been used in the exploration industry for some time to visualize the geometry and mechanism resulting in the formation of orebodies. Presented here are the results of an exploration program developed by the Predictive Mineral Discovery Cooperative Research Center (pmd*CRC) and Stawell Gold Mines in the orogenic gold system Western Victoria that utilized existing datasets, three dimensional modelling and numerical finite element simulations to successfully target several new orebodies and predict their geometries and extents.

Introduction

Historically the Victorian goldfields have yielded over 45 million ounces of gold, there have been no major new discoveries in the last 50 years (Phillips & Hughes 2002). Given the limited exploration techniques available to the early gold explorers and the fact that vast tracts of potentially gold bearing rocks are buried by flat-lying Murray Basin sediments, common sense dictates that there should still be substantial gold deposits awaiting discovery. In particular in the Stawell gold zone of western Victoria (Figure 3-1) considerable effort and capital has been thrown at the problem over recent years in the form of geophysical surveys, geochemical analysis and target drilling without any significant new discoveries. In response to these issues Stawell Gold Mines Mines (now Leviathan Resources) and the pmd*CRC developed a research project designed to use computer based 3-dimensional modelling and numerical simulation techniques to develop a 'predictive discovery model' for orogenic gold systems.

The process of developing the 3-D models highlighted a number of criteria that were deemed important in the development and application of computer based predictive mineral discovery toolsets. Firstly, if the approach is to be useful it would have to utilize existing datasets as much as possible in order to minimize cost of acquisition of new data. It would need to integrate existing knowledge about the geometry and plumbing architecture of systems with the deformation and mineralisation history in order to define which combination of geometrical attributes are critical to mineralisation within the system. The techniques would need to be multiscalar so that they could be applied to problems at the ore shoot, camp or crustal scale. A framework would also be required in which to apply the techniques to the problem of prediction in regions of little to now outcrop with relatively poor geometrical control.

The techniques discriminate the potential fertility of prospect regions based on limited (but reliable) field data and so provides the explorationist with a cheap exploration tool that will greatly assist in area selection and targeting but more importantly has the potential to substantially reduce the time and cost to discovery.

In this paper we describe the philosophy behind the technique, the workflows that have been adopted in order to apply the model with rigor, and present the results from both the modelling and the resultant exploration program. The paper also investigates the potential for and controls on gold mineralisation adjacent to two culminations in the Cambrian basalts of the Stawell belt, known as the Magdala and Kewell domes, using numerical models in order to:

1. model, at all scales, the fluid systems involved in the development of large gold deposits in the Stawell belt of western Victoria (i.e. ore shoot scale, deposit/prospect scale, dome scale and belt scale),
2. use these models to accurately predict the location and geometry of mineralisation in the known systems, and
3. provide a targeting indicator or prospectivity rating tool in the less well known systems.

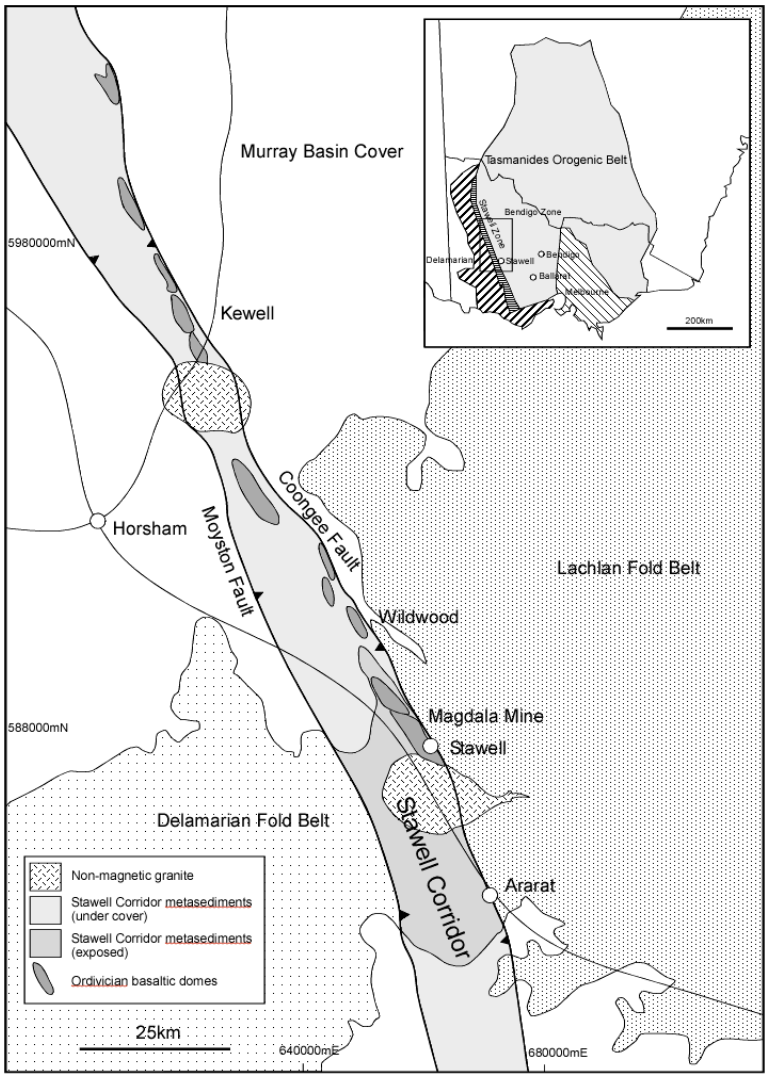

Figure 3-1. Map of the Stawell Gold Corridor showing the surface geometry of major faults and basaltic domes.

Geological Setting

Recent interpretations of the structural geology in the Stawell Zone (Miller *et al*. 2001; Miller & Wilson 2002; Wilson *et al.* 1992) have been critical to both the 3-D model building and the numerical simulations. The Magdala and Kewell basalt domes sit at a similar structural level within the Stawell gold corridor which is a ~25 km wide and >400 km long NNW-trending belt bound by the Moyston Fault to the west and the Coongee Fault to the east (Figure 1). The basalt domes all have a roughly similar geometry and relationship to surrounding units (Squire & Wilson 2005) and sit in the hangingwall of the Coongee Fault. All domes are steep sided and are interpreted to have doubly plunging domal culminations although in the case of Kewell the apex of the dome has been eroded off (Figure 3-2). The basaltic domes are composed of a mixture of massive and pillowed tholeiitic basalt that is mantled by an alteration zone previously identified as a volcanogenic sedimentary unit but now identified as the Magdala Facies (Dugdale & Wilson, submitted). A series of lobes of similar composition flank the domes and led to the geometries initially to be considered as antiformal culminations flanked by a series of asymmetric folds or mullions (Watchorn & Wilson 1989). Recent work has shown these lobes are likely to be primary volcanic depositional features as is the dome itself (Squire *et al*. submitted) although their geometries were likely to have been tightened and modified during the subsequent ductile deformations. The Dukes Nose region of the Magdala dome is a basaltic lobe of this type. Altered sediments that sit in between the basaltic lobes are known as Waterloo's and these regions are commonly strongly deformed and mineralised.

The Magdala Dome sits within a metasedimentary sequence of interbeded shales and sands known as the Albion and Leviathan Formations (Squire & Wilson, submitted). The Kewell Dome is interpreted to sit at a similar stratigraphic level within these sequences. The domes are interpreted to have undergone comparable deformation histories. Three early ductile deformation events pre-dated the gold mineralisation and produced a variably developed layer parallel schistosity, upright folds with a strong axial planar fabric and a differentiated crenulation cleavage and refolding (Miller & Wilson 2002).

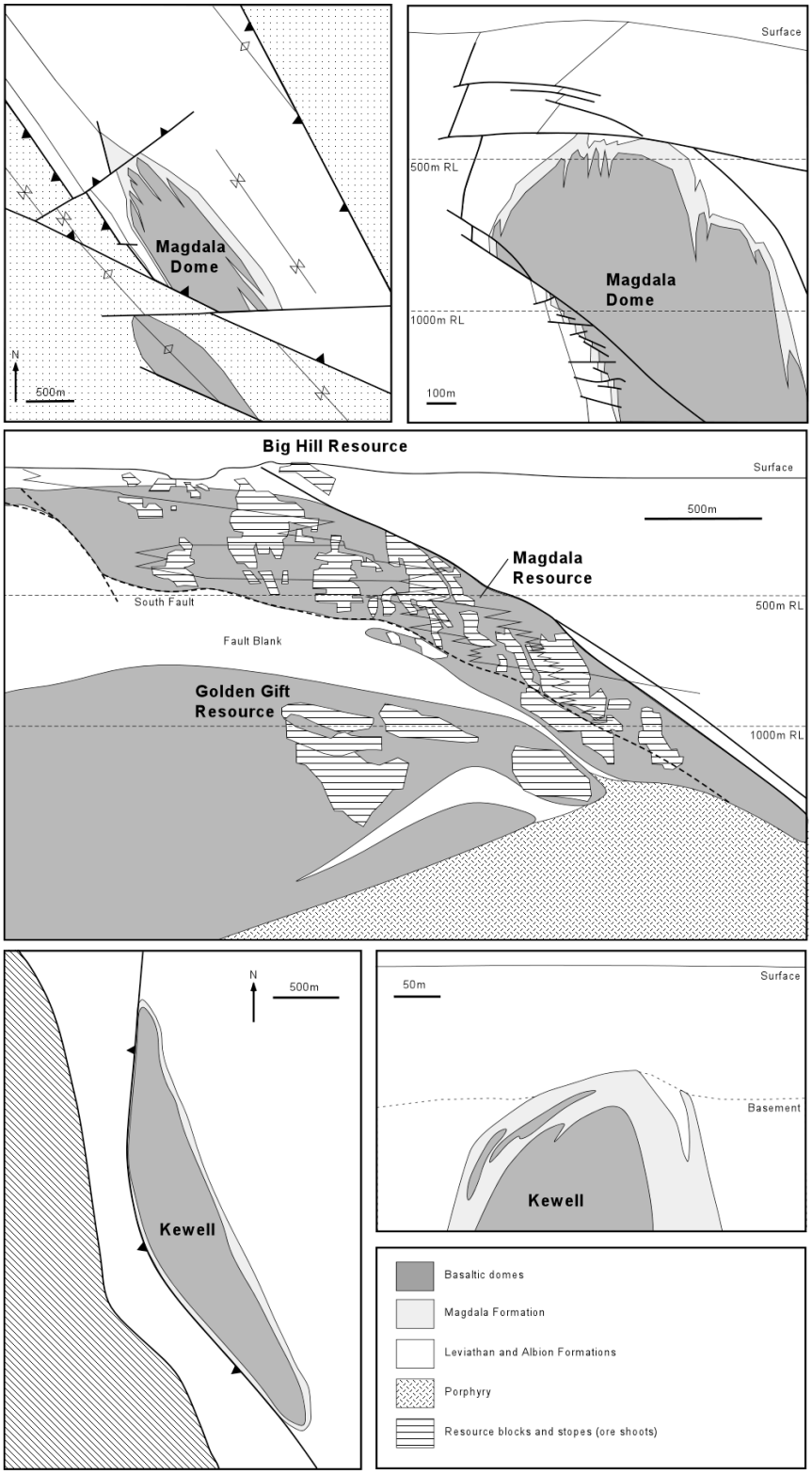

Figure 3-2. Geometry of the: (a) Magdala Dome in plan, (b) Magdala Dome in cross section, (c) Long section of the Magdala Deposit showing steeply plunging shoot geometries defined by historical stopes and reserve blocks, (d) Kewell Dome in plan, and (e) Kewell Dome in cross section (Magdala sections modified after Miller et al. 2002).

Gold mineralisation was coeval with two subsequent brittle deformation events. The first (D_4) resulted in the development of northeast-striking reverse faults due to dominantly east northeast-west southwest directed compression. The second event (D_5) marked a switch to a sinistral shearing environment characterised by tension gashes near the basalt that formed during NW-SE oriented shortening (Figure 3-3). Mineralisation occurs associated with tension gashes along the basalt-Albion Formation contact, within an alteration zone particularly in and adjacent to waterloo structures and associated with laminated quartz veins and faults in the Central Lode and along several linking structures (Miller & Wilson, 2002; Watchorn & Wilson 1989).

The magnitude of deformation at the time of mineralisation was relatively small (Robinson *et al.*, submitted). The deposit was subsequently dismembered by several later brittle faulting events the most significant of which resulted in the formation of the South Fault which was responsible for offsetting the Golden Gift mineralisation from the Magdala mineralisation (Figure 3-2) (Miller & Wilson 2004).

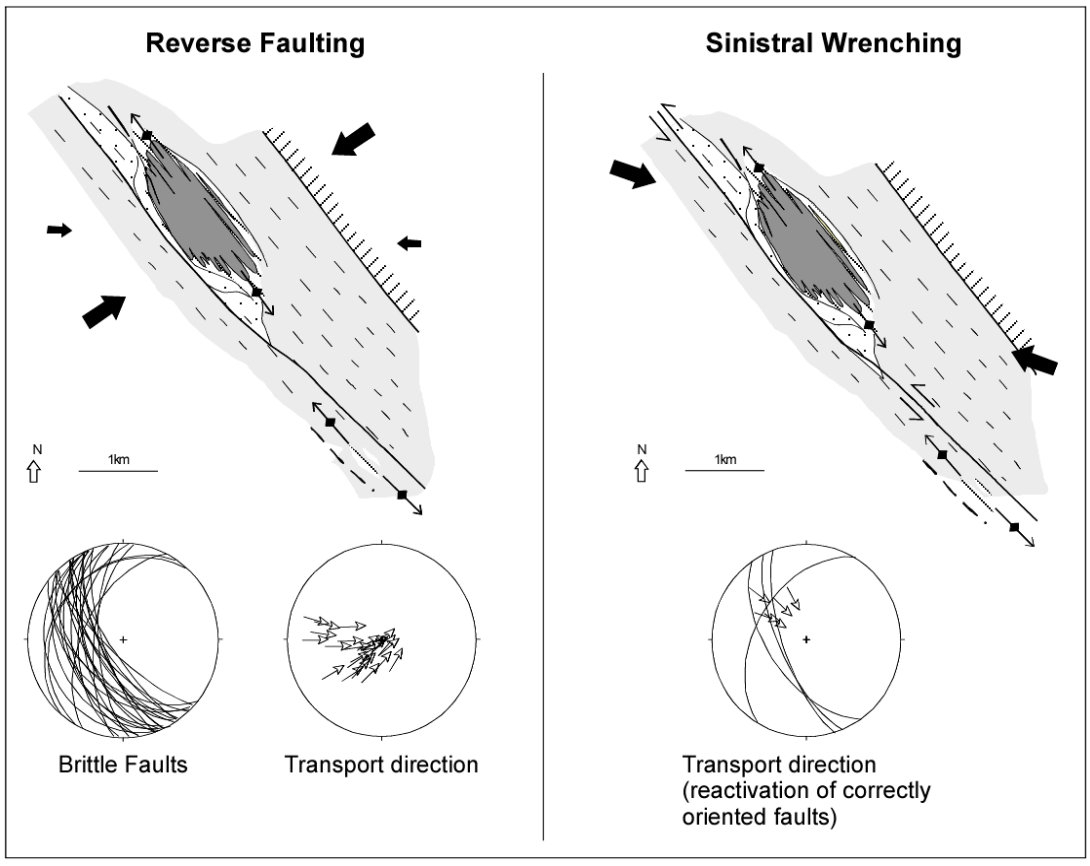

Figure 3-3. Plan view of the effects and orientation of the Au mineralizing D4 and D5 brittle deformation events on the Magdala Dome (modified after Miller et al. 2002)

Strategy for Developing the 'Predictive Discovery Model'

The strategy that has been established is to first develop a strong understanding of a 'Type Locality' through research (Figure 3-4). In doing this the deformation, alteration and metamorphic history, the geometry of critical units, and the petrophysical properties of those units are defined. Numerical simulations are then carried out on this well

defined 'type model' and results of the simulations can be compared with the known deposit geometries and ore grades. This becomes an iterative process where modelling results are compared against ore shells or mineralisation surfaces and changes to model geometries or modelling parameters can be made as required.

Data sets are then acquired in order to constrain the geometries of similar geological features in identified target areas (i.e. by field mapping, potential field data, geochemical drilling, inversion modelling, etc). Realistic 2-D and 3-D models can then be constructed at appropriate scales that may include various alternative interpretations. Numerical simulations are applied to the 'target models' using the (now tested) 'type model' parameters. Drilling programs can then be carried out within the target area to test predicted fertile zones.

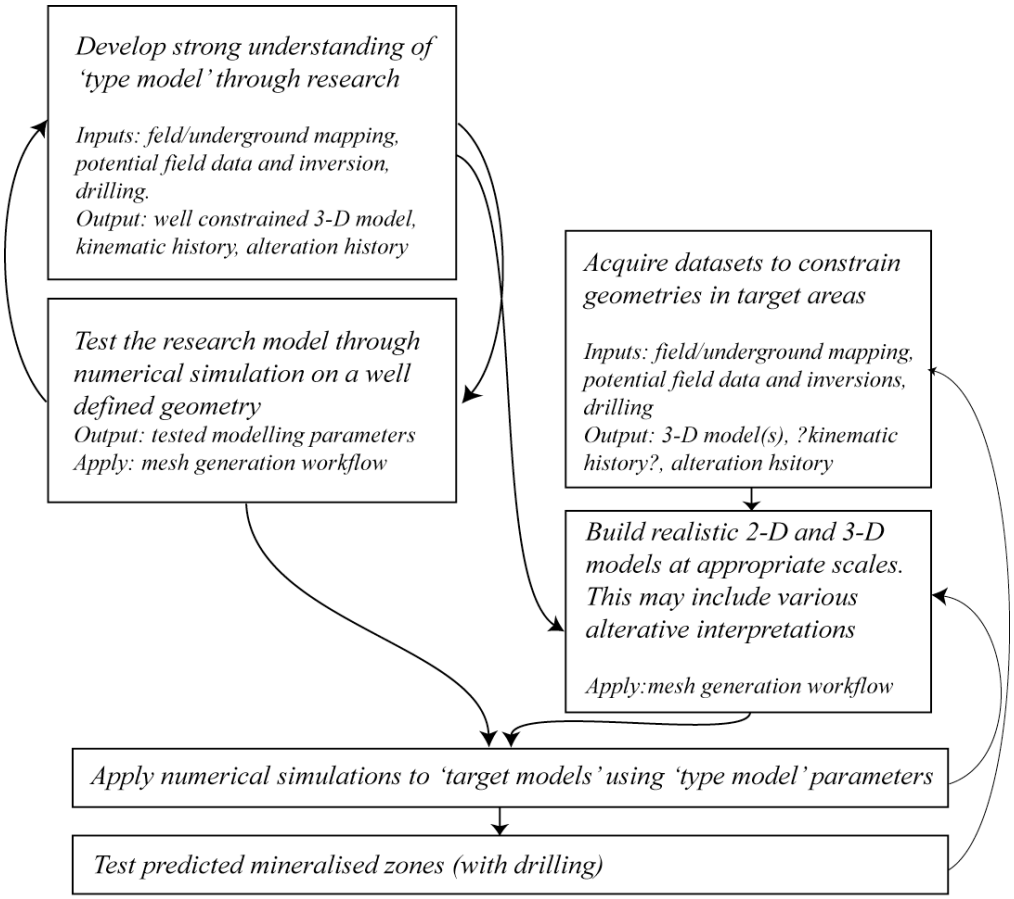

Figure 3-4 Diagramatic representation of the Predictive Discovery Model workflow.

Three Dimensional Modelling

3-D models were initially built of the well constrained Dukes Nose (shoot scale) and Magdala Dome (dome scale) mineralised environments as well as a less well constrained domal target geometry within the Stawell gold belt, the Kewell dome (Figure 3-1). The process of building the models began by defining the critical model elements that would be used as input for the numerical simulations, as well as for visualizing the results of the modelling generating targets. These elements were: (1) the geometry of relevant geological surfaces, (2) petrophysical data regarding the rock types involved and (3) the

orientation of the stress field during gold mineralisation. Whilst items (2) and (3) are not really elements of 3-D geological models they are critical to successful numerical simulation. As a result they were considered during model construction and built into the models where possible.

As these models were primarily to be used as inputs for the numerical simulations they needed to represent an approximation of the geometry at the time of gold mineralisation (D_4). Also transport due to the post-mineralisation brittle deformations, whilst being complicated at the mesoscopic scale (Miller & Wilson 2002), was easily recognized at the macroscopic scale of the models. The effects of these brittle faulting events (in particular South Fault related structures) were removed from the 3-D models when required.

Three major rock types were considered to be critical. These were the basalt (domes), Magdala Facies (altered sediments) and the overlying Albion Formation. Where available existing faults and quartz veins located in the Central Lode, Stawell Fault and Flats Structures in the Magdala system were also modelled. Grade shells were imported for later comparison with modelling results. Erosional surfaces and weathering profiles were included in the Kewell model and the geological surfaces (basalt and alteration halo) were extrapolated above the present erosion level to an approximation of the primary domal geometry.

Numerical Simulation

Numerical simulations have been done using FLAC 3-D. FLAC is an explicit finite-difference code that treats material as continuous and so does not allow the simulation off fluid flow along discontinua such as brittle faults. The Mohr-Coulomb constitutive model (elastic-plastic) was used for all models. Fluid flow obeys Darcy's Law and is affected by changes in deformation induced changes in volume strain that in turn affect pore-pressures and fluid flow velocities. Stress is affected by the changes in pore -pore pressure which completes the feedback loop. We use FLAC because it is one of the few pieces of software that allows deformation - fluid flow coupling in 3-D. It is fairly versatile with its own macro language allowing the user to extend it's capabilities and allows complex geometries to be built. The translation of the mesh from the 3-D modelling package GOCAD to FLAC is done using CSIRO developed software called 3-DMACS.

Numerical simulations have been conducted at the prospect scale on the Dukes Nose system within the Magdala deposit and at the dome scale on the Kewell and Magdala Domes.

All far-field stress directions used in the simulations were derived from the structural analysis done by Miller and Wilson (2002; 2004) and Miller *et al.* (2002). All models were shortened by 5% only as this was deemed to be geologically reasonable given the relatively small amount of transport and deformation associated with the mineralizing events.

The Dukes Nose

The model geometry for the Dukes Nose system was defined by a combination of drilling, underground mapping and to a lesser extent geophysical interpretation. The model was originally built in MineSight by the mine geologists at Stawell Gold Mine and was then imported into GOCAD. The model was simplified in GOCAD and the effects of South Fault aged structures were removed.

As mentioned previously the Dukes Nose region of the Magdala Deposit (Figure 3-5) was chosen as the 'type locality' for the numerical simulation work. This region was chosen because (a) the geometry of the basalt and other units in the region is very well defined by drilling and underground mapping, (b) all of the common geometrical elements were present in the region (i.e. plunging ore shoots, Waterloo's, basalt contacts, quartz vein lodes, 'flats' structures), (c) the deformation history in the region was very well defined, (d) all of the important mineralisation types were present (Dugdale & Wilson submitted), and (e) the region is on the edge of the current mine development so there was potential to add value in this region.

Numerical simulation modelling of the 'type locality' is designed to test assumptions made about model boundary conditions, mechanical properties of rock units, and validity of the simplifications made to the model geometries (Figure 3-5). This is done by running a series of simulations and then comparing the results with the known geology and in particular the ore grade shells.

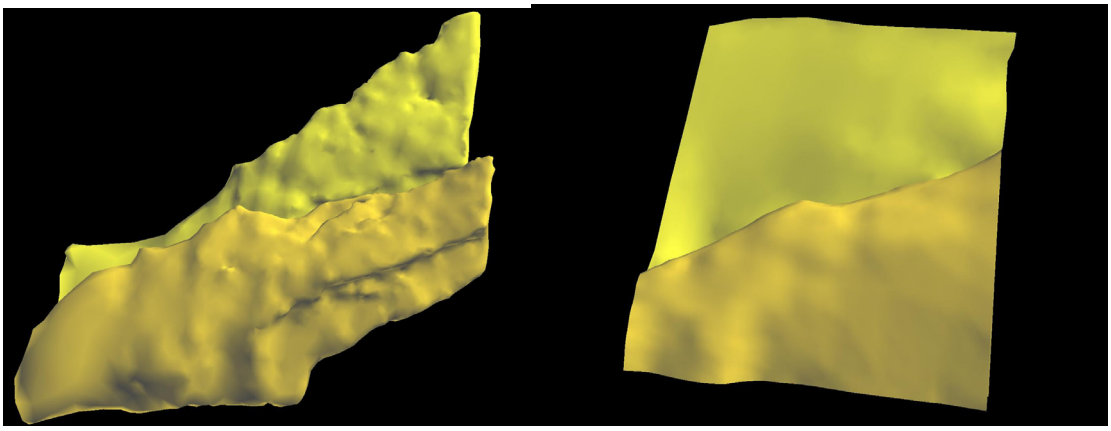

Figure 3-5 (a) 3-D model of the 'real' geometry of the Dukes Nose region as defined by drilling underground mapping; (b) Simplified model of Dukes Nose developed as input for 3-D numerical modelling. Note the smoothing of complex surfaces and removal of post-D4 brittle structures whist retaining the major geometrical elements.

Whilst the development of the Duke Nose models was primarily aimed at doing this testing there were a number of puzzling aspects to the geometry of the ore shoots in the Dukes Nose region. In particular, the apparent oblique plunge of the ore shoots to any significant structural elements in the region. Figure 3-2c is a longitudinal projection through the Magdala system that highlights this very well. The grey regions are mined areas which more or less outline the shoot geometries and their oblique relationship to the basalt noses which plunge much more shallowly to the northwest in this region.

Five models of the Dukes Nose were tested; (i) east northeast – west southwest directed compression alone; (ii) east – west directed compression following east northeast – west southwest directed compression; (iii) east southeast – west northwest compression applied after east – west and east northeast – west southwest compression; (iv) east – west directed compression alone; and (v) east southeast – west northwest compression alone. All models had the same units present and no models contained any pre-existing quartz veining (e.g. central lode). Models were buried to 6 km and all other boundary conditions were the same. The results of each of the different model scenarios are presented and described in more detail in Schaubs *et al*. (Chapter 4).

In the model where compression was directed from the east northeast – west southwest areas of maximum dilation occur within the Magdala Facies unit on the flank of the Dukes Nose basalt and overlain by the Albion Formation. This region of maximum dilation coincides with a thickening of the Magdala Facies unit. This area is also the area with the highest fluid flow rates.

When the compression direction is rotated from east northeast – west southwest directed to east – west directed it cause the areas of maximum dilation to be located within the upper portions of the Magdala Facies high above the Dukes Nose. The region of highest fluid flow also changes position; down plunge along the top of the Dukes Nose. This is caused by the higher fluid pressure gradient within the Dukes Nose towards the northwest end of the model.

Figure 3-6 presents the results of the east – west directed compression following east northeast – west southwest directed compression again superimposed onto the real basalt surfaces (Figure 3-6b). The ore grade shells for the Dukes Nose region have also been added to the model (Figure 3-6c). The green ore shell is the Central Lode 4g/t surface while the blue is the Dukes 4g/t surface. The high grade ore shoots form elongate structures that plunge to the northwest more steeply than does the basaltic nose. This relationship is not necessarily intuitive. However, there is a remarkable correlation, in both geometry and location, of the modelled high shear strain contour, the zones of

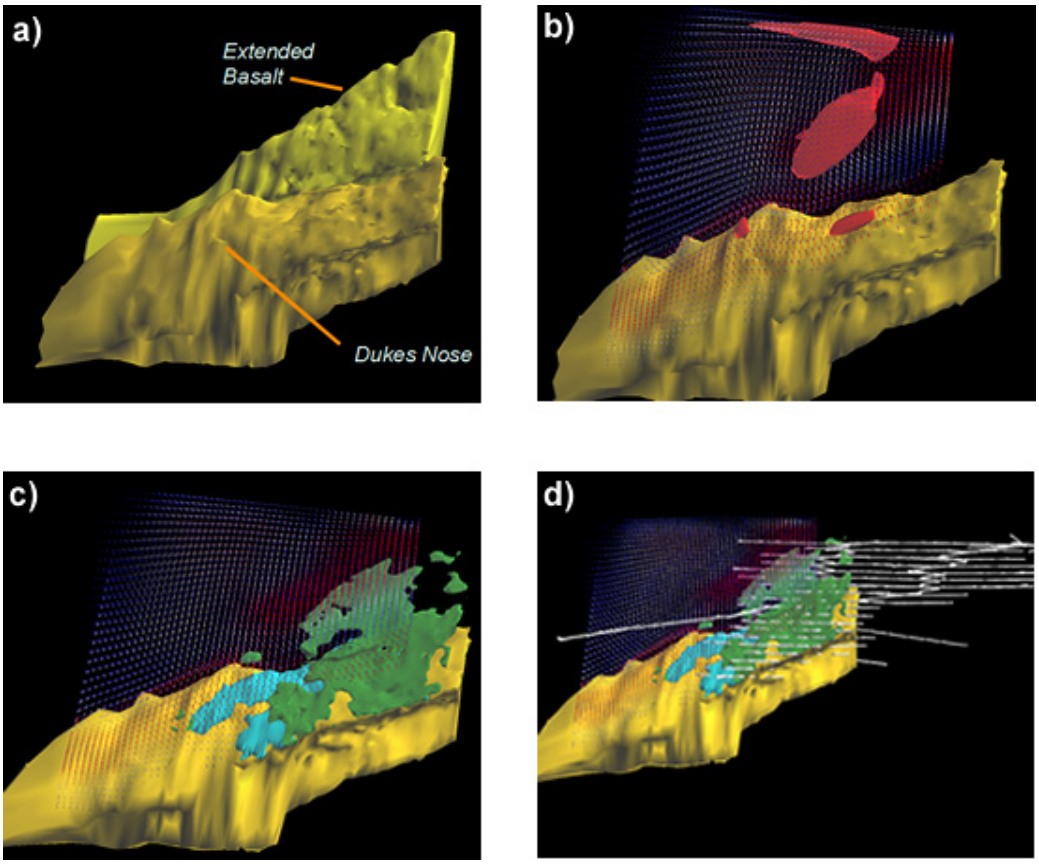

Figure 3-6 Dukes Nose numerical simulation results. (a) Minesight model of Dukes Nose and Extended Basalt, (b) Dukes Basalt with Darcy Flow vectors (red – highest flow rate, blue – low flow rate) and shear strain contour, (c) basalt surfaces with flow vectors and grade envelopes (aqua – Dukes Grade 4g/t, green – Central Lode Grade 4g/t), (d) as above with current mine development.

greatest magnitude fluid flow vectors and the elongations in both the Central Lode and Dukes ore envelopes. This indicates that the location, orientation and geometry of the high-grade ore shoots at Magdala is controlled almost entirely by local geometrical variations rather than larger scale fluid focusing or chemical effects.

The Magdala Dome

A very detailed 3-D model of the Magdala Dome was constructed from a series of serial sections using GOCAD. This model contains all of the Stawell deposits critical rock units and structural elements (see Figure 3-2). The model was then compared with drill core data from the Stawell Gold Mines aQuire database, a kriged basalt surface modelled in MineSight by the mine geologists and isotropic and anisotropic leapfrog models generated from the drillcore database sampled at 1 m intervals. A composite basalt surface was generated utilizing aspects of each of these.

A simplified version of the model was then generated that just contained the critical surfaces for numerical simulations, as described above. Once again in order to use this model in a meaningful way to predict the location of fluid pathways during minerlisation the geometry needed to be restored to a post-D3 state. This first required the removal of the effects of the South Fault aged structures, in particular restoring the displacement

along the South Fault itself, and then the smoothing of the much less significant Early South Fault structures (Figure 3-7).

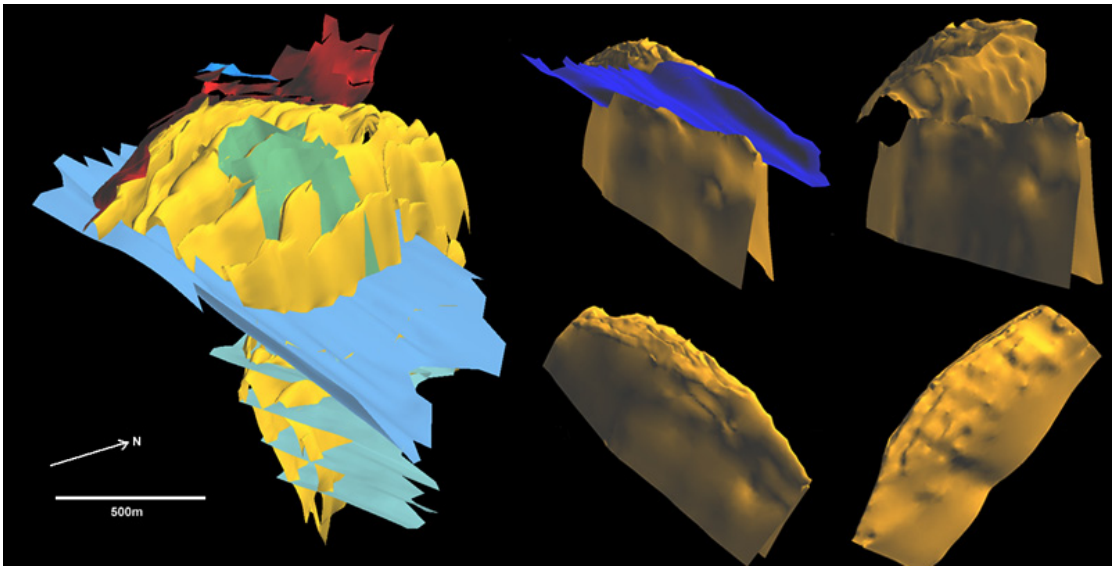

Figure 3-7. (a) The 3-D model of the Magdala Dome. Yellow surface – basalt, red surface – central lode, pale blue surfaces – South Fault and early South Fault aged faults. Volcanogenics have not been included as they mantle most of basalt surface. (b) Reconstructed basalt surface (i) with South Fault, (ii) without South Fault. Effects of minor faults have been removed and the basalt surfaces has been simplified in poorly constrained regions and (iii) The final restored Magdala Basalt Dome. Note the flow lobes on the southwestern flank and the northeast dip in the region of the Golden Gift. The eastern flank of the dome also contains lobes but these have been smoothed out due to a lack of constraining data in this region.

The semi-palinspastic reconstruction was done in gOcad. Transport directions used in the reconstruction were primarily derived from the work of Miller and Wilson (2002; 2004) and Miller *et al*. (2002) but were modified slightly in order to accommodate the modelled geometrical offsets resulting in a realistic unfaulted basalt surface (Figure 3-7).

Reconstructing the dome to a pre-South Fault state raised a number of issues. The major problem was how to deal with the flexure on the interpreted South Fault surface at the southern end of the dome. There are three possible approaches: (1) assume that the flexure is real and that the upper and lower plates in the system deformed as movement occurred on the fault, (2) assume that the South Fault aged faulting in this region is more complex than is modelled and that a wedge of crust is 'missing' (or not modelled), or (3) that a younger steeper dipping structure offsets the South Fault in this region (Figure 3-7).

Given the lack of constraining data in the region concerned it is difficult to distinguish between these possibilities. However, in the hanging wall of the system, where we do have more data, there is no evidence for the significant ductile deformation or accommodation structures that would be required to accommodate the several hundred meters of displacement that is required along a fault with this geometry. Also given the complexity of brittle structures with a similar orientation to the South Fault (Miller & Wilson 2002) it seems likely that geometry of the basalt in the region of the South Fault

flexure would be considerable more complex than is modelled at the macroscopic scale. Finally, whilst data regarding the footwall geometries is sparse, the location of the basalt nose and the basalt contact in the Golden Gift region is known from a series of exploratory deep holes. Given what is known about the geometry of other basalt domes in the belt and the structure of the Wonga Deposit (Miller & Wilson 2004b) reconstructing the dome using either the missing wedge or later fault offset approaches provide the most geologically realistic result.

The reconstructed Magdala Dome surface provided several insights into the geology of the system that may not have been intuitively obvious. First the geometry of the irregularities or noses on the (western) flank of the dome was revealed at the macroscopic scale. These features appear to be discontinuous along strike, quite irregular in the shape and symmetry. They clearly do not resemble asymmetrical folds as on the flank of a major antiform as they had previously been interpreted (Watchorn & Wilson 1989). The overlapping nature of many of these features (Figure 3-7) supports the suggestion that they may in fact represent primary flow lobes associated with basalt deposition (Squire & Wilson 2005). This is supported by the facing direction indicated by pillow basalts in the lobes as described by Henry *et al*. (submitted). The model also shows a number of broader lobes on the eastern flank of the dome but these are largely interpreted and their geometry very loosely defined so no interpretation regarding the nature of these features can be made at this stage.

Another aspect of the domes geometry that was revealed by doing the reconstruction was the thinning of the basalt dome to the southeast. Whilst the geometry of the eastern flank of the dome is not well defined by drill holes the modelling does appear to suggest a thinning of the unit to the south. This has significant implications to the fluid flow simulation results. The geometry of the Magdala Dome at depth remains largely undefined. Three possible alternatives have been proposed: (1) the sides of the dome are relatively straight and steep and continue to depth, (2) the basalt is folded about a pair of bounding synforms and so flares out at depth and folds up into the adjacent West Magdala body and is truncated by the Coongee Fault to the west and east respectively, or (3) the basalt surfaces close back on themselves at depth forming a tongue like structure. Of these the second seems the most likely scenario given geometry and vergence changes in the bounding units on either side of the dome. However, given the first phase of dome scale numerical simulation was designed to investigate fluid flow at the mineralised levels in the system a simple straight sided model was developed initially. Flared and closed models have subsequently been developed as alternate geometries but it is hoped that continued development in the Golden Gift region and new geophysical surveys and interpretation will help define the basalt geometry at depth.

Numerous permutations of the Magdala Dome model were run (with and without the Magdala Facies and several combinations of far field stress orientations). As with the initial Dukes Nose modelling the most geologically reasonable results were generated from a model with a basalt surface mantled with a weaker alteration halo and north northeast – south southwest oriented compression followed by east – west oriented compression. The results of this modelling are presented in Figure 8. Figure 8a presents a volume strain isosurface in yellow that indicates regions that are undergoing dilation. The yellow isosurface is U.gradP which is the scalar product of the fluid pore pressure gradient and the fluid velocity (Schaubs *et al*. Chapter 4). This indicates where pressure sensitive mineralisation might occur (i.e. quartz veins). Figure 3-8b clearly shows that

fluid flow is concentrated in two regions on the southwestern flank of the dome. The north most of these coincides precisely with the location of the central lode mineralisation and the more southerly one sits just above the inferred position of the Golden Gift mineralisation. Also the zone of reduced flow in the section between these zones corresponding with the less well mineralised Federal-Albion section of the deposit as well as the complete lack of high-flow zones on the relatively barren northeast flank of the dome.

In Figure 3-9a the Central Lode grade shell is plotted against the U.gradP isosurface and Figure 3-9b where the Leapfrog 1g/t ore envelope is plotted against the fluid flow velocity vectors for the reconstructed dome models. In both cases the similarity in the location and geometry of the known ore shoots and the predicted zones of high-fluid flow or pressure sensitive mineralisation is remarkable.

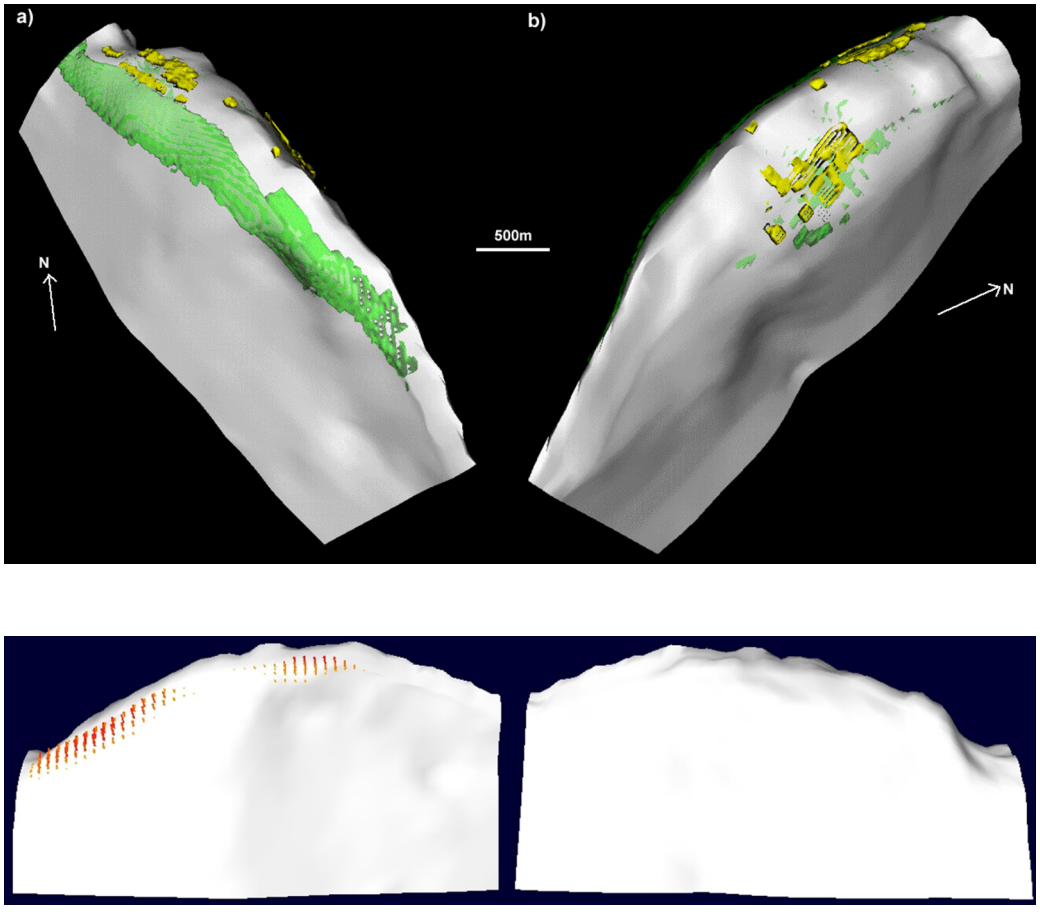

Figure 3-8. (a) Magdala Dome Basalt with U.gradP (green) and dilatant volume strain (yellow) surfaces. The modelling conditions involved NE-SW compression followed by east – west with a Magdala Facies unit present. The U.gradP surface shows regions where pressure sensitive mineralisation might occur (i.e. quartz veining). (b) Magdala Dome Basalt with Darcy fluid flow vectors shown in the zones with high fluid flow rates. The modelling conditions involved NE-SW compression followed by east – west with a Magdala Facies unit present. First view is to the NE and second to the SW. Note the coincidence of the northeastern-most zone of high flow with the mineralised and developed parts of the mine. The more southwestern zone sits just above the northeast dipping Golden Gift region.

One of the striking features of the mineralisation at the Magdala Deposit is its asymmetrical nature. The northwestern section of the southwest flank of the dome is strongly mineralised, whereas the northeastern flank is barren. Again this is not necessarily intuitive as analysis of the dome suggests it is relatively symmetrical and one would expect to see matching mineralisation zones on opposing flanks of the dome if purely mechanical flow focussing processes where most critical. However, the fact that numerical deformation and fluid flow simulations predicted this variation suggests that there is enough asymmetry in the shape of the dome to restrict the dilatant zones and high fluid-fluxes to one flank. Closer inspection of the domal geometry shows that there is a substantial thinning of the dome to the south as well as a number of perturbations in the shape of the axis of the dome and that these must be significant enough to partition strain along the mineralised flank.

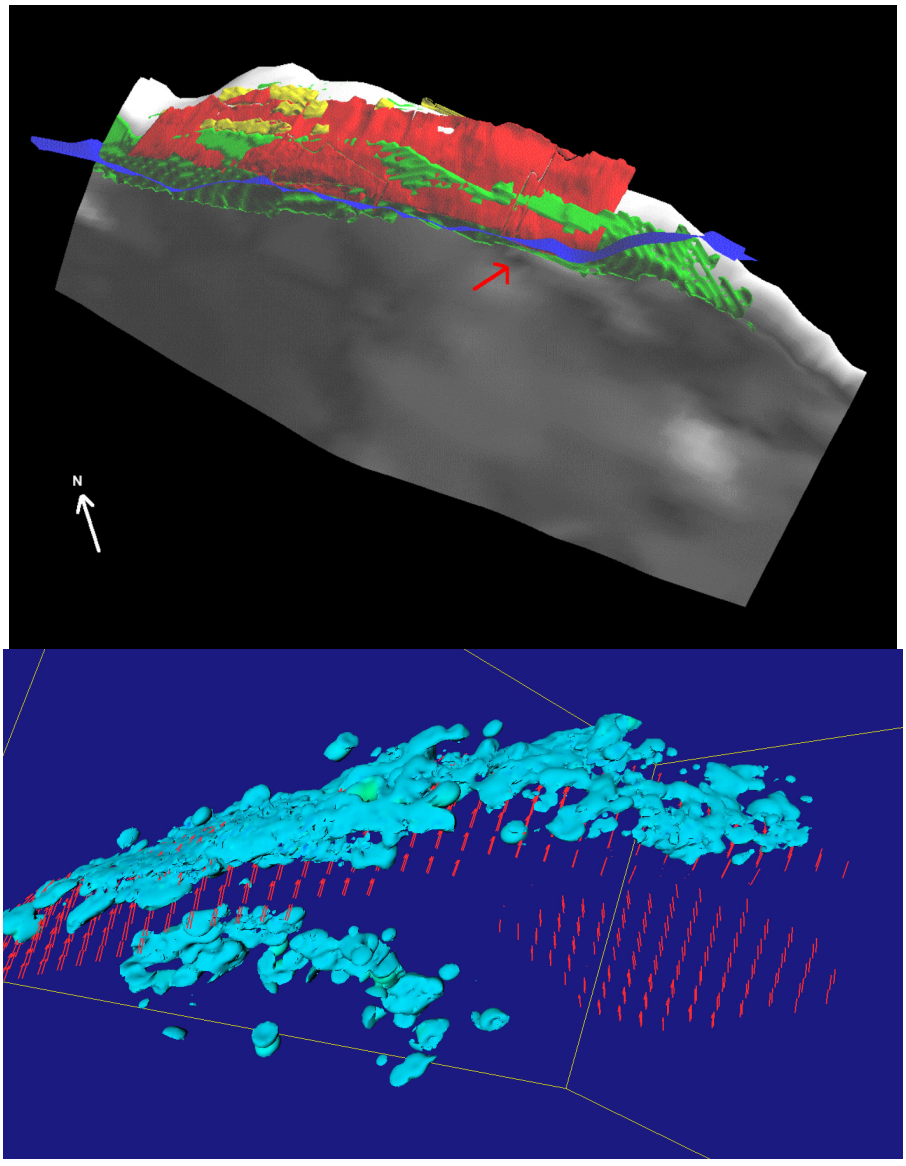

Figure 3-9 – (a) Magdala Dome with South Fault surface (blue) and modelling results (as described in Figure 12) superimposed onto the Central Lode grade shell (red). Red arrow marks approximate position of the Golden Gift deposit. (b) Darcy flow vectors overlain with Leapfrog 1g/t ore shell.

Figure 3-10 presents some of the modelling results after having been 'refaulted' into their interpreted present day positions. This involved slicing the model with the South Fault and then undoing the reconstruction described above. Note the small section of the U.gradP surface that has been offset by the refaulting into the footwall sequences to the South Fault in a location not far to the southwest of the Golden Gift mineralisation.

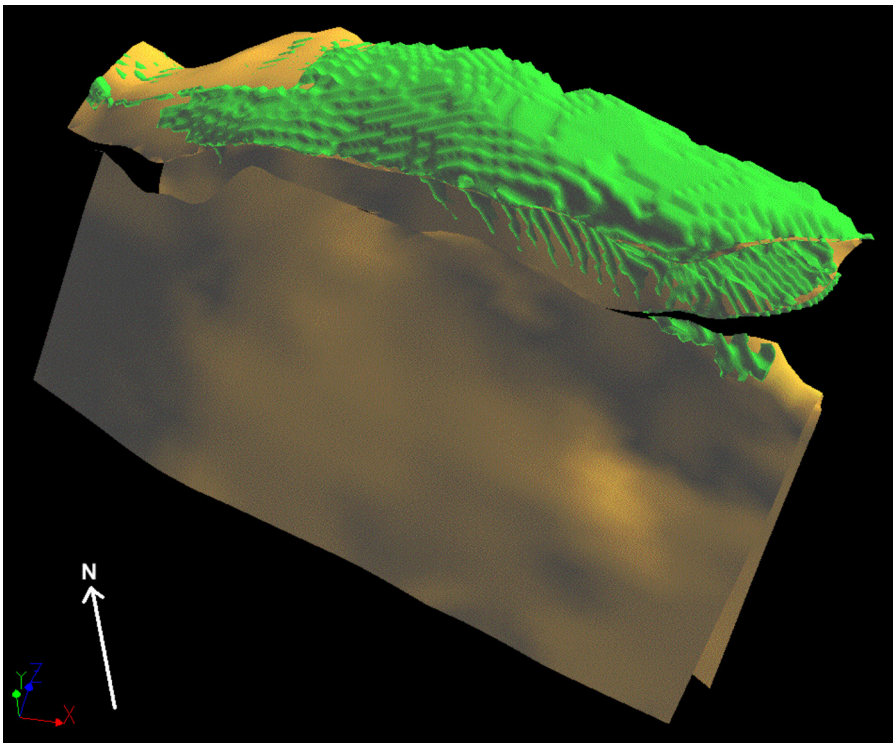

Figure 3-10 Re-faulted Magdala Basalt Dome with re-faulted U.gradP surface for the NE-SW compression with Magdala Facies present model.

The Kewell Dome

The Kewell dome was chosen as a target localities for a number of reasons: (1) it is located in the same structural position within the Stawell Zone as the Magdala Dome, (2) whilst there were some differences in aspect ratio it largely has similar domal geometries to the Magdala Dome and its geometries were relatively well defined, (3) the dome has been targeted using classical geophysical and drilling techniques and the modelling may allow refinement of the drilling strategies.

Four scenarios for the Kewell Dome were tested; the absence /presence of the Magdala Facies equivalent (Dugdale *et al.* this volume), the presence of a minor basalt lobe on the flank of the major basalt dome and a change in compression direction from east northeast – west southwest to east – west (Figure 3-11). The presence of the Magdala Facies (which are given weaker mechanical properties than the matrix or the basalt) causes the absolute values of dilation and fluid flow to increase; however, the relative position of areas of dilation and high fluid fluxes with respect to the position of the dome does not vary greatly. The Magdala Facies are areas of contraction on the flanks of the basalt

dome where the dip is steep and at a high angle to the compression direction. Towards the top of the dome the Magdala Facies become areas of dilation. This causes fluid flow rates to be highest close to the top of the dome where areas of contraction and maximum dilation are in close proximity. Contraction occurs within the matrix above the highest point of the dome.

The presence of a thin basalt lobe on the flank of the major basalt dome causes the region above the basalt lobe within the intervening Magdala Facies (between the basalt) to become the region with the highest fluid flow rates (Figure 3-11). As in the simplified Dukes Nose models this occurs because the Magdala Facies separating the basalt bodies is contracting and is an area of high fluid pressure. Fluid is forced up this thin unit towards the area of dilation which occurs within the Magdala Facies near the top of the basalt lobe. Areas of maximum dilation still occur near the top of the main basalt dome but the fact that the intervening Magdala Facies are contracting and have high permeability cause high fluid flow rates to be localised above the minor lobe.

Changing the compression direction from east northeast – west southwest to east – west cause the areas of maximum dilation to be decreased in volume relative to the model were only east northeast – west southwest compression is applied. The location of highest fluid flow rates is also shifted. In both models the highest fluid flow rates occur near the highest portion of the dome; however, in the model where compression is applied east – west, the highest rates occur on the east northeast side as opposed to the west southwest.

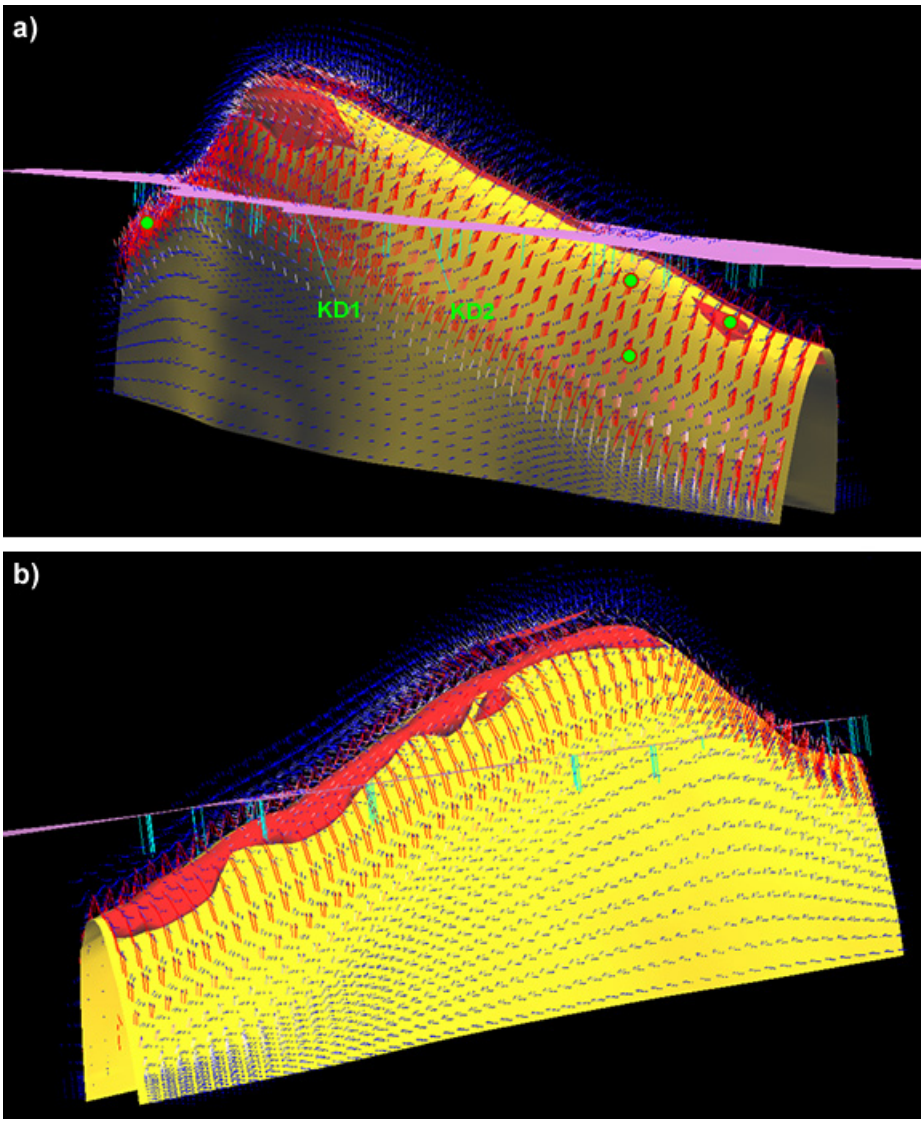

Figure 3-11 Kewell Dome numerical simulation results. Yellow surface – basalt, red surface – shear strain contour, mauve surface – ground level, fluid flow vectors (a) North directed view (b) East directed view. Existing diamond holes KD1 and KD2 are marked as are the proposed diamond hole locations (green circles). Dome is 3.5km in length.

Outcomes

In the shoot and dome scale models the presence of the Magdala Facies (which are given weaker mechanical properties than the matrix or the basalt) causes the absolute values of dilation and fluid flow to increase; however, the relative position of areas of dilation and high fluid fluxes with respect to the position of the domes does not vary greatly.

The Magdala Facies are areas of contraction on the flanks of the basalt dome where the dip is steep and at a high angle to the compression direction. Towards the top of the domes the Magdala Facies become areas of dilation. This causes fluid flow rates to be highest close to the top of the dome where areas of contraction and maximum dilation are in close proximity.

The presence of thin basalt lobes on the flanks of the domes cause the region above the basalt lobes, within the intervening Magdala Facies, to become the region with the highest fluid flow rates. This occurs because the Magdala Facies separating the basalt bodies is contracting and is an area of high fluid pressure. Fluid is forced up this thin unit towards the area of dilation which occurs within the Magdala Facies near the top of basalt lobe. Areas of maximum dilation still occur near the top of the main basalt dome but the fact that the intervening Magdala Facies are contracting and have high permeability cause high fluid flow rates to be localised above the minor lobe.

In the Magdala deposit the rotation of the compression direction from east northeast – west southwest directed to east – west directed causes the locus of maximum dilation to be located within the upper portions of the Magdala Facies high above the Dukes Nose. The region of highest fluid flow also changes position; down plunge along the top of the Dukes Nose. This is cause by the higher fluid pressure gradient within the Dukes Nose towards the Nnorthwest end of the model.

Application of Predictive Discovery Models in Exploration

Dome scale targets

Numerical modelling of the Dukes Nose region and the reconstructed Magdala Dome showed that there is a strong correlation between the areas of predicted high U.gradP values and areas of elevated fluid flow velocities and the location and geometry of gold mineralisation at two scales.

Prior to commencement of the numerical simulation work the Kewell Dome was considered a potential analogue to the Magdala Deposit. As such the only diamond drilling that had been done on the deposit was targeting mineralisation on the steeply dipping western flank of the dome. Of the two diamond holes that had been drilled KD1 intercepted steeply dipping basalt on the western flank beneath the level or an interpreted basaltic nose (Figure 3-11). KD2 was a slightly shallower hole that intersected the basalt nose and then penetrated a ‘waterloo’ structure before hitting the basalt dome proper. KD1 was virtually barren and KD2 had a few mineralised intercepts but did not find any continuous regions of grade.

When the location of the KD1 and KD2 holes were analysed in conjunction with the numerical modelling results it was noted that KD1 actually intercepted the basalt contact below the regions of predicted elevated fluid flow velocities whilst KD2 intercepted a zone of relatively elevated flow velocities. Hence the drilling results confirmed the relationship between the elevated flow velocities and zones of Au mineralisation in these environments.

As a result a new diamond drilling program was designed for the Kewell dome that targeted regions with predicted high fluid flow velocities and corresponding elevated U.gradP values (Figure 3-11). KD3 was drilled west to east at -60º and intersected laminated and brecciated hangingwall quartz reefs with footwall tension veins followed by strongly mineralised Magdala Facies with variable silicification and coarse pyrite, a basalt nose and a strongly mineralised volcanogenic Waterloo. The Waterloo includes a zone with pyrrhotite-chalcopyrite-arsenopyrite bearing tension veins containing visible gold. Subsequent assays revealed continuous zones with gold grades of around 9 g Au/t

in Hangingwall lode settings, 2 g Au/t in basalt contact settings and >12 g Au/t in tension vein arrays in Magdala Facies with visible gold. Interpretation suggests that KD3 intersected a 'Magdala style' mineralized sequence with Central Lode, basalt contact and Waterloo environments on the west flank of a basalt dome. Subsequent drilling delineated a series of mineralised zones concentrated on the SW flank of the dome and plunging away to the south (Figure 3-2e).

Conclusions

Three dimensional numerical simulation of syn-mineralisation rock deformation and fluid flow in the Magdala Deposit at Stawell accurately predicted the location and geometry of known mineralisation. At the macroscopic scale the location of all of the mineralised zones in the Magdala System were predicted using these techniques on geometrical grounds alone. Whilst it is clear that at the mesoscopic and microscopic scale chemical processes played a very big role in the fertility of the host rocks there is no need to consider anything other than geometrically and mechanically controlled fluid focusing mechanisms when considering/predicting the location of potentially mineralised sites at the larger scale.

Application of similar simulations in prospective regions with less well constrained geometries can substantially inform the exploration process. Modelling of the Kewell dome predicted that the plunging noises of the dome may have been sites of localised fluid flow at the time of minersalisation. Drilling these targets resulted in the discovery of a new mineralised zone in a previously explored region under 120m of Murray Basin cover.

References

DUGDALE, A.L. AND WILSON, C.J.L. 2005 Unravelling the alteration history associated with the gold mineralisation in the Magdala Mine Stawell. (this volume)

GRAY D.R. 1988. Chapter 1: Structure and Tectonics. *In:* Douglas J. & Ferguson J. eds. *Geology of Victoria*, pp. 7-18. Victorian Division of the Geological Society of Australia.

HENRY D.A., SQUIRE R.J., WILSON C.J.L., & RAWLING T.J., 2005 Controls on high-grade gold deposit associated with the Hangingwall Reefs, Stawell, western Victoria (this volume).

MILLER, J. MCL, L. J. DUGDALE, AND C. J. L. WILSON. 2001. Variable hangingwall palaeotransport during Silurian and Devonian thrusting in the Western Lachlan Fold Belt; missing gold lodes, synchronous Melbourne trough sedimentation and Grampians Group fold interference. *Australian Journal of Earth Sciences* 48, 901-909

MILLER, J. MCL, AND C. J. L. WILSON. 2002 The Magdala Lode System, Stawell, southeastern Australia; structural style and relationship to gold mineralization across the Western Lachlan Fold Belt. *Economic Geology and the Bulletin of the Society of Economic Geologists* 97, 325-349.

MILLER, J. MCL. & WILSON, C.J.L., 2005 Structural setting and timing relationships of the Victorian gold deposits. *(this volume)*

MURPHY, B. RAWLING, T.,WILSON, C.J.L., MILLER, J. MCL. AND DUGDALE, L. J. 2005 Three-dimensional geological model of western Victoria. *(this volume)*

PHILLIPS N.G. AND HUGHES M.J. 2003 Gold in Victoria; a summary. Victoria undercover-Benalla 2002; conference proceedings and field guide; Collaborative geoscience in northern Victoria. April 30-May 2, 2002 65-69.

ROBINSON, J., WILSON C.J.L. AND RAWLING, T., 2005 Numerical modelling of an evolving gold system: Structural and lithological, controls on ore shoot formation within the Magdala Mine, western Victoria. *(this volume)*

SCHAUBS, P.M., RAWLING, T., DUGDALE, L. J. AND WILSON, C.J.L. 2005 Factors controlling the location of gold mineralisation around basalt domes:insights from deformation-fluid flow models *(this volume)*

SQUIRE, R. J. & WILSON, C.J.L., 2005 Palaeotectonic and palaeogeographic evolution of the Cambrian successions of western Victoria. *(this volume)*

VANDENBERG A.H.M., WILLMAN C.E., MAHER S., SIMONS B.A., CAYLEY R.A., TAYLOR D.H., MORAND V.J., MOORE D.H., & RADOJKOVIC A. 2000. The Tasman Fold Belt System in Victoria. Geological Survey of Victoria Publication. Melbourne, 462. pp.

WATCHORN R.B. & WILSON C.J.L. 1989. Structural setting of the gold mineralisation at Stawell, Victoria, Australia. *Economic Geology* Monograph 6, 292-309.

WILSON C. L. J., WILL, T. M., CAYLEY R. A & CHEN S., 1992. Geological framework and tectonic evolution in western Victoria, Australia. Tectonophysics, v. 214, p. 93-127.

Chapter 4 : Factors controlling the location of gold mineralisation around basalt domes in the Stawell corridor: insight from 3-D deformation – fluid-flow numerical models

P.M Schaubs, T.J. Rawling, L.J Dugdale & C.J.L Wilson

Summary

We present 3-D deformation – fluid-flow models which place constraints on the importance of basalt dome shape and interpreted syn-mineralising shortening direction in localising gold mineralisation around basalt domes in the Stawell Corridor, Western Victoria. Gold mineralisation in the Magdala ore-body at the Stawell Mine occurs predominantly within a thin metasomatised unit named the Magdala Facies that blankets the basalt domes and also occurs in close proximity to parasitic fold-like basalt lobes on the basalt domes. In dome scale models which do not contain basalt lobes, areas with the maximum fluid flow rates occur on the tops of the flanks of the domes where there is a dramatic change in dip of the basalt, and a change from contraction to dilation which creates a significant pore pressure gradient. In models, which contain basalt lobes the location of high fluid flow, rates are strongly controlled by the presence of these lobes. High fluid pressure gradients are created between the contracting Magdala Facies within the area between the lobe and the main domes and those areas dilating above. Areas of significant dilation occur on the shallow dipping portion at the top of the dome and cause fluid to flow towards them. Areas which have significant dilation are also areas of tensile failure in some cases and are coincident with areas of known quartz vein associated mineralisation. In the Magdala Dome models only the east-northeast – west-northwest and east-west shortened models record high fluid flow rates in areas of known mineralisation which is consistent with the interpreted syn-mineralisation shortening directions. Therefore in this situation fluid flow rates during east-northeast – west-northwest and east-west shortening can be used to indicate the potential location of gold mineralisation. In numerical models of the Kewell Dome (a prospect to the north), the position of areas of high fluid flow rate when shortened in the east-northeast – west-northwest and east-west direction, combined with information from limited drilling indicated the potential for gold mineralisation at the south-west end of the dome. Diamond drill holes in this area yielded significant gold values.

Introduction

We present the results of coupled deformation – fluid-flow numerical simulations which are used to test the effects that varying shortening directions (far-field stresses), and basalt dome shape have on the location of regions of significant dilation and fluid-flow rates with respect to gold mineralisation around the basalt domes at

Stawell, Western Victoria. The strategy that we have adopted is to use the strong understanding of a type model to "re-engineer" the known deposit, where the deformation, alteration and metamorphic history are well understood (e.g. Miller & Wilson 2002; Dugdale & Wilson, submitted). Numerical models have been constructed based on this knowledge and results of the simulations have been compared with the known deposit geometries and grades. In this way we have determined some of the critical factors that are important for localising mineralisation at the Magdala mine based on the criteria of dilation and fluid-flow rates. Areas of dilation and high fluid flow rates within the models are interpreted as having a greater potential for gold mineralisation. Newly acquired data (i.e. potential field data, inversion modelling, diamond and air-core drilling) were then used to constrain the geometries of similar geological features in identified target areas, below sedimentary cover. Realistic 3-D models were constructed at appropriate scales and include various alternative interpretations. Numerical simulations were then applied to the 'target models' using the (now tested) 'type model' parameters. Drilling programs were then carried out within the target area to test predicted fertile zones. We have used the Magdala Deposit as our type model and modelled it at 2 scales – ore shoot (Dukes Nose area ~ 800 m) and the entire dome (~4 km). The results of these models were then compared to models of the Kewell and Wildwood Domes (Figure 4-1) - two basalt domes and prospects that lie to the north of Stawell under the cover of the Murray Basin

Geological setting

The Stawell corridor and the Magdala mine are located in a reworked Cambrian orogenic zone that exists between the Lachlan and Delamarian orogens (Miller *et al.*, in press; Figure 4-1a). Within the Stawell Zone, basalt domes with associated gold mineralisation occur within a ~15 km wide region bounded on the west by the east dipping Moyston Fault and on the east by the west dipping Coongee Fault (Figure 4-1b). These domes are made up of massive to pillowed tholeiitic basalt (Squire & Wilson, in press) which are overlain by a unit of rocks termed the Magdala Facies (Dugdale & Wilson, submitted) previously referred to as the 'Volcanogenics', which are made up of variable amounts of calcareous sandstone, chert, sulfidic mudstone, black mudstone and quartz-rich sandstone and are interpreted to have been altered prior to mineralisation (Watchorn & Wilson 1989). East of the Coongee Fault, the St. Arnaud beds (Figure 4-1b) are made up of less deformed and metamorphosed sandstone and shale (Leader *et al.,* this volume).

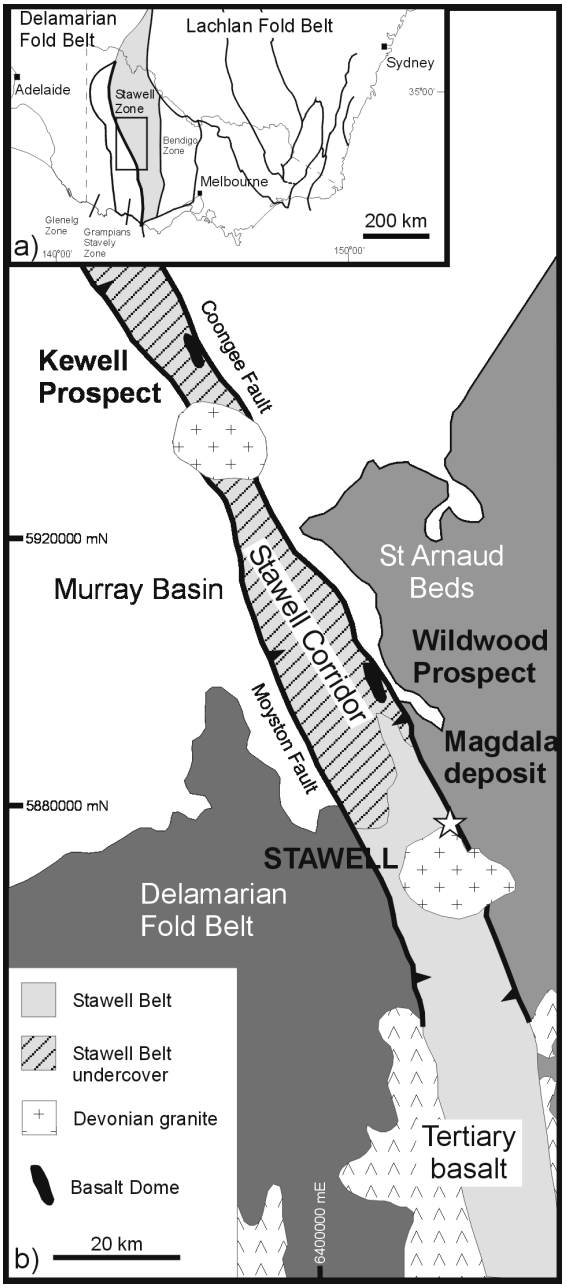

Figure 4-1 a) Simplified geological map of southeastern Australia focussing on the Western Lachlan Fold Belt. Modified after VandenBerg *et al.* 2000. b) Geological map of area surrounding Stawell.

At the Stawell Mine, gold mineralisation within the Magdala ore-body occurs primarily on the west flank of the Magdala Dome; a northwest trending, ~ 4000 m long, doubly-plunging basalt edifice. On the flanks and top of the dome are a number of basalt lobes that resemble parasitic folds but are thought to represent primary flow lobes formed during the extrusion of the basalt (Squire & Wilson, in press). The unit termed the Magdala Facies mantles the basalt dome and occurs between the basalt lobes as cusp like synforms (Figure 4-2). Metasedimentary rocks surrounding the Magdala Dome have been divided into two units: the Albion Formation and Leviathan Formation (Squire & Wilson, in press). The Leviathan Formation is more psammitic and has more foliation parallel quartz veins than the other schists, while the Albion

Formation is more pelitic and the Eastern schist contains interbedded shale and sandstone (Miller & Wilson 2002).

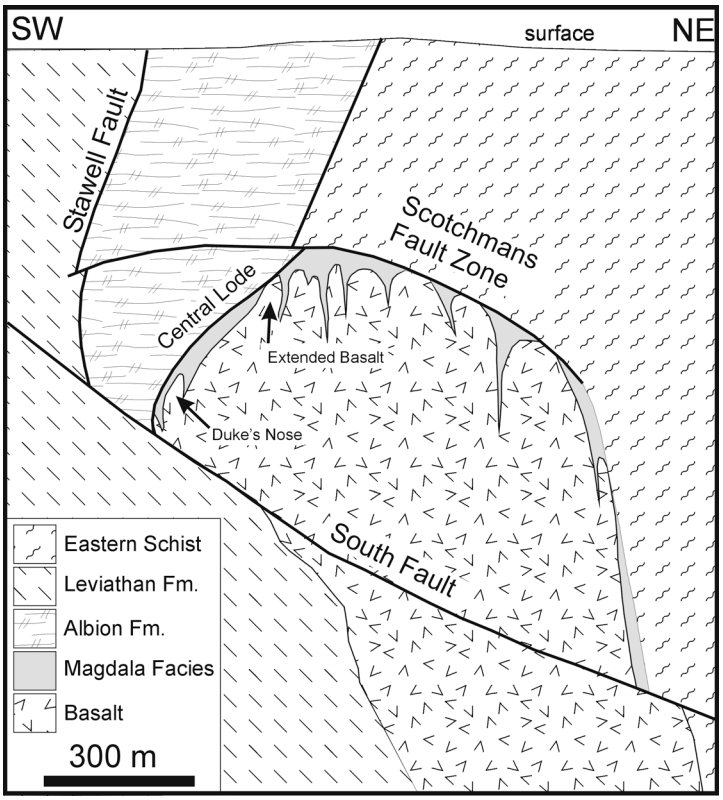

Figure 4-2 Cross-section through the Magdala antiform at section 320. Note location of "Dukes Nose" and "Extended Basalt" basalt lobes on the west flank of the dome.

The deformation history at the Magdala mine has been well documented (Watchorn & Wilson 1989; Miller *et al.* 2001; Miller & Wilson 2002; Miller & Wilson 2002; Miller & Wilson 2004a). Three early ductile deformation events predated the gold mineralisation and produced a variably developed layer parallel schistosity, upright folds with a strong axial planar fabric and a differentiated crenulation cleavage and refolding respectively. Gold mineralisation was coeval with two subsequent brittle deformation events. The first (D_{4a}) resulted in the development of NE striking reverse faults due to dominantly east-northeast – west-southwest directed contraction which is interpreted to have rotated to east – west (D_{4b}). The second event (D_5) marked a switch to a sinistral shearing environment characterised by tension gashes near the basalt that formed during northwest - southeast oriented shortening. The northwest striking and northeast dipping South Fault is interpreted to have been active during D_6 deformation and offset the Magdala Antiform (Miller *et al*., 2001; Miller &Wilson, 2004a).

Gold mineralisation

Gold occurs in a number of structural settings and locations within the Magdala ore-body including the Central and Golden Gift Lodes. Mineralisation occurs primarily within the Magdala Facies and associated structures, while little occurs within the basalt itself. The Central Lode occurs on the west flank of the dome at the contact between the Magdala Facies and the Albion Formation. The Golden Gift Lodes occur on the offset portion of the Magdala Antiform below the South Fault (Miller *et al*.,

2001; Miller &Wilson, 2004a). Mineralisation is also associated with the Hangingwall lodes and Stawell Fault that lie to the west of the Magdala Antiform (Henry *et al.*, submitted). In this paper attention is drawn to the significance of the Dukes Nose and the overall shape of the basalt domes in localising the distribution of the gold. More detailed descriptions of the gold mineralisation at Stawell can be found in the work of Watchorn & Wilson, 1989, Mapani & Wilson, 1995; Fredericksen & Gane 1998; Gane 1998; Mapani & Wilson, 1998; Wilson *et al*., 1999; Miller *et al*., 2001; Miller & Wilson; 2002, 2004a, 2004b.

Modelling Scenarios

Based on the geological information and interpretations of Miller and Wilson (2002) there are a number of factors that appear to be important in localising gold mineralisation from a deformation – fluid-flow point of view. These are: (i) the shape of the basalt dome and the presence of basalt lobes; (ii) the orientation of the stress field during gold mineralisation.

The aim of the numerical models is to gauge the relative importance of these factors in areas of known mineralisation and to determine how we may predict areas of new mineralisation in prospective basalt domes along the Stawell corridor (Figure 4-1). Therefore to assess the above factors the following two questions have been posed.

What is the effect of varying basalt dome shape?

With this question we aim to determine the effects of the overall shape of the basalt domes on focussing areas of dilation and high fluid-flow rates. We wish to know which portions of the dome are better than others and how the patterns change from dome to dome (i.e. Magdala, Kewell, and Wildwood). We also explore the effects of the presence of basalt lobes and intervening Magdala Facies on the flanks of the Magdala and Kewell Domes.

What is the effect of changing the orientation of far-field stresses?

Gold mineralisation is interpreted to have occurred during D_4 deformation which began with an east-northeast – west- southwest orientation and rotated clockwise with the peak of mineralisation coincident with east - west shortening. For completeness we have applied 5 different shortening orientations to each of the models: northeast - southwest, east-northeast – west-southwest (D_{4a}), east - west (D_{4b}), and east-southeast – west-northwest (D_5) and southeast - northwest to determine the effects of changing shortening direction. Again we are interested in determining where regions of dilation and high fluid-flow rates are focussed. All models were deformed to 5 % shortening as the structural observations of Miller and Wilson (2002) suggest that the mineralising events were associated with small strain.

Model setup and Numerical Modelling Methods

Numerical simulations

The three-dimensional, finite-difference code FLAC3D (Fast Langrangian Analysis of Continua) has been used to place constraints on the deformation and fluid -flow. FLAC3D is an explicit finite-difference code (e.g. Desai & Christian 1977), which

treats materials as continuous. The code operates by time-stepping, whereby areas are given initial stress and velocity values and then, after each time-step, strain rates are derived from the velocities and new stresses are calculated from these strain rates. The values are recalculated and updated after equations of motion are applied. The fluids in FLAC3D obey Darcy's Law (see Bear & Verruijt 1987) and deformational induced changes in volumes are used to calculate changes in pore-pressure. Materials were modelled following the elastic-plastic Mohr-Coulomb constitutive model. Other descriptions illustrating the use of FLAC in modelling deformed ore-deposits are presented in Ord & Oliver 1997; Ord *et al.* 2002; Schaubs & Zhao, 2002 and Sorjonen-Ward *et al.* 2002.

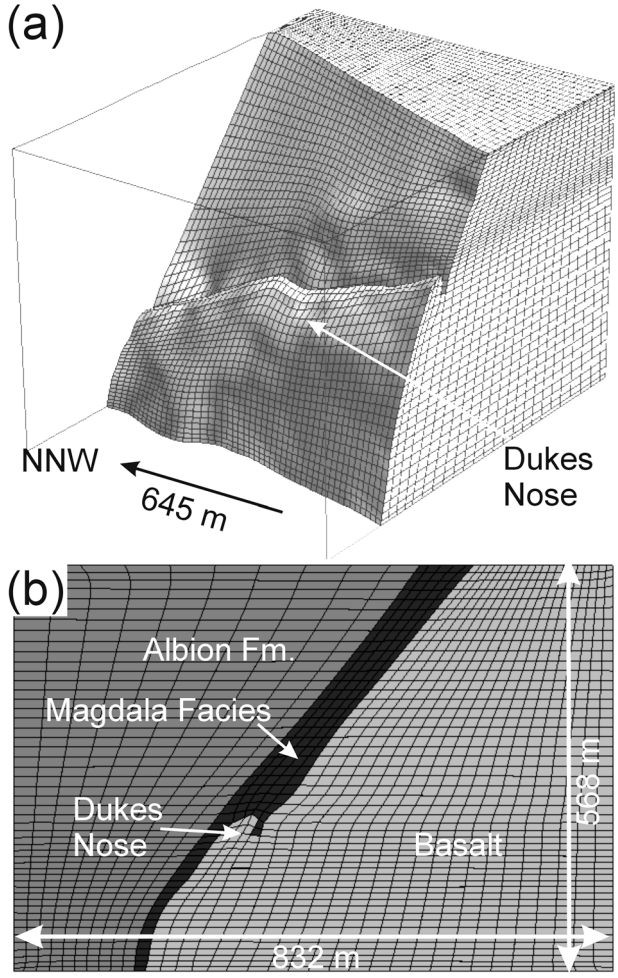

Figure 4-3. a) Outline of basalt for the model of the Dukes Nose. B) Cross-section through the centre of the Dukes Nose model.

Model Geometry

The Dukes Nose model is 832m wide, 568 m tall and 645 m deep with an orientation to the north-northwest (Figure 4-3). It consists of Albion Formation on the west side and basalt on the east. A thin unit of Magdala Facies occurs in the middle to the west and above a lobe of basalt which is the "Dukes Nose" and has a maximum thickness of ~60 m. This basalt lobe plunges to the north-northwest at an angle of ~30^{o}. The basalt on the east side of the model represents the rest of the Magdala Dome and although the Extended Basalt (another basalt lobe) occurs in this area it is not

incorporated into the model other than a slight 'bump' where the crest of the Extended Basalt occurs.

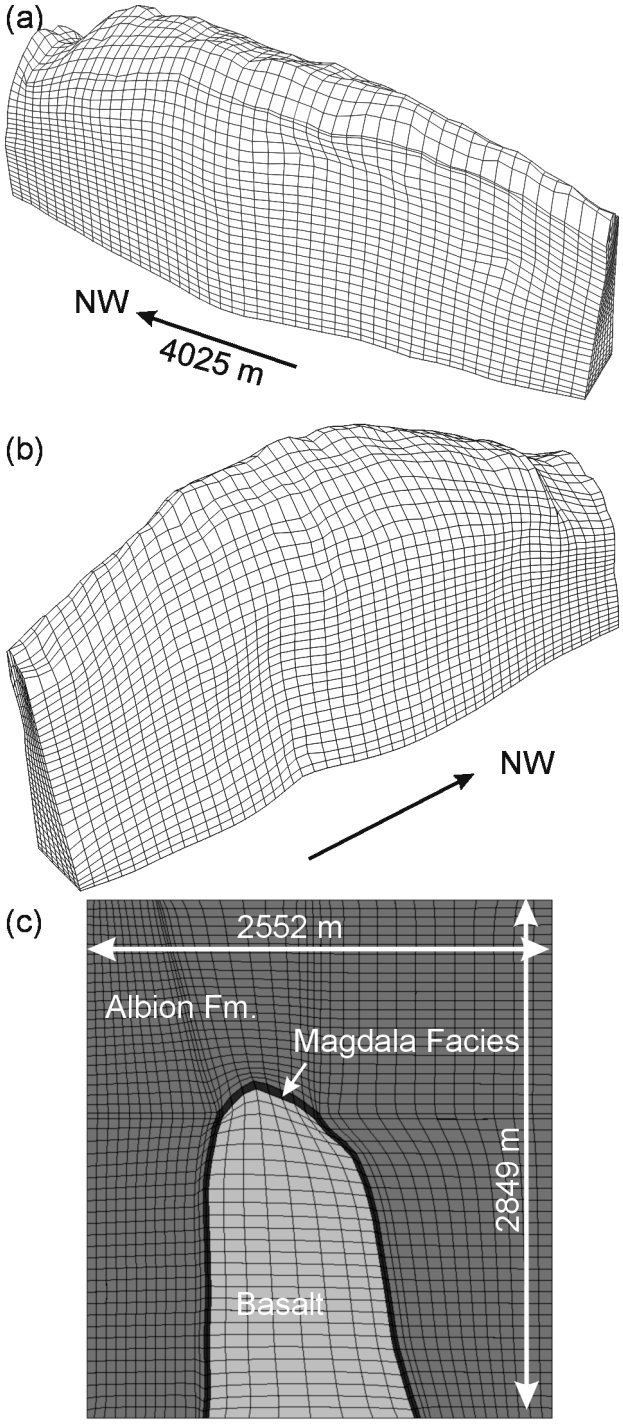

Figure 4a) Outline of basalt for the simplified model of the Magdala Dome. Dome has been constructed to simulate its shape prior to D_6 movement on the South Fault and does not contain any basalt lobes (i.e. Dukes Nose on the northwest flank). b) Cross-section through the centre of the Magdala Dome model.

The shape and geometry of the Magdala deposit models were defined by a combination of drilling, underground mapping and to a lesser extent geophysical interpretation. The Magdala Dome is modelled with two geometries: the first (Figure 4-4) takes into account the entire dome but is simplified and therefore does not

include basalt lobes such as the Dukes Nose or the Extended Basalt, while the second model (Figure 4-5) includes these lobes but only incorporates the northern half of the dome. The model of the entire dome strikes northwest and is 4025 m in this direction along the axis of the dome. The model is 2552 m wide and 2849 m tall.

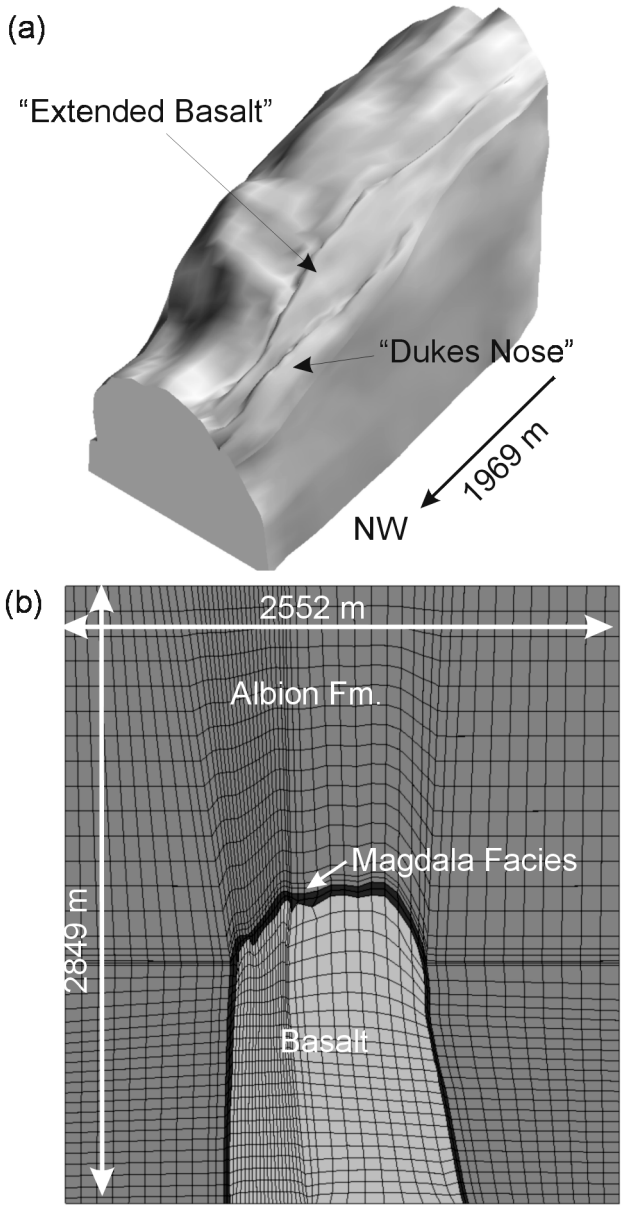

Figure 4-5a) Outline of basalt for the model of the Magdala Dome with basalt lobes. The model is of the northern half of the dome only and has been constructed to simulate its shape prior to D_6 movement on the South Fault. b) Cross-section through the centre of the Magdala dome with basalt lobes model.

The basalt dome is mantled by a thin unit of Magdala Facies which is ~ 25 m thick. The rest of the model consists of a matrix of "Albion Formation". The basalt unit has a maximum width and height of 1274 m and 1870 m, respectively. It is wider and plunges more steeply at the northern end, while the southern end is thin and has a sub-horizontal to shallow southerly plunge. In the model of the Magdala dome with basalt lobes which only takes into account the northern end of the dome, the basalt lobes occur on the west side and plunge to the north-northwest. The model extends 1969 m along the strike of the dome is 2552 m wide and 2849 m tall. The units are otherwise the same as the basalt which does not include the basalt lobes. In both models of the

Magdala Dome we are concerned with mineralisation and deformation that occurred prior to movement on the D_6 South Fault and therefore the displacement due to this fault has been removed in the models.

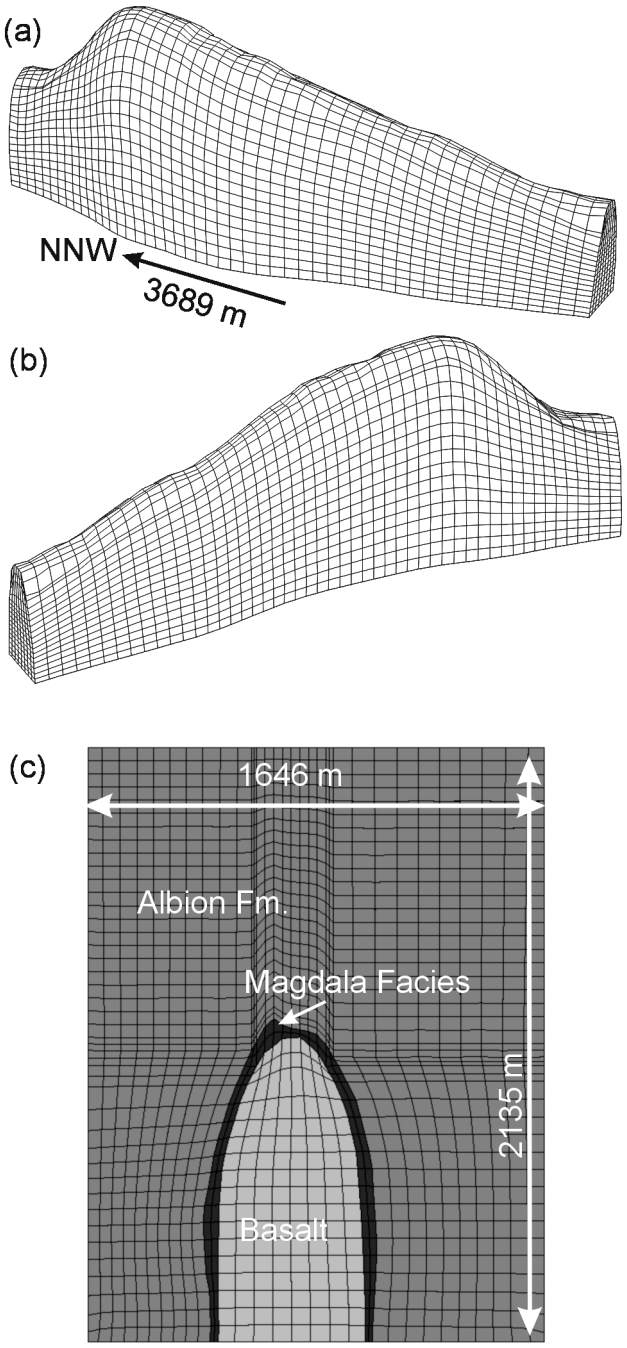

Figure 4-6 a) Outline of basalt for the simplified model of the Kewell Dome. The model does not contain any basalt lobes b) Cross-section through the centre of the Kewell Dome model.

Air core drilling, minor diamond drilling and detailed magnetic and gravity inversion modelling defined the Kewell and Wildwood model geometries. Both models were both built in gOCAD. For more information on the methods used to create the geometries of the models see Rawling *et al.* (this volume).

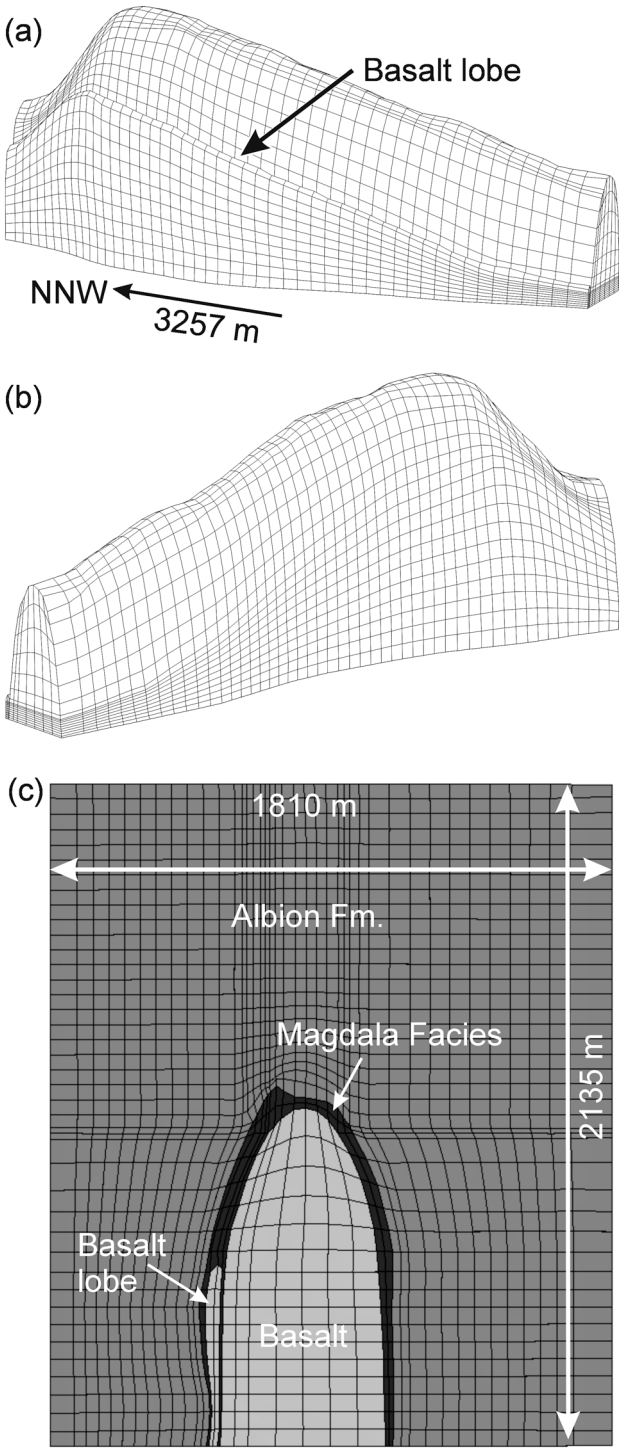

Figure 4-7 a) Outline of basalt for the the Kewell Dome with a basalt lobe. b) Cross-section through the centre of the Kewell Dome model.

The Kewell dome is also modelled with two geometries: with and without a basalt lobe. The basalt dome strikes to the north-northwest and the model without the basalt lobe extends 3689 m in this direction (Figure 4-6). It is 1646 m wide and 2135 m tall. The dome has a maximum width and height of 792 m and 1273 m, respectively. The basalt dome is doubly plunging with a steep northerly plunge and a longer more

shallowly southern plunge. The model of the Kewell Dome with a basalt lobe (Figure 4-7) has roughly the same dimensions: 3257 m long, 1810 m wide and 2135 m tall. The basalt lobe occurs on the west side and mimics the shape of the top of the dome with a steep northerly plunge and shallower southerly plunge. Part of the Kewell Dome has been eroded and therefore the shape of the highest portion of the model has been extrapolated and interpreted from geophysical information.

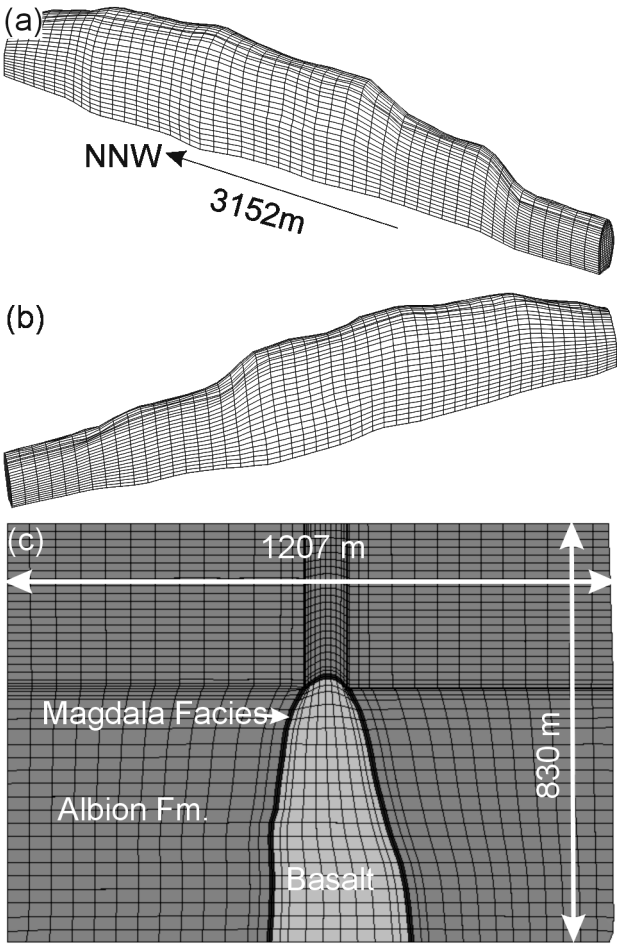

Figure 4-8 a) Outline of the the Wildwood Dome. The model does not contain any basalt lobes.

b) Cross-section through the centre of the Wildwood Dome model.

The Wildwood dome strikes to the north-northwest and the model (Figure 4-8) extends 3152 m in this direction. It is 1207 m wide and 830 m tall. The dome has width and height of 542 and 550 m, respectively and plunges shallowly both to the north and south.

Rock Properties and initial conditions

Three major rock types were considered to be critical to the modelling: the basalt (domes), Magdala Facies and the Albion Formation. The petrophysical data used for each rock type in the modelling was taken from geotechnical data supplied by Leviathan. Overall the basalt was assigned the strongest mechanical properties and lowest permeabilities and the Magdala Facies were assigned the lowest mechanical properties and the highest permeability (Table 4-1). Permeability remained constant during deformation. Stress conditions were initialised to simulate burial to 6 km depth, while pore pressure values were initialised to a pore fluid factor of 0.5 (half-way between hydro- and lithostatic).

	Basalt	Albion Fm.	Magdala Facies
Density (kg m^{-3})	2950	2760	2790
Bulk modulus (GPa)	67	45	61
Shear modulus (GPa)	45	20	22
Cohesion (MPa)	40	30	25
Tensile strength (MPa)	4	3	3
Friction angle (^{o})	30	25	20
Dilation angle (^{o})	2	3	4
Permeability (m^2)	1×10^{-16}	1×10^{-15}	5×10^{-12}

Table 4-1. Specific rock properties used in the models.

Numerical modelling results

In the following sections we present the results of the numerical models. Specifically we discuss the relative position and magnitude of regions of accumulated positive volume strain (dilation), and high instantaneous fluid-flow rates which are interpreted to be the deformation – fluid-flow factors with the greatest potential influence on the localisation of gold mineralisation. Volume strain is measured as the cumulative ratio: (V'-V)/V, where V is the original volume and V' is the new volume. Instantaneous Darcy fluid velocities are measured in m/s. The premise here is that areas with high values of dilation and fluid flow will have a greater volume of potentially gold-bearing fluid pass through. There is no chemical component to these models and therefore whether gold would actually precipitate is another matter.

Dukes Nose

Volume strain

In all models the greatest amount of dilation (positive volume strain) occurs in two areas: above the crest of the basalt lobe (Dukes Nose) and within the Magdala Facies at the bump where the Extended Basalt should occur (Figure 4-9a-e). Areas of high positive volume strain within the Magdala Facies at the top of the model are a boundary effect. The greatest amount of dilation is recorded in the east-northeast – west-southwest shortened model (Figure 4-9a) and gradually decreases in models

where the shortening direction is rotated away from this direction. The position of maximum dilation; however, does not change and in all models, areas of maximum dilation occur within the Magdala Facies unit on the flank of the Dukes Nose (closest to the Albion Formation) and coincide with a thickening of the Magdala Facies unit.

Fluid-flow velocities

The highest fluid velocities occur within the Magdala Facies which is assigned the highest permeability. Within this unit the highest velocities occur: 1) above the crest of the Dukes Nose where the Magdala Facies are thinnest; 2) within the trough of Magdala Facies to the east of this crest and 3) and where the top of the Extended Basalt should occur (Figure 4-9f-j). The region of Magdala Facies which occurs between the crest Dukes Nose and the flank of the Extended Basalt is referred to as a 'Waterloo' (Watchorn & Wilson 1989). In the northeast-southwest shortened model maximum fluid flow rates occur at the behind the "bump" of the Dukes Nose within the intervening Magdala Facies and also slightly up plunge and down the flank of the Dukes Nose (Figure 4-9f). As with dilation, the areas of highest fluid-flow rate occur in the model with east-northeast – west-southwest directed shortening and their position is the same as the northeast-southwest shortened model (Figure 4-9g). As the shortening direction is rotated clockwise to east-west, east-southeast - west-northwest and southeast – northwest (Figure 4-9h-j), the maximum fluid rates are reduced and their position moves down plunge but are still located within the Magdala Facies which occurs between the Dukes Nose and the flank of the Extended Basalt.

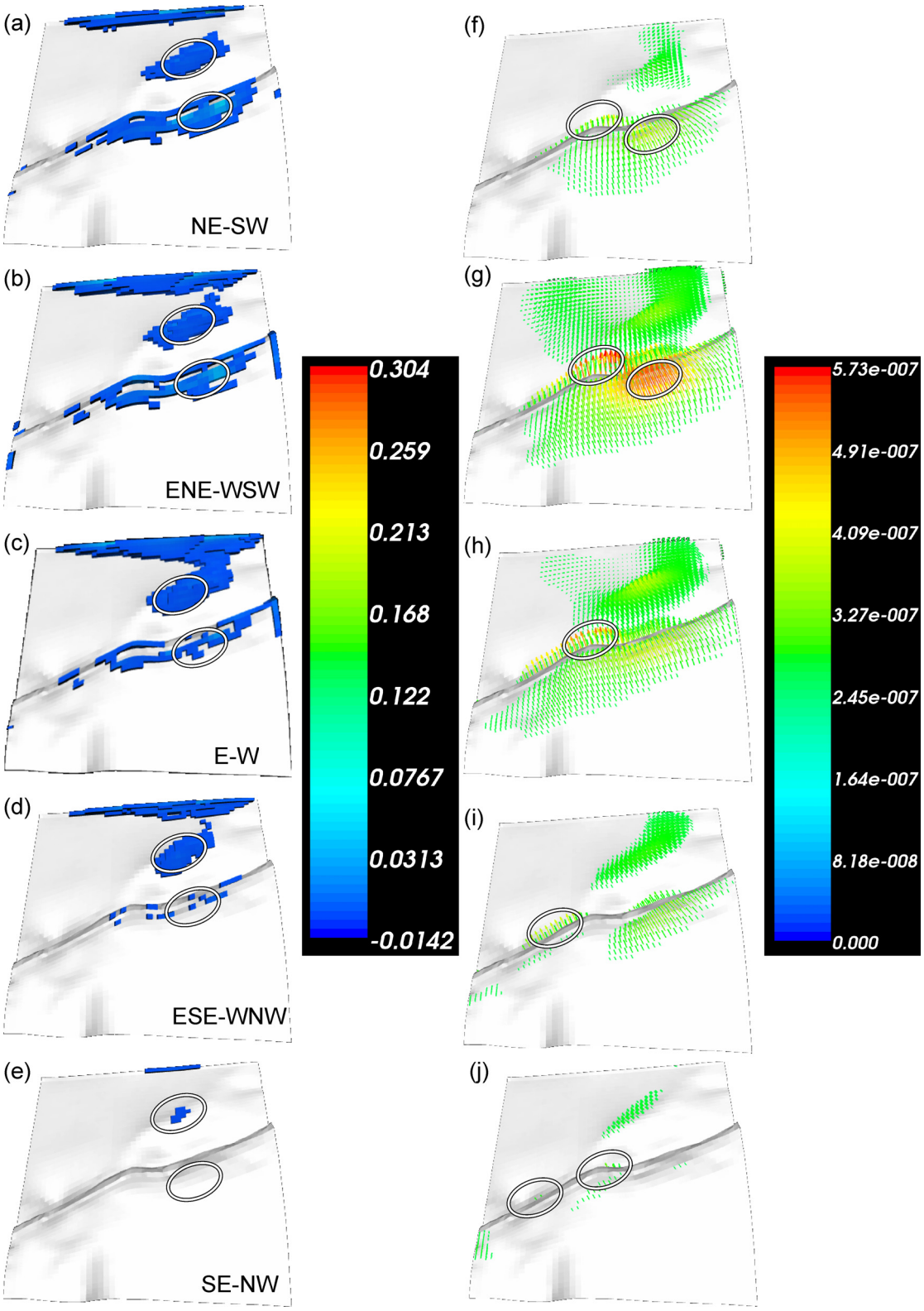

Figure 4-9 Results from Dukes Nose models after 5 % shortening. a-e) Accumulated volume strain with only values above 0.00778 shown. Negative values indicate contraction while positive values indicate dilation. f-j) Instantaneous fluid-flow velocities above 5e-8 m/s (0.16 m/yr). Ovals indicate maximum location of areas of maximum dilation and fluid flow velocity.

Magdala Dome without a basalt lobe

This model takes into account the entire Magdala Dome prior to D_6 movement on the South Fault. It has been simplified somewhat and does not include any basalt lobes such as the Dukes Nose.

Volume strain

The greatest amount of dilation occurs within the Magdala Facies on the top portion of the dome. In the northeast - southwest shortened model (Figure 4-10a) the region of maximum dilation occurs on the northeast side of the crest of the dome which has a shallow dip, while a region of lower dilation occurs on the southwest side of the crest of the dome. The region of maximum dilation occurs in a similar position in the east-northeast – west-southwest shortened model (Figure 4-10b); however, the extent of significant dilation is larger. The east - west shortened model (Figure 4-10c) results in the highest values of dilation and at this orientation of shortening the maximum values occur on the northwest flank of the dome near where the Dukes Nose occurs. The size of the region of significant dilation is less than that of the east-northeast – west-southwest shortened model. In the east-southeast – west-northwest shortened model (Figure 4-10d) maximum dilation also occurs on the northwest flank; however, dilation on the top of the dome separating the northwest and southeast flanks has decreased. The southeast - northwest shortened model (Figure 4-10e) results in maximum dilation values closer to the crest of the dome at the northwest end of the dome, while dilation on the southeast flank is significantly reduced. In most cases tensile failure occurs at the same location as the regions of maximum dilation at the top of the dome.

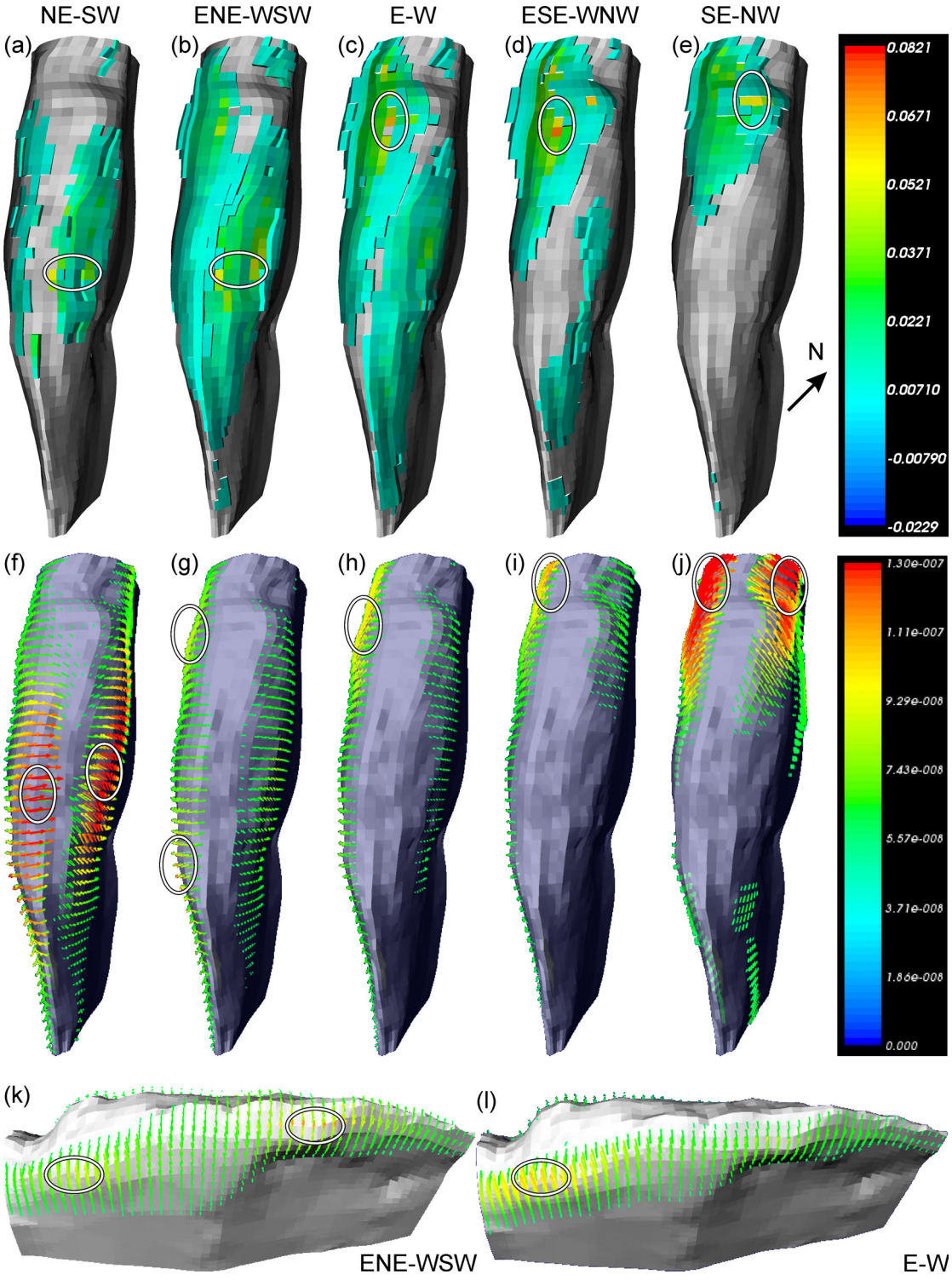

Figure 4-10. Results from Magdala Dome models after 5 % shortening. a) Accumulated volume strain with only values above 0.0075 shown. Negative values indicate contraction while positive values indicate dilation. b) Instantaneous fluid-flow velocities above 5e-8 m/s (0.16 m/yr).

Fluid-flow velocities

Overall fluid-flow is directed up the flanks of the dome and perpendicular to the long axis of the dome. Maximum values occur on the top of the flanks of the dome where the dip of the basalt changes from sub-vertical to relatively shallow. On the very top of the dome where fluid-flow velocities are generally lower, flow is directed up plunge and parallel to the long axis of the dome. Changes in instantaneous fluid-flow patterns with varying shortening directions are similar to those displayed by changes in volume strain. Unlike dilation; however, the maximum fluid-flow velocities occur in the northeast - southwest shortened model (Figure 4-10f) on both flanks close to the top and centre portions of the dome. When the shortening direction is rotated to the east-northeast – west-southwest (Figure 4-10g, k), maximum values shift to the west side of the dome to positions which coincide with the position of the Dukes Nose as well the Golden Gift; two areas of significant mineralisation. During east - west directed shortening (Figure 4-10h and l) maximum values also occur in the region of the Dukes Nose and the area over which high values occurs is increased; however, fluid flow rates in the area of the Golden Gift are reduced. East-southeast – west-southwest shortening (Figure 4-10i) results in a shift of the maximum values to the end of the northwest side of the dome. Southeast - northwest shortening (Figure 4-10j, perpendicular to the long axis of the dome) results in high fluid-flow rates on both sides of the dome at the northwest end.

Magdala Dome with a basalt lobe

Volume strain

Overall volume strain patterns in this suite of models (Figure 4-11a-e) are consistent with the model of the entire dome which excludes the basalt lobes. The significant difference is that areas of dilation are strongly concentrated into 'Waterloos' associated with the Dukes Nose and Extended Basalt lobes. Apart from the northeast - southwest shortened model (Figure 4-11a), maximum values in all models occur in this area and move down plunge as the shortening direction is rotated from east-northeast – west-southwest to southeast - northwest.

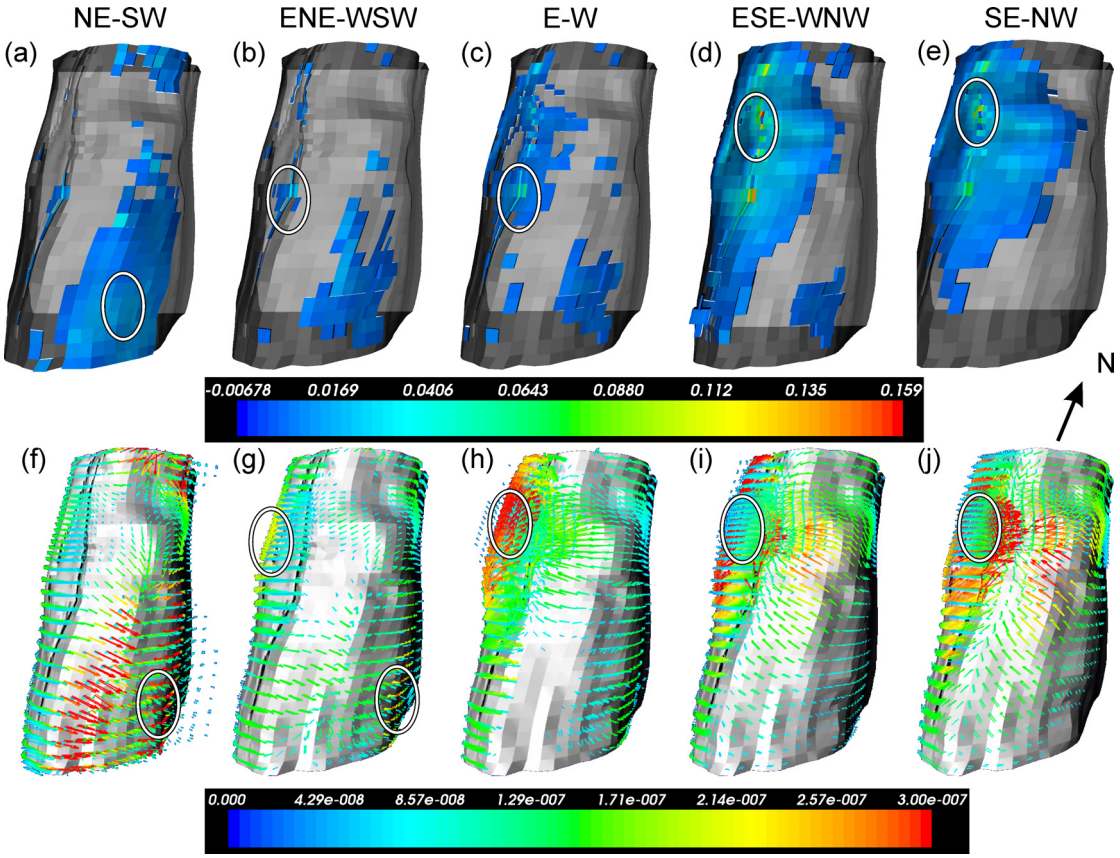

Figure 4-11. Results from Magdala Dome with basalt lobes models after 5 % shortening. a) Accumulated volume strain with only values above 0.005 shown. Negative values indicate contraction while positive values indicate dilation. b) Instantaneous fluid-flow velocities above 5e-8 m/s (0.16 m/yr).

Fluid-flow

As with volume strain, fluid-flow patterns are consistent with the model of the entire Magdala Dome which excludes the basalt lobes. Maximum values are recorded in the east-southeast – west-northwest shortened model (Figure 4-11g). With northeast - southwest directed shortening (Figure 4-11f) maximum values are recorded on the southeast flank of the model. When the shortening direction is rotated to east-northeast – west-southwest (Figure 4-11g) maximum values are associated with the region above the Dukes Nose as well as the southeast flank. During east - west, east-southeast – west-northwest and southeast - northwest shortening (Figure 4-11h, i and j), maximum values only occur in a region above the Dukes Nose.

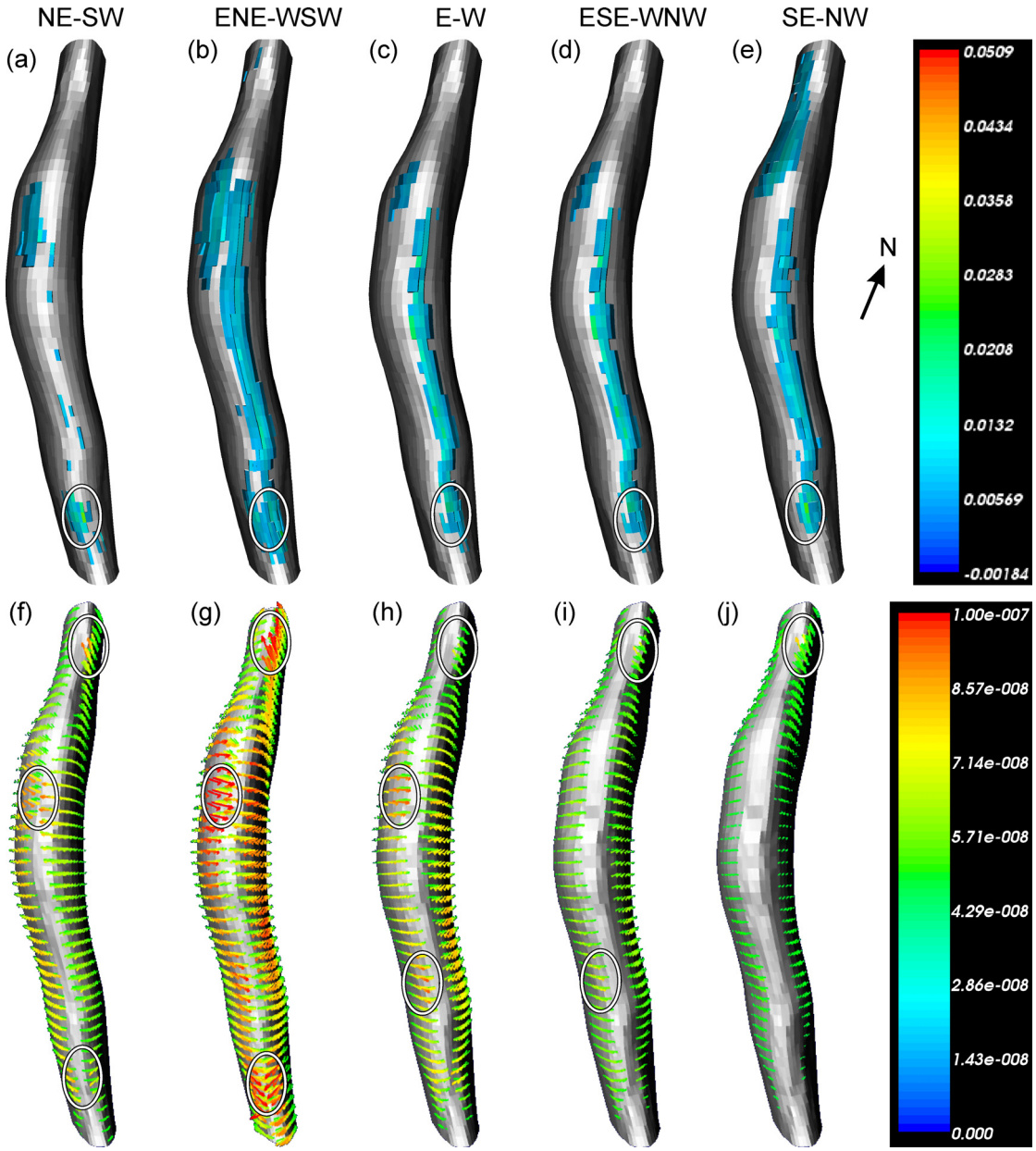

Figure 4-12. Results from Kewell Dome models after 5 % shortening. a) Accumulated volume strain with only values above 0.01 shown. Negative values indicate contraction while positive values indicate dilation. b) Instantaneous fluid-flow velocities above 5e-8 m/s (0.16 m/yr). Outline of basalt for the model of the Kewell Dome with a basalt lobe. b) Cross-section through the centre of the model of the Kewell Dome with a basalt lobe.

Kewell Dome without basalt lobe

Volume strain

The Kewell Dome has a distinctly different shape to the Magdala Dome and therefore the positions of areas of maximum dilation are also different. The area of maximum dilation occurs on the crest of the dome at the southern end in all the Kewell models (Figure 4-12a-e), where there is a change to a more shallowly plunge. Significant dilation also occurs on the entire south plunging portion of the dome at its crest. As the shortening direction is rotated from northeast - southwest to southeast - northwest

an area of significant dilation that occurs on the northwest flank of the dome is shifted northwards.

Fluid-flow

As in the Magdala Dome models, areas of maximum fluid-flow occur at the top of the flanks of the dome where the dip of the basalt changes from sub-vertical to sub-horizontal; just below areas of significant dilation. The positions of areas of maximum fluid-flow also vary with changes in shortening direction. With northeast - southwest shortening (Figure 4-11f) areas of maximum fluid-flow occur on the: i) southwest side of the dome at the southern end, ii) on the west side just below the highest point of the dome and iii) on the northeast flank. During east-northeast – west-southwest shortening (Figure 4-11g) maximum flow rates also occur in these areas; however, the magnitude is increased. During east-west shortening (Figure 4-11h) the area of maximum flow on the southern end has moved up plunge and flow rates at the northern end are reduced. During east-southeast - west-northwest (Figure 4-11i) shortening rates are reduced on the west side below the top of the dome. With southeast-northwest shortening (Figure 4-11j) maximum values occur on the northeast side of the dome and all areas are reduced.

Kewell Dome with basalt lobe

Volume strain

Volume strain patterns in the Kewell models with a basalt lobe (Figure 4-13a-e) are very similar to those in the model without the lobe. Maximum values occur at the crest of the southern end of the dome with all shortening directions. Significant values also occur up plunge from this position towards the very top of the dome. As the shortening direction is rotated towards southeast - northwest an area of dilation also occurs on the northwest flank.

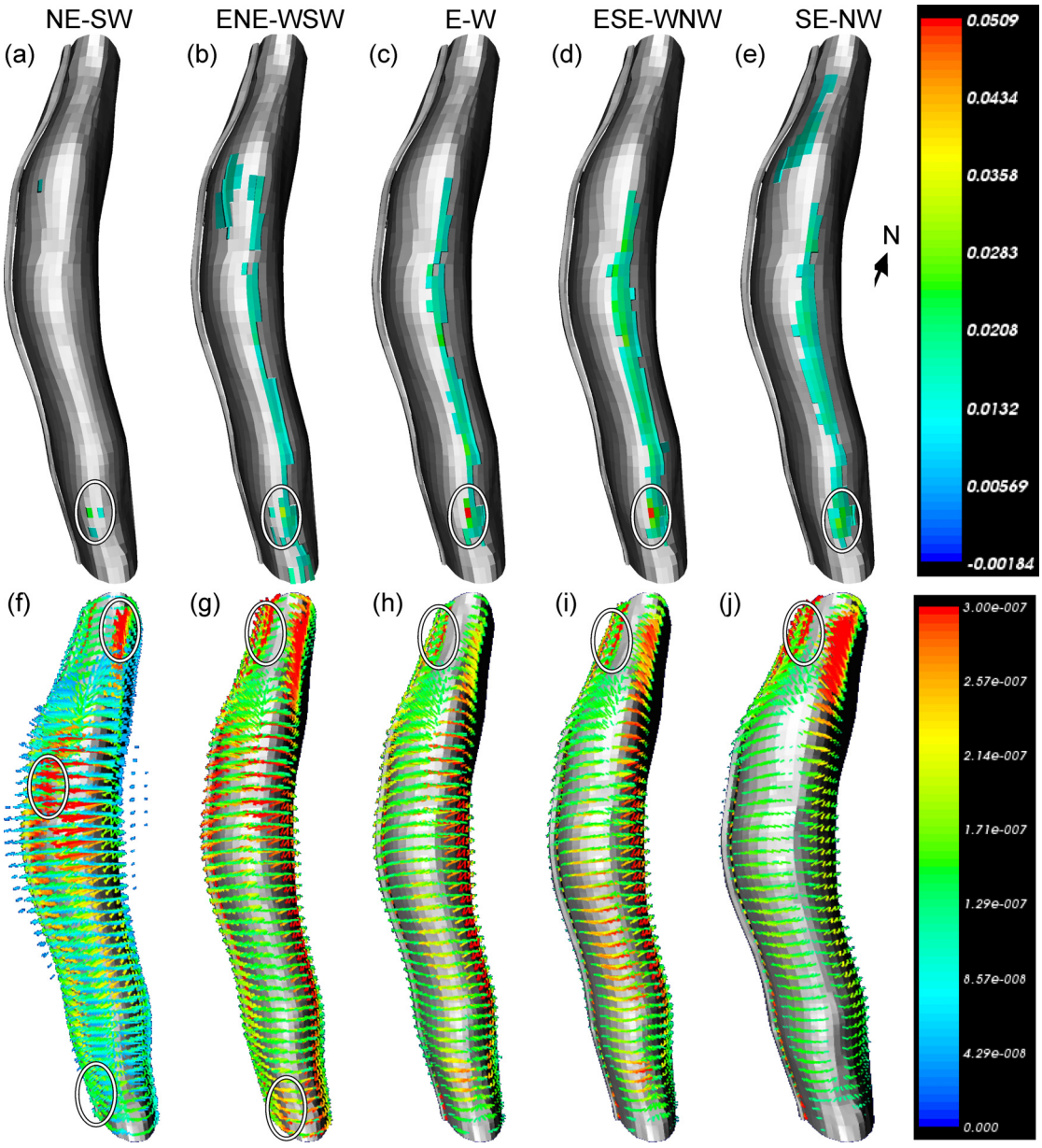

Figure 4-13. Results from the models of the Kewell Dome with a basalt lobe after 5 % shortening. a) Accumulated volume strain with only values above 0.01 shown. Negative values indicate contraction while positive values indicate dilation. b) Instantaneous fluid-flow velocities above 5e-8 m/s (0.16 m/yr).

Fluid-flow

Fluid-flow patterns in the Kewell model with a basalt lobe (Figure 4-13f-j) are slightly different to the model without the lobe. The Magdala Facies which occurs between the lobe and the main basalt dome focuses fluid-flow and therefore maximum values occur adjacent to the basalt lobe at the northern end in all models where the crest of the lobe is closest to the top of the main dome. In the northeast - southwest shortened model (Figure 4-13f) high flow rates also occur on the west side below the highest portion of the dome. With east-northeast – west-southwest shortening (Figure 4-13g) high fluid-flow rates also occur in this position but near the lobe at the very southern end of the dome as well. In the east – west, east-southeast – west-northwest and southeast – northwest shortened models (Figure 4-13h, i and j), maximum fluid flow

values occur only at the northern end of the dome where the crest of lobe is close to the top of the main dome.

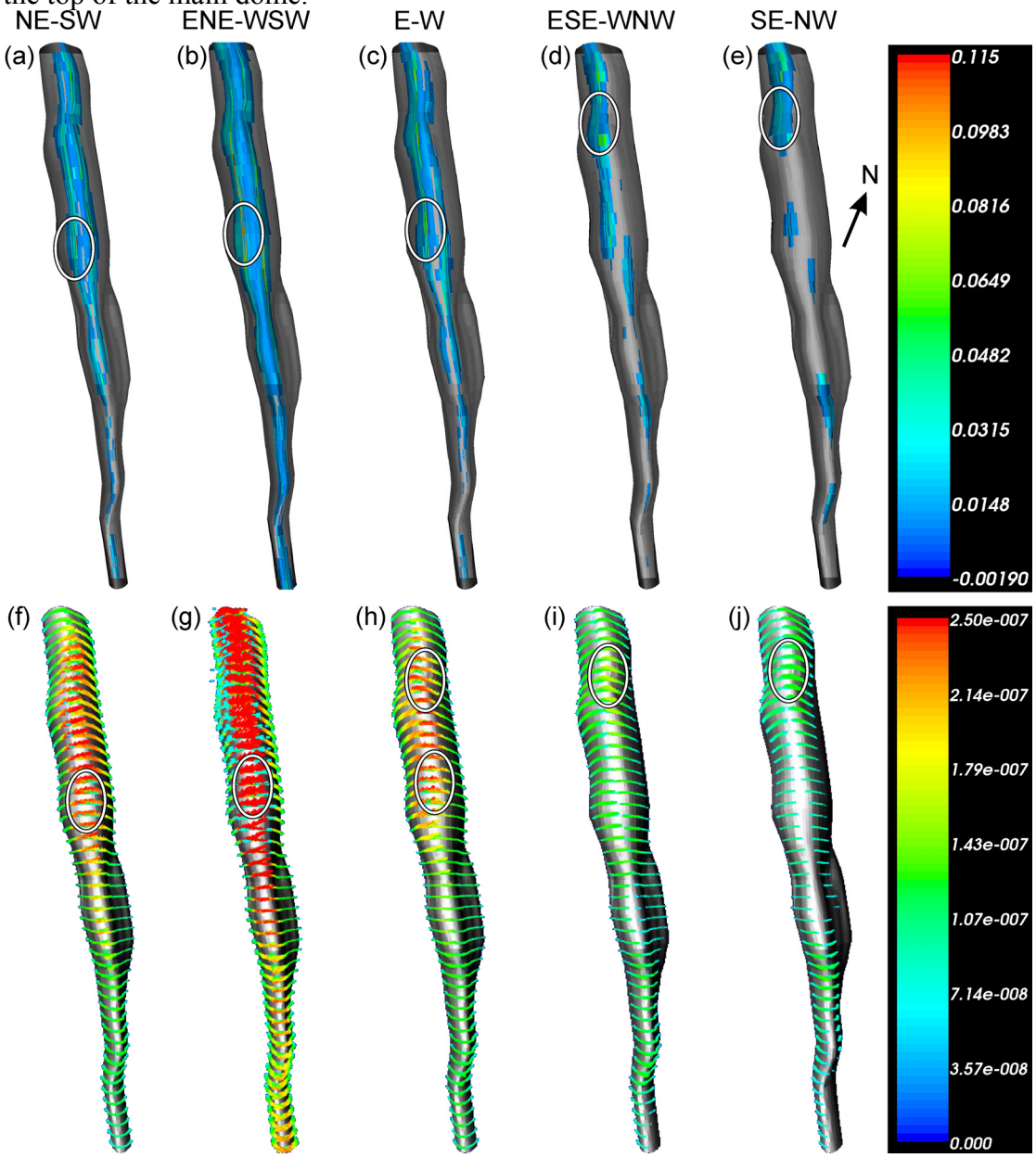

Figure 4-14. Results from Wildwood models after 5 % shortening. a) Accumulated volume strain with only values above 0.01 shown. Negative values indicate contraction while positive values indicate dilation. b) Instantaneous fluid-flow velocities above 5e-8 m/s (0.16 m/yr).

Wildwood Dome

Volume strain

As with the Kewell models areas of high positive volume strain occur on the top of the dome. During northeast - southwest, east-northeast – west-southwest and east - west shortening (Figure 4-14a, b and c) the area of maximum dilation occurs at the highest structural position on the west side of the dome. With east-southeast – west-northwest and southeast-northwest shortening (Figure 4-14d and e) the area of maximum dilation moves down plunge and to the north. The model with east-

northeast – west-southwest (Figure 4-14b) shortening exhibits the largest area of significant dilation; along most of the top of the dome. As the shortening direction is rotated towards the southeast-northwest, dilation becomes gradually reduced at the southern and middle portions of the dome.

Fluid-flow

The locations of areas of maximum fluid flow are comparable to those of dilation. During northeast – southwest, east-northeast – west-southwest and east – west shortening (Figure 4-14f, g and h), maximum fluid-flow rates occur close to the highest structural position of the dome. Fluid-flow rates are greatest during east-northeast – west-southwest shortening (Figure 4-14b). With east-west shortening high flow values begin to move down plunge and northwards. During east-southeast – west-northwest and southeast – northwest shortening (Figure 4-14i and j) maximum flow rates occur at the north end of the dome and values are significantly less than in models with different shortening directions.

Discussion and Implications for exploration

The models show that both the presence of basalt lobes and changing the shortening direction cause significant changes in the position of areas of dilation and high fluid flow rates. In models that do not contain basalt lobes areas of maximum dilation generally occur on the top of the dome whereas regions of high fluid flow rate occur at the top of the flanks of the dome where there is a change in dip. The presence of a basalt lobe, strongly localises high fluid flow rates into the adjacent 'Waterloo', but does not greatly control the location of maximum dilation. In all models the position and magnitude of areas of positive volume strain (dilation) and instantaneous fluid flow velocities change with shortening direction. Overall the patterns of dilation and fluid flow velocities are consistent across the different models and where there are differences these may be explained by the differences in shape of the basalt bodies.

In all models areas of high fluid-flow rate occur within the Magdala Facies because of the high permeability assigned to it but within this unit high fluid-flow is controlled by the proximity of areas of contraction and dilation. Areas of contraction on the flanks of the basalt dome occur where the dip is steep and therefore at a high angle to the shortening direction. Towards the top of the domes, the Magdala Facies has a shallow dip and is an area of dilation. This causes fluid-flow rates to be highest close to the top of the flanks of the dome where areas of contraction and dilation are close together and both volume strain and pore pressure gradients are highest. Areas of dilation and high fluid flow rates are generally in the same location; however, there is always a slight offset. Fluid flow rates are highest close to but not coincident with areas of maximum dilation because fluid is flowing *towards* these areas within the high fluid pressure gradient. The fluid pressure gradient is significantly reduced at the site of maximum dilation.

In the Dukes Nose models and the Magdala and Kewell models which incorporate a basalt lobe, areas of high fluid-flow are concentrated close to the basalt lobes. In particular the highest fluid flow rates occur within the trough of Magdala Facies (at the 'Waterloo') that separates the basalt lobe from the main basalt body. This occurs because the Magdala Facies separating the basalt bodies is contracting and a high

fluid pressure gradient is produced between the Magdala Facies in the 'Waterloo' and that which lies above. Fluid is forced up out of the Magdala Facies rocks in the Waterloo which are contracting towards those above which are dilating. Areas of maximum dilation; however, still occur near the top of the main basalt dome. In the Kewell model with a basalt lobe, the plunge of the lobe mimics that of the main dome for most of the model. The top of the lobe is at a significant distance from the top of the main dome except at the very northern end of the dome. This causes fluid flow rates to be elevated at this position relative to other portions of the basalt lobe.

In the Dukes Nose models, areas of high fluid flow are recorded on the flank of the Dukes Nose where the Magdala Facies is quite thin. An area close to where the top of the Extended Basalt should occur is also an area of high but reduced fluid flow. In the Magdala Dome models areas of high fluid flow are associated with the Basalt Lobes whereas maximum dilation and tensile failure occur at the top of the dome. The difference in the position of these two properties is consistent with the location of different styles of mineralisation around the dome. Mineralisation within the Central Lode near the Dukes Nose on the flanks of the dome is reasonably disseminated and is likely to have formed as a result of fluid permeating the area. Mineralisation on the top of the dome is associated more with veins and is more likely to have formed as a result of tensile failure.

Miller & Wilson (2002) interpreted gold mineralisation to have been synchronous with east-northeast – west-northwest to east-west shortening with the peak at east-west. In the both the Dukes Nose and Magdala Dome models the position of areas of maximum fluid flow rates and values of dilation are consistent with this interpretation and with the location of known mineralisation. In the Magdala Dome models without a basalt lobe, areas of high fluid flow in the area of the known mineralisation at the Dukes Nose are recorded in the east-northeast – west-northwest and east-west shortened models. Models with different shortening rates have significantly reduced fluid flow rates in this area and the maximum fluid flow rates occur in different locations. High fluid flow rates at the approximate position of the Golden Gift Lodes are also recorded in the east-northeast – west-northwest model. Similar results are recorded in the Magdala Dome models with a basalt lobe; the highest fluid flow rates in the region of the Dukes Nose are recorded during east-west shortening. Although the presence of a basalt lobe strongly focuses high fluid flow rates into areas of the basalt lobe, a change in shortening direction alters the position of maximum fluid flow rates along the plunge of the lobe. In the Dukes Nose models maximum fluid flow rates at the position of the main Central Lode mineralisation are recorded during east-northeast – west-northwest shortening. With different shortening directions maximum fluid flow rates are reduced and move down plunge from the area of known mineralisation. The fact that areas of high fluid flow rates (and dilation to a lesser extent) are consistent with areas of known mineralisation in the Dukes Nose and Magdala Dome models which are shortened in east-northeast – west-northwest and east-west directions shows us that these parameters may be used to explain in part the location of gold mineralisation.

At the Kewell and Wildwood Domes the general shape of the domes is known from geophysical and drilling data but the position or even presence of gold mineralisation was not known until recently. At the Kewell Dome, shallow air-core drilling had identified a number of gold anomalies, while deeper diamond drilling on the west

flank of the dome recorded some mineralisation where it intersected a basalt lobe and no mineralisation at depths below the lobe. The information from the Dukes Nose and Magdala Dome numerical models was then used to help predict where gold mineralisation might occur at the Kewell Dome. The position of an area of high fluid flow rate and significant dilation recorded in the east-west shortened model, coincident with a gold anomaly (from the air-core drilling data) indicated that a position on the south end of the dome on the west flank had potential for mineralisation. Other areas in the model have high fluid flow rates but they include areas at the very top of the dome that has been eroded. The area at the south end of the dome is the only position where high fluid flow rates and considerable dilation coincide together with a gold anomaly and the potential presence of a basalt lobe (from the diamond drilling). This area was targeted by Leviathan Resources and resulted in significant gold values within the drill-core. An area at the northern end of the dome where high fluid flow rates adjacent to the basalt lobe coincides with air-core drilling gold anomalies has not been tested.

Conclusions

- Numerical modelling has placed some constraint on the importance of basalt dome shape and interpreted syn-mineralising shortening direction in controlling the location of gold mineralisation around basalt domes in the Stawell Corridor, Western Victoria.
- In dome scale models which do not contain basalt lobes (Magdala, Kewell, and Wildwood) areas with the maximum fluid flow rates occur on tops of the flanks of the domes where there is a dramatic change in dip of the basalt. At this position a change from negative volume strain (contraction) on the flanks of the dome to positive volume strain (dilation) at the top of the dome causes a significant pore pressure gradient to form and results in increased fluid flow rates relative to other areas of the domes.
- In models which contain basalt lobes (Dukes Nose, Magdala, Kewell) the location of high fluid flow rates are strongly controlled by the presence of these lobes. High fluid pressure gradients are created between the contracting Magdala Facies within the 'Waterloo' adjacent to the lobes and areas dilating above.
- Areas of significant dilation occur on the shallow dipping portion at the top of the dome and cause fluid to flow towards them. Areas which have significant dilation are also areas of tensile failure in some cases and are coincident with areas of known quartz vein associated mineralisation.
- In the Dukes Nose and Magdala Dome models only the east-northeast – west-northwest and east-west shortened models record high fluid flow rates in areas of known mineralisation – the Dukes Nose and Golden Gift. This is consistent with the interpreted syn-mineralisation shortening directions of Miller (2002). Therefore in this situation fluid flow rates during east-northeast – west-northwest and east-west shortening can be used to indicate the potential location of gold mineralisation.
- The position of areas of high fluid flow rate in the Kewell Dome numerical models shortened in the east-northeast – west-northwest and east-west direction, combined with information from limited drilling indicated the potential for gold mineralisation at the south-west end of the dome. Diamond drill holes in this area yielded significant gold values.

- The combination of a good geological understanding of the Stawell mineralising system, combined with numerical modelling helped predict the location of and reduce the number of drill holes required to find gold mineralisation at the Kewell Dome.

References

BEAR, J. & VERRUIJT A. 1987. Modelling Groundwater Flow and Pollution, D. Reidel Publishing Company, Boston.

DESAI C.S. & CHRISTIAN J.T. 1977. Numerical Methods in Geomechanics. McGraw-Hill, New York.

DUGDALE A.L. & WILSON, C.J.L.. 2005 Hydrothermal alteration of an atypical turbidite-hosted orogenic gold deposit: the Magdala system, Stawell, western Victoria, Australia *Australian Journal of Earth Sciences,* submitted.

FREDERICKSEN D.C. & GANE M. 1998. Stawell Gold Deposit, *in* Berkman, D.A., and Mackenzie, D.H., eds., Geology of Australian and Papua New Guinean Mineral Deposits. The Australian Institute of Mining and Metallurgy, Melbourne, p. 535-542.

GANE M.J. 1998. Gold mineralisation within the basalt contact ore zones, Magdala mine, Stawell, Victoria. M.Sc. thesis, University of Melbourne, Melbourne, Australia (unpubl.), 302p.

GRAY D.R. 1988. Chapter 1: Structure and Tectonics. *In:* Douglas J. & Ferguson J. eds. *Geology of Victoria*, pp. 7-18. Victorian Division of the Geological Society of Australia.

HENRY D.A, SQUIRE R.J, WILSON C.J.L & RAWLING T.J. 2005. Controls on the 440 Ma high-grade Hangingwall Reef gold deposit, Stawell, western Victoria. *Australian Journal of Earth Sciences,* **this volume.**

LEADER L. D., RAWLING T.J. & WILSON C.J.L. 2005. Modelling of structural transect across the St Arnaud Group, Victoria. *Australian Journal of Earth Sciences,* submitted**.**

MAPANI B.S.E. & WILSON C.J.L. 1995. Structural evolution and gold mineralisation in the Scotchmans Fault Zone, Magdala Gold Mine, Stawell, Western Victoria, Australia. *Economic Geology* **89,** 566–583.

MAPANI B.S.E. & WILSON C.J.L. 1998. Evidence for externally derived vein forming and mineralising fluids: an example from the Magdala gold mine, Stawell, Victoria, Australia. *Ore Geology Reviews* **13,** 323-343.

MILLER J. MCL, DUGDALE L.J. & WILSON C.J.L. 2001. Variable hangingwall palaeotransport during Silurian and Devonian thrusting in the Western Lachlan Fold Belt; missing gold lodes, synchronous Melbourne trough sedimentation and Grampians Group fold interference. *Australian Journal of Earth Sciences* **48**, 901-909.

MILLER J. MCL, & WILSON C.J.L. 2002. The Magdala Lode System, Stawell, southeastern Australia; structural style and relationship to gold mineralization across the Western Lachlan Fold Belt. *Economic Geology and the Bulletin of the Society of Economic Geologists* **97**, 325-349.

MILLER J. MCL. & WILSON C.J.L. 2004a. Application of structural analysis to faults associated with a heterogeneous stress history: the reconstruction of a dismembered gold deposit, Stawell, western Lachlan Fold Belt, southeastern Australia, *Journal of Structural Geology*.**26**, 1231-1256

MILLER J. MCL. & WILSON C.J.L. 2004b. Stress controls on intrusion-related gold lodes: Wonga gold mine, Stawell, Western Lachlan Fold Belt, southeastern Australia. *Economic Geology **99**, 941-963.*.

MILLER J. MCL., WILSON C.J.L. & DUGDALE, L.J. 2005. Ordovician to Early Devonian structural evolution of the western Victorian gold deposits. *Australian Journal of Earth Sciences,* submitted**.**

MILLER J. MCL., PHILLIPS D., WILSON C.J.L. & DUGDALE L.J. in press. Evolution of a reworked orogenic zone: the boundary between the Delamerian and Lachlan Fold Belts, southeastern Australia. *Australian Journal of Earth Sciences.*

ORD A. & OLIVER N.H.S. 1997. Mechanical controls on fluid-flow during regional metamorphism: some numerical models. *Journal of Metamorphic Geology* **15,** 345-359.

ORD A., HOBBS B.E., ZHANG Y., BROADBENT G.C., BROWN M., WILLETTS G., SORJONEN-WARD P., WALSHE JL., & ZHAO C. 2002. Geodynamic modelling of the Century deposit, Mt Isa Province, Queensland. *Australian Journal of Earth Sciences* **49,** 1011-1039.

RAWLING T.J., SCHAUBS P.M., DUGDALE L.J. & WILSON C.J.L. 2005 Development of new mineral targeting strategies using 3-D modelling and numerical fluid simulation techniques in western Victoria. *Australian Journal of Earth Sciences* **this volume.**

ROBINSON, J., WILSON, C.J.L. & RAWLING, T.J. Numerical modelling of an evolving gold system: Structural and lithological, controls on ore shoot formation within the Magdala Mine, western Victoria*, Australian Journal of Earth Sciences,* submitted.

SCHAUBS P.M., & ZHAO C. 2002. Numerical models of gold deposit formation in the Bendigo-Ballarat Zone, Victoria, Australia, *Australian Journal of Earth Sciences*.**49** 1077-1096.

SORJONEN-WARD P., ZHANG Y. & ZHAO C. 2002. Numerical modelling of orogenic processes and gold mineralisation in the southeastern part of the Yilgarn Craton, Western Australia. *Australian Journal of Earth Sciences* **49,** 935-964.

SQUIRE R & WILSON C.J.L. in press. Interaction between collisional orogenesis and convergent-margin processes: evolution of the Cambrian proto-Pacific margin of East Gondwana. *Journal of the Geological Society*

VANDENBERG A.H.M., WILLMAN C.E., MAHER S., SIMONS B.A., CAYLEY R.A., TAYLOR D.H., MORAND V.J., MOORE D.H., & RADOJKOVIC A. 2000. The Tasman Fold Belt System in Victoria. Geological Survey of Victoria Publication. Melbourne, 462. pp.

WATCHORN R.B. & WILSON C.J.L. 1989. Structural setting of the gold mineralisation at Stawell, Victoria, Australia. *Economic Geology* **Monograph 6,** 292-309.

WILSON C.J.L., XU G. & MONCRIEFF J. 1999. The structural setting and contact metamorphism of the Wonga gold deposit, Victoria, Australia. Economic *Geology* **94**, 1305-1328.

Chapter 5 : 3-D Structural framework of western Victoria and implications for targeting gold mineralisation.

F. C. Murphy, T. J. Rawling, C. J. L. Wilson, L. J. Dugdale, & J. McL. Miller.

Summary

A crustal-scale 3-D model has been constructed of an area of 150 x 150 km to ~20 km depth in western Victoria through integrated analysis of a range of geological and geophysical data sets. The positions of major faults, intrusive bodies and lithostratigraphic packages are derived from interpretation of upward continued multiscale wavelet edges (worms) of aeromagnetic and gravity data, inversions of the gravity field and acoustic boundaries. We interpret the upper crustal structure as dominated by a series of northwest-trending steep to moderate inclined mainly east-dipping faults (e.g. Moyston, Pleasant Creek) that flatten at depth and sole onto a basal detachment. This detachment, termed the Western Fault, separates the upper crustal Cambrian elements from middle to lower crustal elements of inferred Proterozoic age. We suggest the controls on orogenic gold distribution may be related to the position of the leading edge of the Proterozoic wedge in the middle crust. The Coongee Fault, a key element in the mineralised Stawell corridor, appears to be a locus for basaltic domes that host the early stage Magdala-type deposits. This steep west-dipping fault is a distinct feature in termed of its dip direction, compared to the major east-dipping faults that dominate the upper crustal architecture. It represents a back thrust with superimposed sinistral transpression, and is interpreted as originating as a back-stop above a middle crustal ramp.

Introduction

In western Victoria, the exposed margin of the Palaeozoic Lachlan orogen is defined by interleaved geological elements showing strong metamorphic gradients and multiphase structural histories. The setting is complex as the area is co-located with the eastern extent of the Neoproterozoic to early Cambrian Delamerian orogen (Miller *et al.* in press). The gold-bearing Stawell corridor occupies a central position within this northwest-trending linear fault system, extending northwards for over 200 km from the Stawell gold mine under the younger Murray Basin sediments (Figure 5-1), and southwards for over 100 km beneath the Newer Volcanics. We seek to constrain the 3-D crustal architecture of the region and from this to generate predictive models and concepts on area selection criteria that may lead to new mineral discoveries in the belt (Rawling *et al*. Chapter 3). This research augments the dome modelling within the Stawell corridor itself (Schaubs *et al*. Chapter 4). that has a direct bearing on prospect scale evaluation. The 3-D model described here covers an area of ~150x150 km to a depth of ~20 km, with the eastern boundary of the model being the Avoca Fault and the western boundary as the Mouchong Fault (Figure 5-1). The model is naturally a non-unique representation, one that can be modified as more data and new interpretations come to light, but is considered geologically reasonable, based on our interpretation of available data. It has been tailored with the objective of deriving

crustal scale geometries relevant to targeting gold mineralisation, and evaluating such scenarios through numerical fluid flow modelling (Rawling *et al*. Chapter 3).

The construction of regional scale models forces decisions regarding the tectonic assembly that are inherently ambiguous, and rely on a sound geological understanding of the terrain of interest. Inputs used in construction of the 3-D model are derived from a standard geological legend (Table 5-1). Mapping at 1:100,000 and 1:250,000 scales by GeoScience Victoria has focussed in the better exposed areas to the south, and is complimented by aeromagnetic and gravity coverage that identifies Palaeozoic signatures under cover to the north (VandenBerg *et al*. 2000). In addition, seismic data acquired by Geoscience Australia (Korsch *et al.* 2002) provides important constrains on the crustal geometry. The earlier (Delamerian) history of the area is still being un-ravelled, through isotopic dating and structural/metamorphic analysis (Miller *et al.* in press; Phillips *et al.* 2002). We are largely concerned here with the imprint of the convergent and better understood Lachlan orogeny, although the structures themselves may in part originate from re-activation of Delamerian features. The major elements of the geological history involve early Cambrian (Delamerian orogeny) accretion of fore arc or back arc material onto a continental margin, formation of a volcanic arc in an extensional setting during the Cambrian, foreland basin development in the Cambro-Ordovician, leading to convergence and oblique slip that culminated in the early to mid Devonian Tabberabberan orogeny. The geological setting shows many similarities to western Tasmania where Proterozoic rocks are exposed and have been similarly modelled in 3-D (Denwer *et al.* 2004).

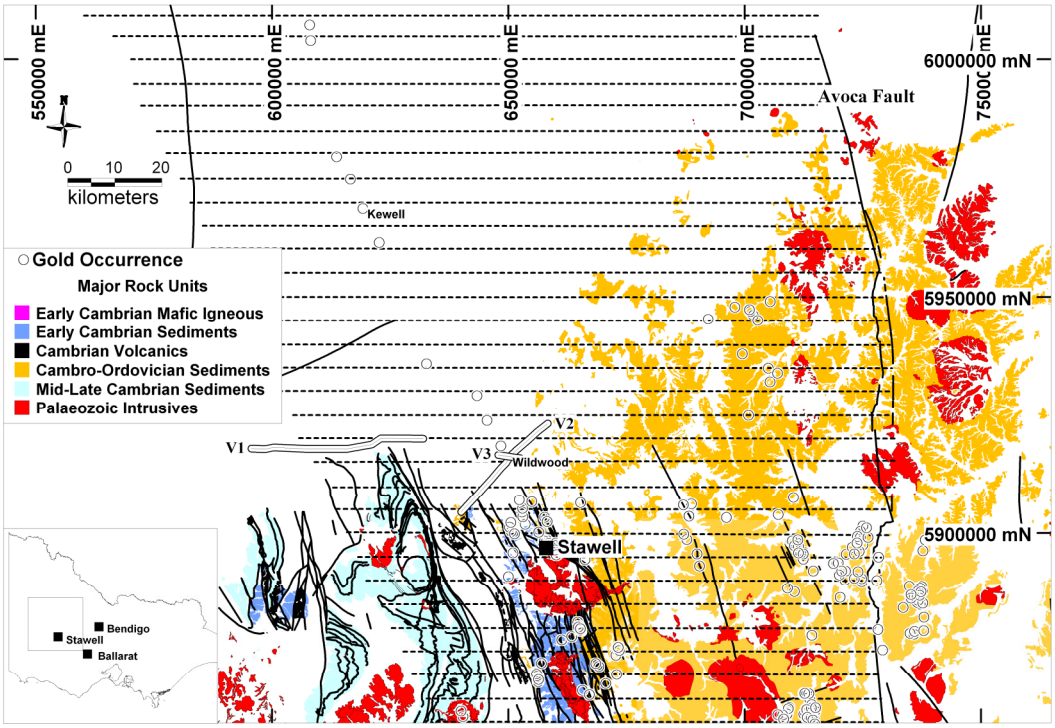

Figure 5-1: Distribution of major geological elements in region covered by 3D model, showing bedrock gold occurrences (Kewell and Wildwood prospects labelled), major faults (black lines), seismic traverses (V1, V2, V3), geological cross section lines (dashed, E-W lines) ; white regions represent post-Palaeozoic cover.

Unit	Name	Components	Age	Max Thickness	Avg Density
Basement	Un-named	Metasediment?	Proterozoic	unknown	
Oceanic-affinity suite	Mt Dryden, Dimboola	Ultramafics, bonninites	Cambrian		
Mafic Domes	Magdala	Tholeiites, basalts	Cambrian		
Metasediments	Mine Schist, Nargoon Gp		Cambrian		
Volcanics	Stavelely		Cambrian		
Magmatic suite (1)			Cambrian		
Clastic Sediments (1)	St Arnaud Glenthompson		Cambrian-Ordovician		
Clastic Sediments (2)	Castlemaine, Grampians		Ordovician-Silurian		
Magmatic suite (2)		Intrusives, extrusives	Devonian		
Cover rocks	Newer Volcanics, Murray Basin	Volcanics, Mineral sands	Mesozoic to Recent		

Table 5-1: Standard geological units used in the modelling with representative properties.

Methodology

Major bounding surfaces in the model are defined from mapped geology and from interpretation of potential field and seismic data. The distribution of the lithostratigraphic components (Table 5.1) is in large part determined by fault geometries. As a first order approximation of faults that may have significant down-dip or depth extent, the mapped faults were ranked by length (Figure 5-2). The major northwest-tending faults are moderate to steeply inclined, both to the east (Moyston Fault) and west (Coongee Fault), and show relatively straight to curvilinear surface traces. Other long fault elements are low-angle thrust faults in the Grampians to the west (Figure 5-2; Leuctra Fault). A generally good correlation is observed between the major faults and the positions of gradients in the aeromagnetic and gravity data (Figures 5-3 and 5-4). This gives a reasonable degree of confidence in extending structures under cover based on geophysics alone. An initial objective is to constrain the near-surface geology and link this to the geophysical gradients and signatures as basis for development of serial cross section interpretations and rendering these into 3-D space.

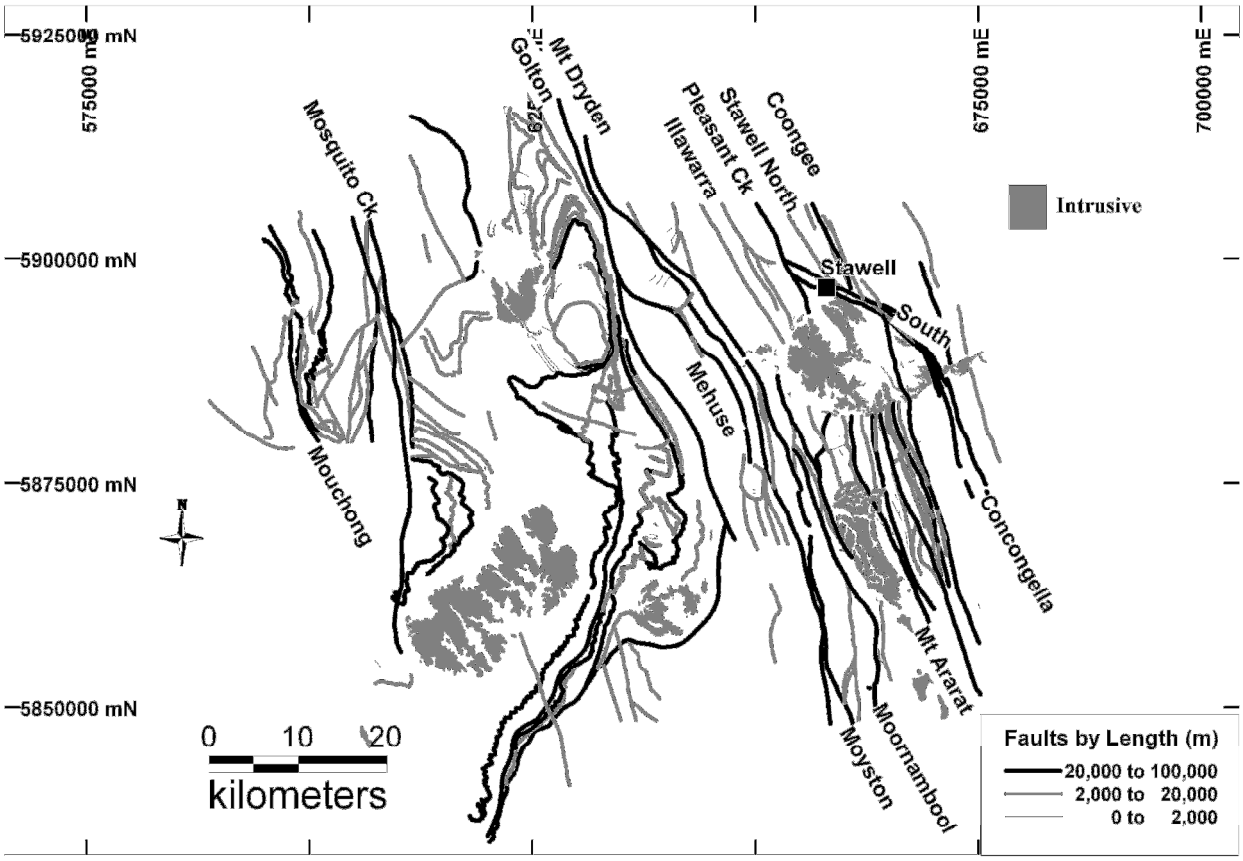

Figure 5-2: Distribution of mapped faults and intrusive bodies from 1:100,000 scale geology, with coding of faults by strike length, with significant faults named.

The regional aeromagnetic and gravity data were interpreted with an emphasis on the nature of the gradients. An automated edge detection technique, called multiscale wavelet edges ('worms'), was used. This technique, developed by CSIRO and Fractal Graphics, reduces ambiguities inherent in the interpretation of potential field data (Hornby *et al.* 1999). Worms are points of maximum gradient derived from wavelet transformation and upward continuation of potential field grids that can be visualized as 3-D arrays; such arrays combine visually as variably coherent worm 'sheets' (Archibald *et al.* 1999). The 3-D points (xyz) include the variable, *w,* a measure of the amplitude or strength of the gradient. Worms originate at the lowest (fine scale) level and persist to varying levels of upward continuation (coarse scale), with the maximum height of individual worm sheets being a function of the nature of the gradient (Archibald *et al.* 1999). Fine scale worms relate to near-surface gradients, and coarse scale worms usually relate to deeper sources. Exceptions to this are seen, for example, where flat lying, near-surface bodies (e.g. basalts) can produce coarse scale worms at the edge of the body. Levels of upward continued for the western Victorian data were 30 km for the pseudo-gravity transformed aeromagnetics from a grid cell size of 200 m (Figure 5-5), and 50 km for the gravity from a grid cell size of 500 m (Figure 5-6). This yields information on contacts that may persist to >15 km depth. Contacts with no detectable density contrast across them, such as cross-faults, are invisible to the worming process but may be inferred through linear truncations and offsets in subjacent worm sheets.

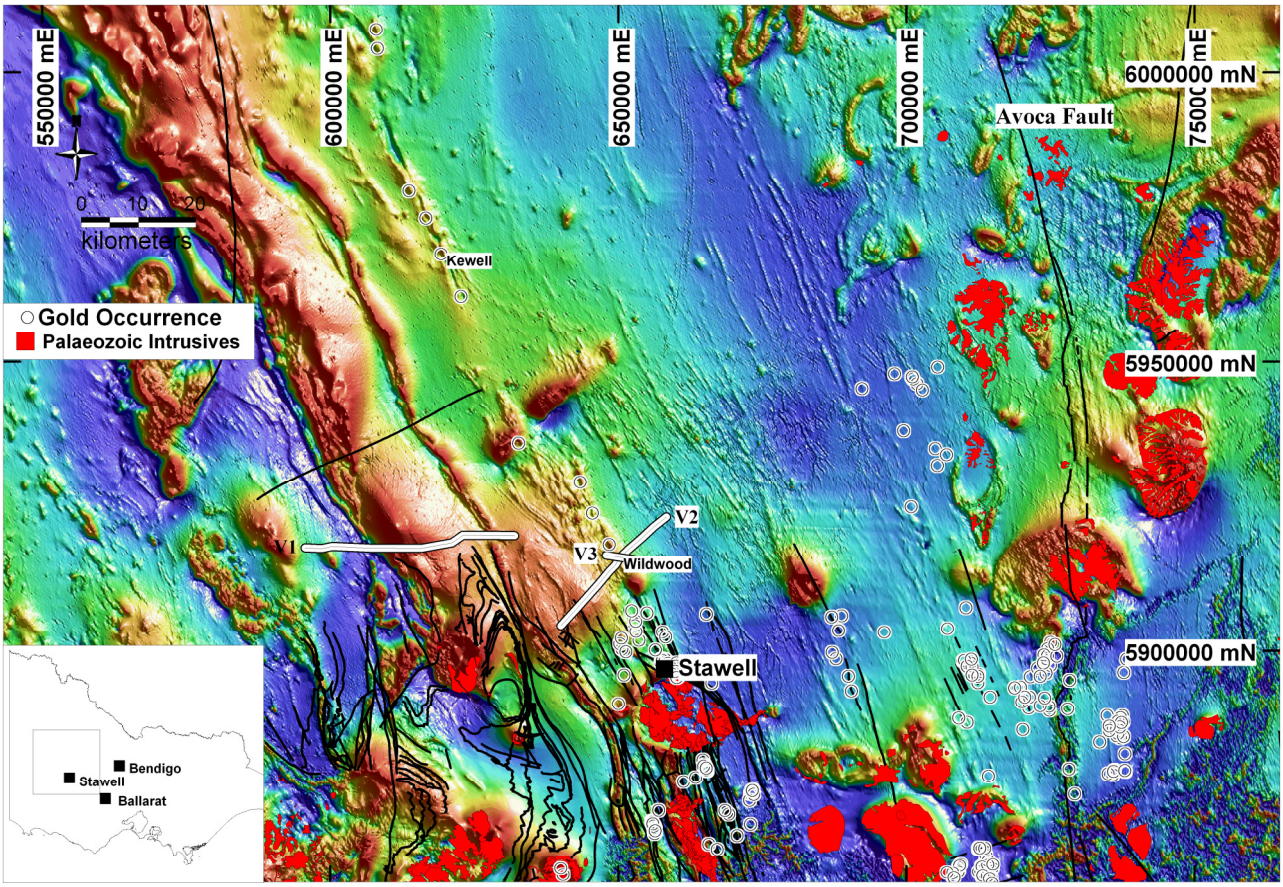

Figure 5-3: Total magnetic intensity aeromagnetic image of western Victoria with superimposed geological map distributions of granites (red), faults (black lines) and positions of seismic traverses (blue lines) .

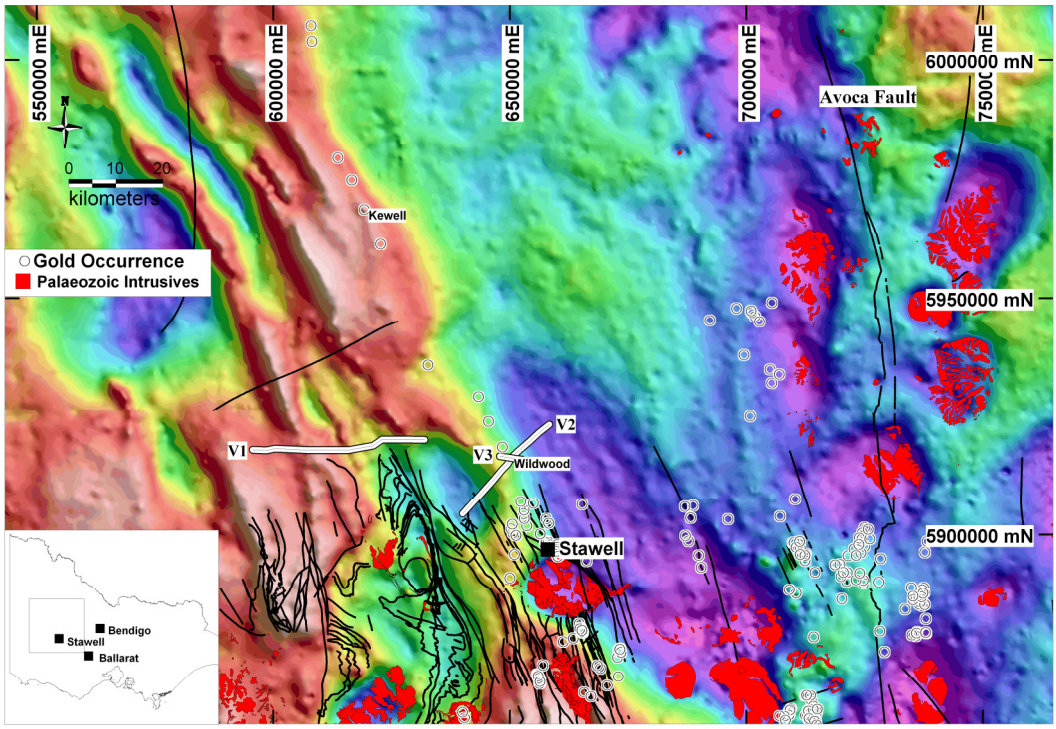

Figure 5-4: Bouguer gravity image of western Victoria with superimposed geological map distributions of granites (red), faults (black lines) and positions of seismic traverses (blue lines).

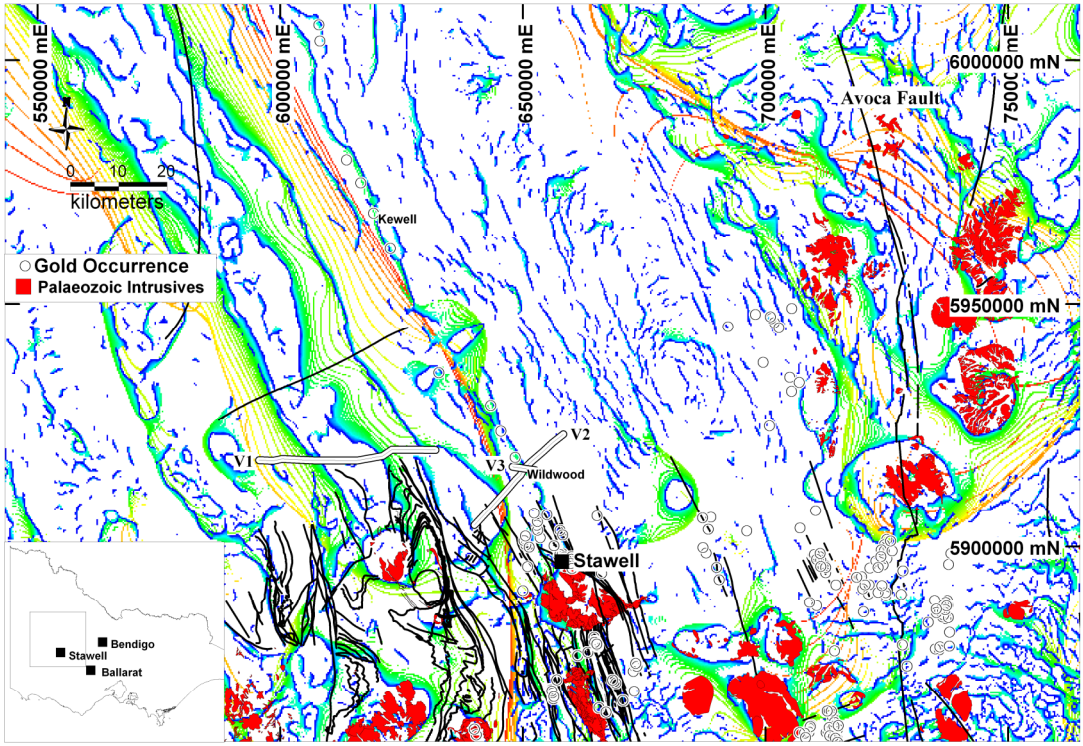

Figure 5-5: Image of regional scale aeromagnetic worms of western Victoria with superimposed geological map distributions of granites (red), faults (black lines) and positions of seismic traverses (blue lines). Worm points are coloured by height of upward continuation, blue being near-surface/fine scale and green-to-red being higher level/coarse scale gradients.

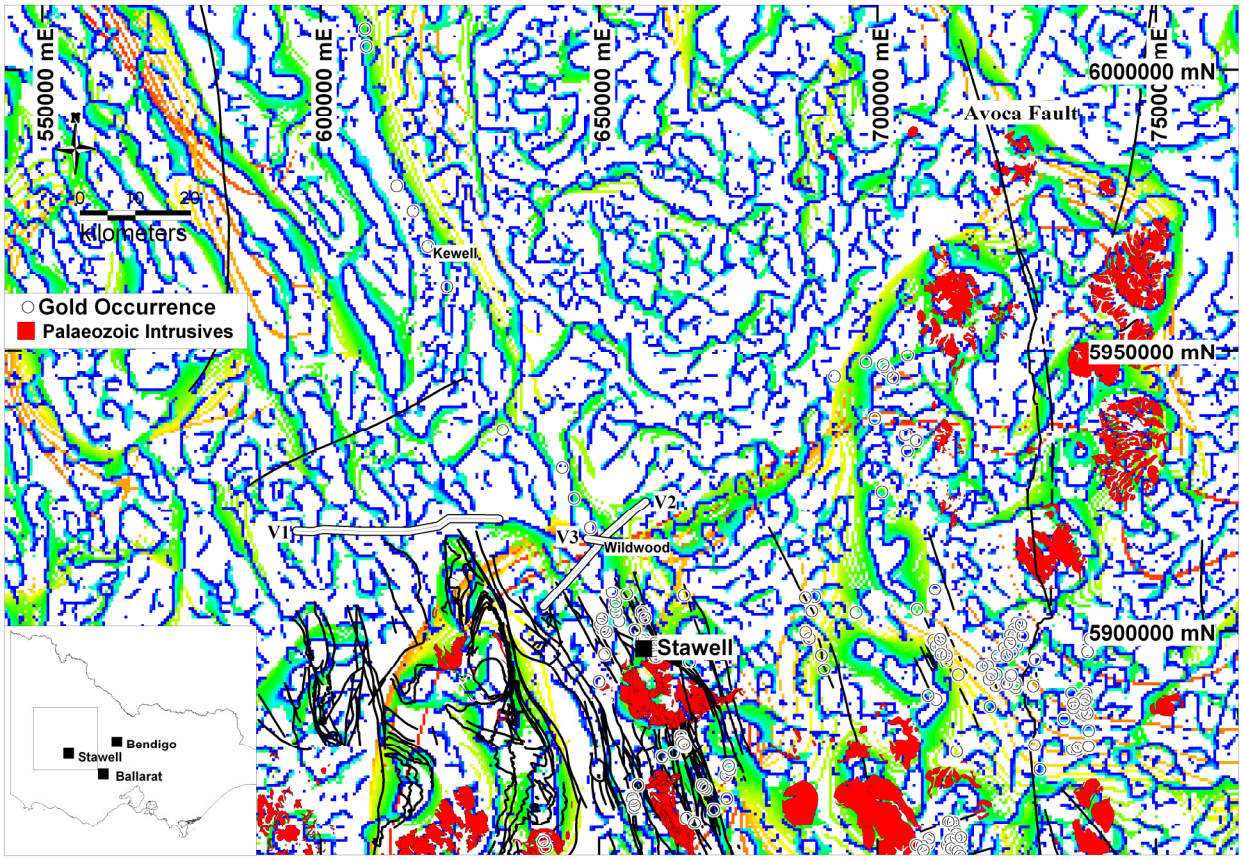

Figure 5-6: Image of regional scale gravity worms of western Victoria with superimposed geological map distributions of granites (red), faults (black lines) and positions of seismic traverses (blue lines). Worm points are coloured by height of upward continuation, blue being near-surface/fine scale and green-to-red being higher level/coarse scale gradients.

A reasonable assumption underlying the interpretation of worms is that singularities in the mass density distribution of the sources correspond *lit-par-lit* with apparent edges in the potential field and that such singularities can be ascribed a geological meaning (Archibald *et al.* 1999). Thus, with some exceptions, coarse scale worms generally derive from more persistent crustal sources, such as penetrative faults. Synthetic models indicate that the dip direction of a worm sheet can be a mirror image its related geological contact (e.g. folds, faults, intrusive bodies), up to the *w* maxima (Holden *et al.* 2000). A rule of thumb that may be used is that the depth extent of a geological feature is approximately equivalent to half the maximum height of upward continuation (z) of the related worm sheet. Typically, persistent gradients (in height and/or length) have most impact on the 3-D geometry. Post-processing of the worms, through vectorisation of both the gravity and aeromagnetic data, generates populations of lines and polygons from which trend, length, height and straightness parameters are derived. These parameters are used to infer the nature of the geological sources, such as faults, intrusives and stratigraphic boundaries, through correlation with mapped geology and by visual interpretation of the morphology of worm sheets in 3-D.

The gravity data (Figure 5-4) was further processed using UBC code to derive 3-D inversion models as an aid to the geological interpretation. This provides some

constraints on the relative positions of different mass distributions in 3-D space for which, however, there are innumerable possible solutions. The gravity inversion was not constrained by mapped geology in this instance, and a model was chosen from a number of iterations. 2-D slices of the selected inversion model were then used as a backdrop in the construction of thirty one serial E-W cross sections at 1:120,000 scale on 5 km spacing through the region (Figure 5-1). The template for each cross section (Figure 5-7) combines profiles of the upward continued aeromagnetic and gravity worms, a gravity inversion model, and strip maps of geology and worms in the vicinity of the section line. Geological interpretations were drawn from these templates. Once completed, each interpreted section was forward modelled (in GM-SYS), compared to the actual potential field profiles, and the model modified according to visual best fit criteria (Figure 5-8). For this process, average densities and susceptibilities of units in the standard geological legend were derived from generic values of common rock types in the region (Direen 1999), plus some field data supplied by Leviathan Resources (see table 6-1 in Chapter 6). 3-D surfaces and volumes were subsequently generated in gOcad, and visualisation of the resultant model in relation to other geoscientific data used the FracSIS platform. Details of the methodology are given in Rawling *et al.* (this volume).

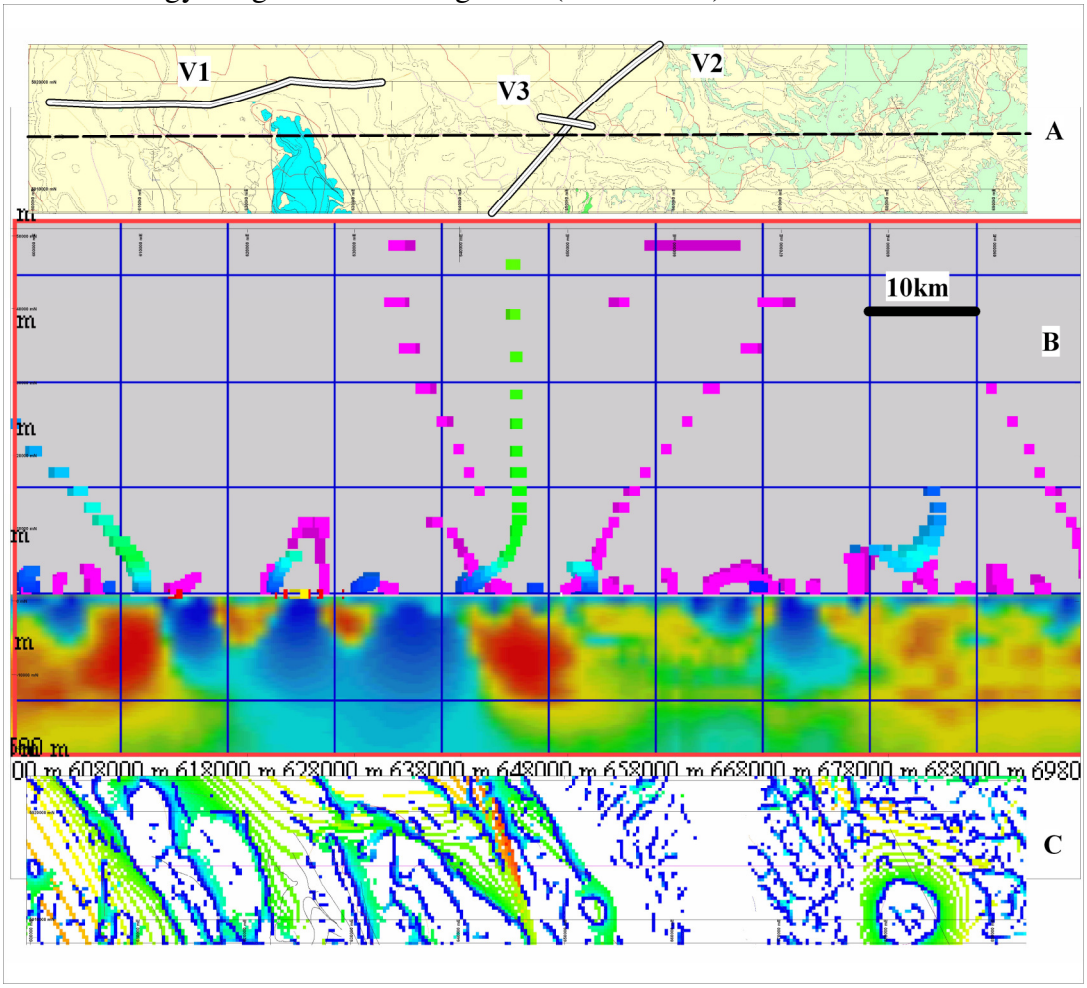

Figure 5-7: Template used for construction of geological cross sections. A) geological map with superimposed positions of seismic traverses (V1, V2, V3) and line of section (dashed line at 5915000N); B) vertical profile of worm points at different heights of upward continuation above ground surface (magenta are gravity worms, blue-green are magnetic woirms coloured by amplitude) and image of unconstrained gravity inversion below ground surface to 20km depth

(red are more dense bodies); C) map of aeromagnetic worms at same location as geology map. Scale bar is 10km, V=H.

The relevance of the 3-D architecture to mineral exploration in this region derives from the concept that large dimension faults penetrating a layered crust can intersect a variety of fluid reservoirs and thermal gradients and promote the formation and localisation of major ore systems. The association of faults with potential field gradients, often a key tool in exploration targeting (Betts & Lister 2002), has important consequences when exploring in under-cover terrains. The recognition of continental scale lineaments in the gravity field of Australia led to the discovery of giant ore deposits, such as Olympic Dam (O'Driscoll 1990). Hobbs *et al.* (2000) drew attention to the Barramundi worm, a deep seated gravity gradient in northern Australia, and the proximity of giant Proterozoic sediment-hosted massive sulphide deposits. Similarly, Archibald *et al.* (2001) find a strong correlation between major gravity worms in Australia and the locations of large Ag-Pb-Zn deposits, and to a lesser degree with major Cu deposits. Drawing on lessons from related pmd*CRC projects in the Yilgarn of Western Australia (A1 project) and in Tasmania (T3 project), we evaluate the impact of potential field gradients and their interpreted 3-D geological entities on gold distributions in western Victoria, seeking exploration-related outcomes that lead to better informed area selection decisions.

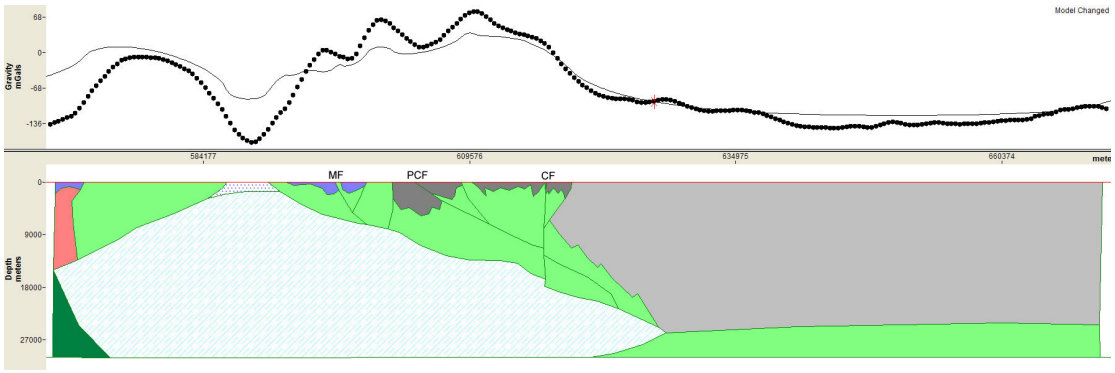

Figure 5-8: Example of forward modelleing of the gravity data using GM-SYS profile analysis and interpretative geological cross section. V=H. The gravity data was extracted from east-west oriented transect that parallels the seismic line (from 588500E to 700500E and 5920000N). The units in the geological section are dominated by a proposed Proterozoic block (inclined stripes) overlain by mafic units (light green), Glenthompson sandstone (blue) and St Arnaud Group (grey). In the west of the section there is a granite (red) and ultramafic unit (dark green) that would underlie Glenthompson sandstone. The Grampians group is thrust over the Proterozoic block (horizontal stipple). CF -Coongee Fault, MF - Moyston Fault, PCF - Pleasant Creek Fault.

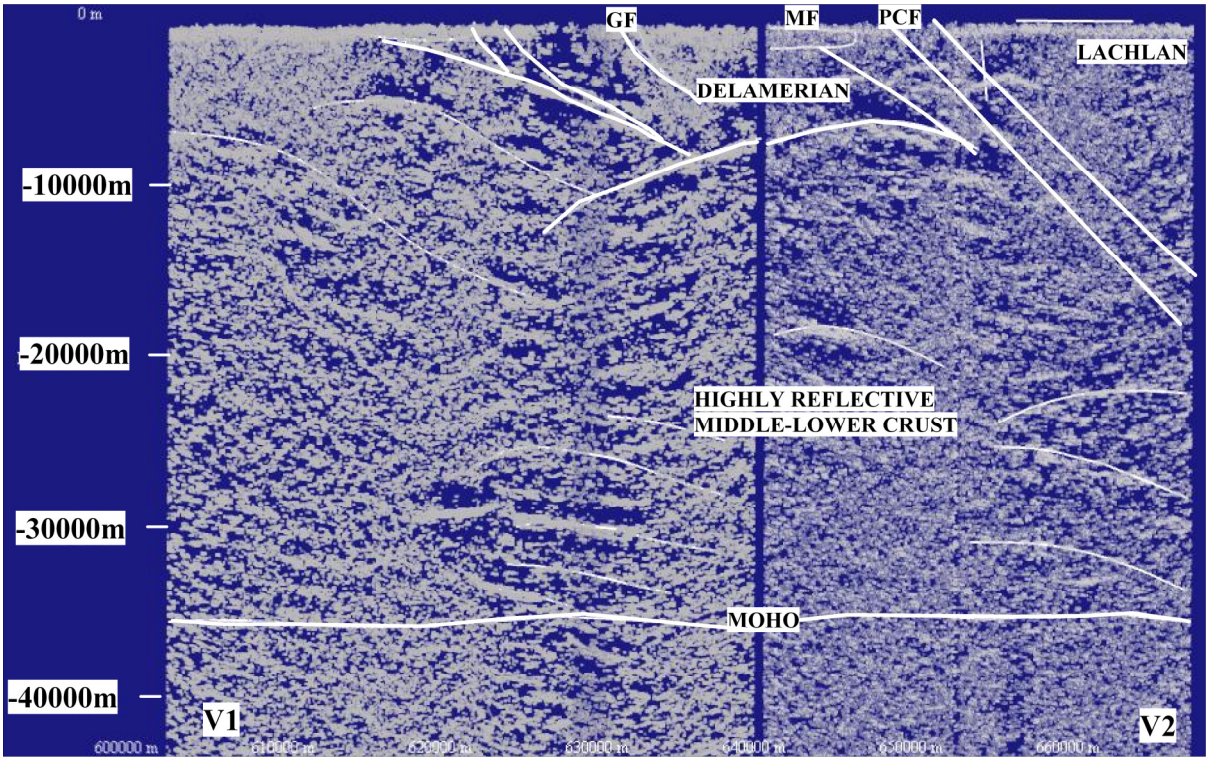

Figure 5-9: Interpreted seismic reflection profiles of lines 97AGS-V1 ("V1") and 97AGS-V2 ("V2"), GF = Golton fault, MF = Moyston Fault, PCF = Pleasant Creek Fault, V~H. (Adopted from Korsch *et al*. 2002, Fig. 6)

Geological interpretations

Seismic reflection profiles (Figure 5-1) provide an entry point for the cross section interpretation and are a primary constraint on the gross geometry of the 3-D model. Three slightly offset east-west lines, up to 69 km long, were acquired and interpreted by Korsch *et al.* (2002). These were positioned to reveal the crustal architecture across the northern extensions of major interpreted faults in the region (Figure 5-1). The profiles highlight, in particular, the Moyston and Pleasant Creek Faults as large scale, east-dipping sub-parallel features that can be traced to over 15 km depth (Figure 5-9). Teleseismic data (Graeber *et al.* 2002) indicates a velocity contrast in the mantle that Korsch *et al.* (2002) relate to the downdip position of the Moyston-Pleasant Creek fault system, suggesting the dislocation perhaps extends to approximately 100 km depth. East of these faults, in the upper crust, the Coongee Fault is a major steep, west dipping structure, based on mapped geology and potential field worms, but is not imaged in the seismic data. This upper crustal fault architecture overlies a broad arch-like reflector (Figure 5-9), here interpreted as a décollement, and termed the Western Fault in our model. The depth to the top of the décollement is approximately 6 km in the plane of the seismic profile (Figure 5-9). Beneath this, the middle to lower crust is highly reflective, internally duplexed and is inferred as a sub-Delamerian basement. The Moho is defined at about 35 km depth as a slightly undulating surface at the base of the highly reflective middle to lower crust (Korsch *et al.* 2002).

The Bouguer gravity image shows a pattern of regional scale northwest-trending anomalies (Figure 5-4). A prominent feature is the distribution of high density material in the northwest (under cover) and this signature diminishes in intensity

southwards towards the outcropping areas. The high density material is attributed to Palaeozoic lithostratigraphic sources. The low density material in the southwest of this region is largely related to a series of Devonian granitoids. The eastern boundary of the regional scale gravity ridge appears to correlate with the position of the Coongee Fault (Figure 5-4). Major gradients in the gravity data, as portrayed by the worm sheets (Figure 5-6), are northwest-trending and these mirror the strike of major faults, lithostratigraphic packages and intrusives. The processed worm vectors (Figure 5-10) show the northwest-trending gradients are typically truncated by a family of northeast-trending cross structures, interpreted as faults. Many of the semicircular gradients relate to the margins of intrusive bodies, and a northeast-trending control in the alignment of intrusive-related gravity lows is evident (Figure 5-10).

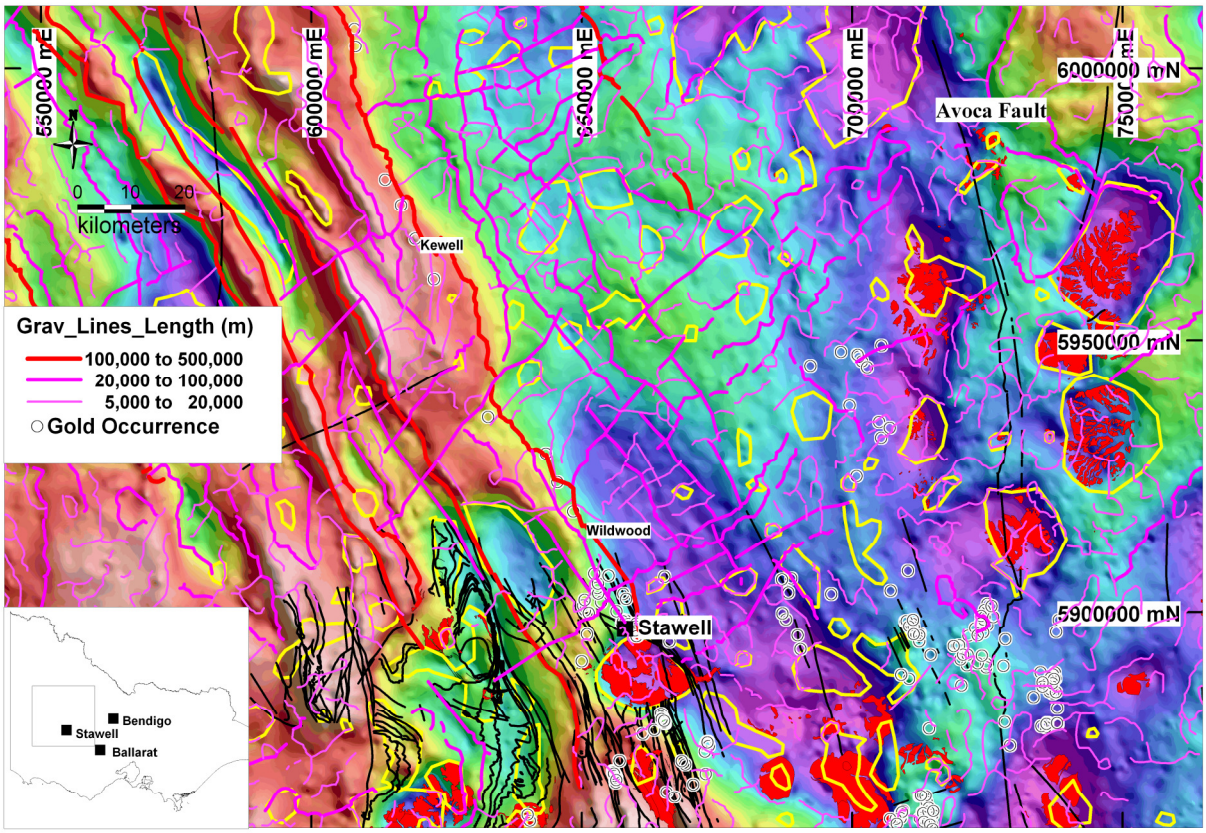

Figure 5-10: Interpreted gravity worm lines coloured by strike length (filtered for > 5km) with outlines of discrete gravity lows (yellow polygons), and superimposed geological map distributions of granites (red), faults (black lines).

The aeromagnetic data yields a wealth of detail on the Palaeozoic and younger geological elements (Figure 5-3). High susceptibility Palaeozoic units chiefly relate to Cambrian ultramafics, the Magdala basalts, the Stavely volcanics and Cambrian granites. These units mainly occur in the western parts of the region, associated with northwest-trending anomalies. Lower susceptibility rocks predominate in the east. The Coongee Fault appears to delineate this regional scale susceptibility gradient. High susceptibility Devonian plutons are widely distributed, and several are aligned along northeast and northwest trends. There are other granitoids of this suite that are

non-magnetic (e.g. the Stawell granite; Figure 5-11) and some are zoned in their magnetic properties Moore 2003). The Newer Volcanics, in the south, and linear trains of mineral sand deposits in the Murray Basin, to the north, also have high susceptibility. The wormed data (Figure 5-5) largely conforms to the interpretation by the Geoscience Victoria (Moore 2003), with some modifications of these being made in the 3-D model, such as the interpreted fault linkage through, or below, the Stawell granite and across the South Fault (Figure 5-2), and the continuity of major boundaries under the Murray Basin. Interpreted faults from the magnetic worms (Figure 5-10) suggest a linear system of strike extensive northwest-trending structures. Some east-southeast-trending faults, such as the South Fault, are evident which offset the dominant northwest structures. There is a later set of northeast trending faults that show small or negligible apparent lateral displacements, but some have considerable strike continuity suggesting a vertically extensive character. Intersections of northeast and northwest trends are in several places occupied by late Devonian intrusives. We have not sought to constrain the 3-D shapes of granites in the modelling. Given the late stage emplacement in the structural history, the granites have been treated as transparent to the traces on the 3-D fault surfaces that we have defined, such that faults are connected through the granites. This approach works well in the case of the Stawell granite where gradients can be traced trough the region occupied by the granite (Figure 5- 5), and suggests the granite is a flat-based body.

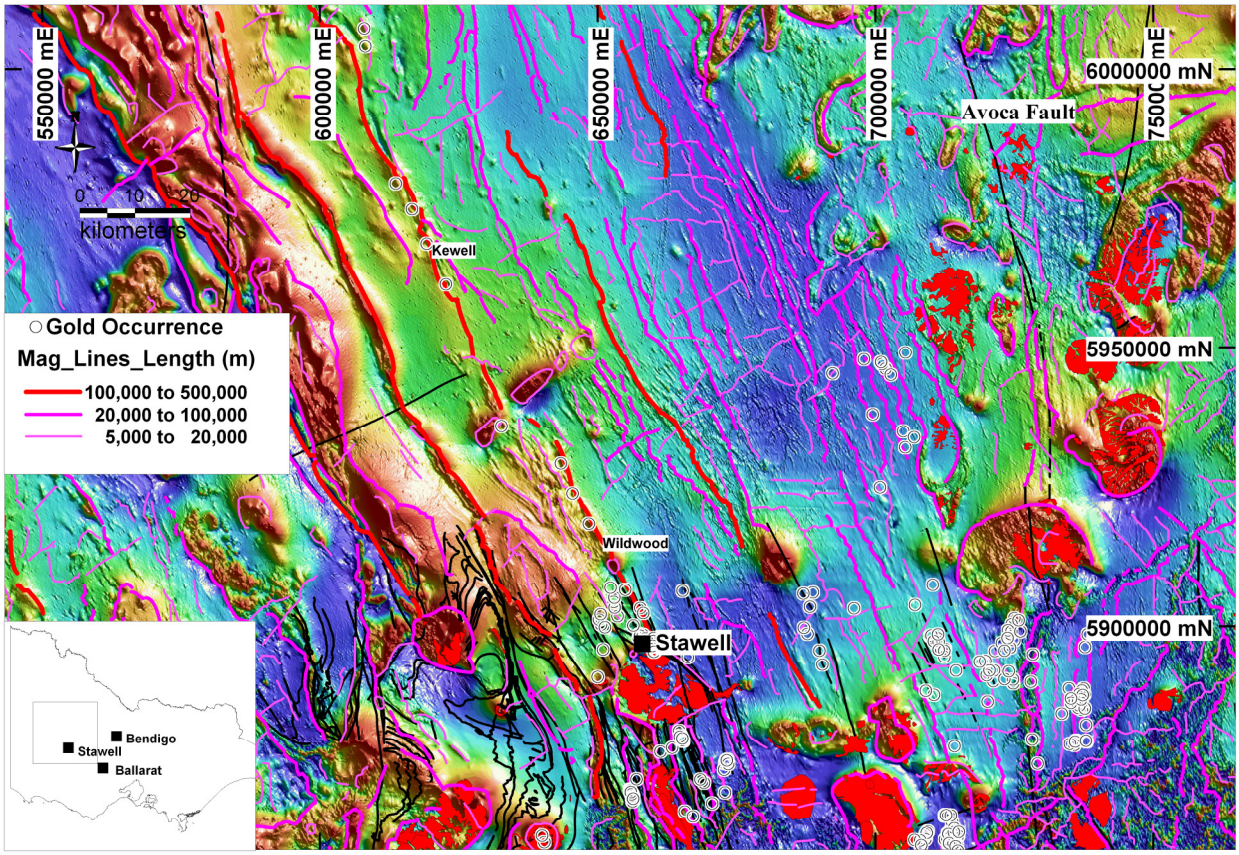

Figure 5-11: Interpreted magnetic worm lines coloured by strike length (filtered for > 5km) with outlines of discrete gravity lows (yellow polygons), and superimposed geological map distributions of granites (red), faults (black lines).

The wormed data were vectorised and imaged to assist with delineation of major gradients and boundaries to be incorporated in the 3-D model. Images of edge length (e.g. Figure 5-12), height and dimension (=length*height) for the magnetic and gravity interpretations of fault-related gradients emphasise the crustal scale gradients. A combined gravity and aeromagnetic edge length parameter serves to summarise the main fault-related gradients of interest (Figure 5-13). This shows a relative coherence between the aeromagnetic and gravity gradients.

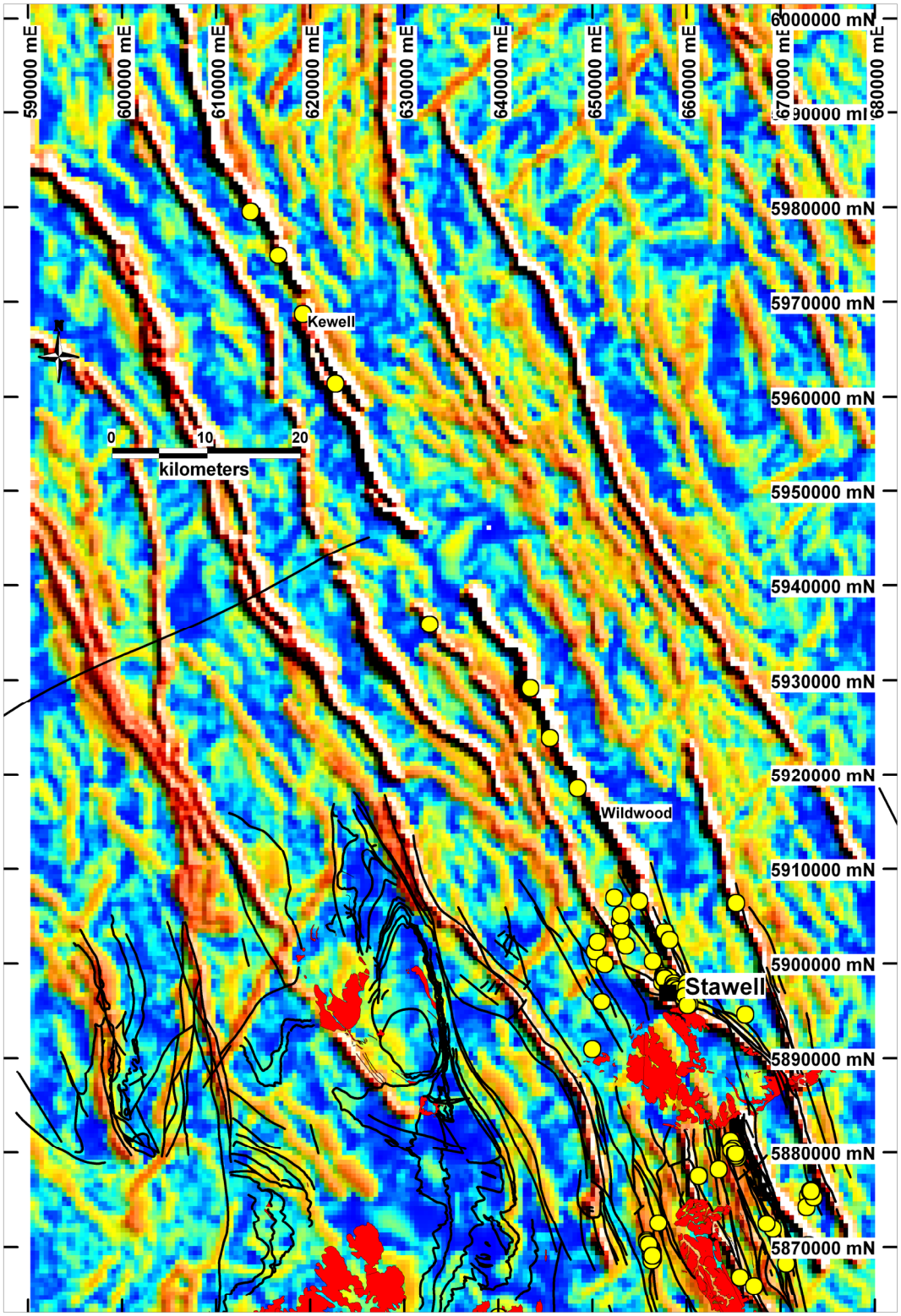

Figure 5-12: Image of interpreted magnetic worm lines with colour intensity representing strike length (white/red = high values), and superimposed geological map distributions of granites (red), faults (black lines) and gold occurrences (yellow dots).

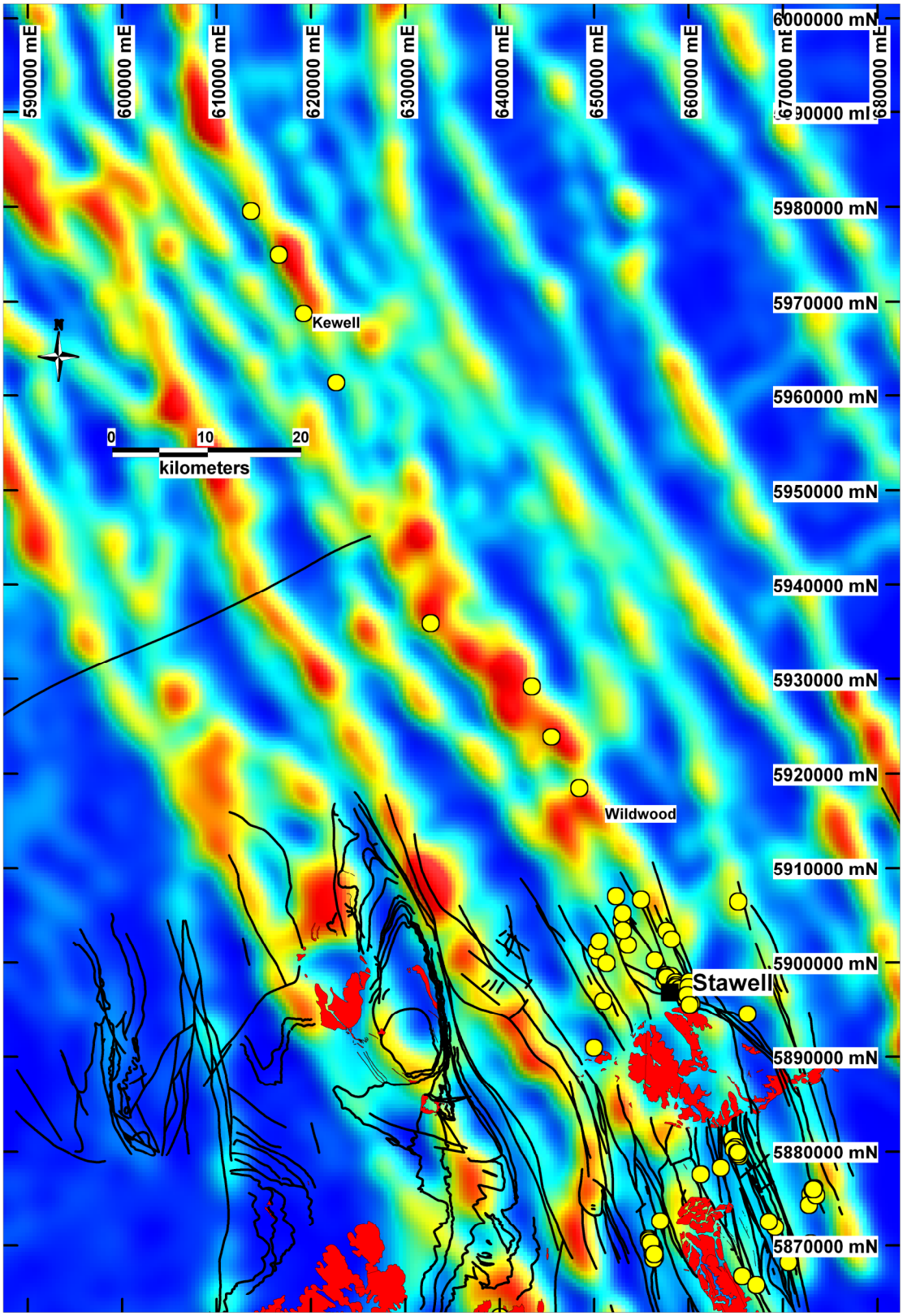

Figure 5-12: Image of interpreted magnetic worm lines combined with gravity worm lines with colour intensity representing strike length (red = high values), and superimposed geological map distributions of granites (red), faults (black lines) and gold occurrences (yellow dots).

Using such information, the major faults that were constructed in the 3-D model (Figure 5-14) are, from west to east:

- Mouchong Fault: modelled as a steep east-dipping structure, with an early Cambrian ultramafic sheet in the footwall position. This is interpreted to truncate the west dipping flank of the Western Fault at ~12-18 km depth.
- Escondida Fault: a west-dipping structure inferred from worm data, largely obscured by the structurally overlying Grampian Group. This is located in the up-dip position of the steep west-dipping limb of the Western Fault culmination, with which it merges at ~5km depth.
- Western Fault: this is interpreted as a basal detachment for the Palaeozoic section. Bouguer gravity data shows a broad high in the northwest that we attribute to stacked Delamerian crustal sources above the detachment. We model the detachment as an undulating surface with a northwest-trending axis of culmination that extends through the 3-D crustal geometry (Figure 5-15). Some of its topology may relate to interaction with northeast-trending cross faults (not modelled in 3-D). We infer a possible breached dome of the basement surface, corresponding to a linear gravity low, beneath the Murray Basin cover sediments to the north (Figure 5-10). The steep western limb of the fault surface may be imposed as a result of folding and faulting, perhaps related to reverse displacements along the Mouchong Fault.
- Fyans Fault: this east-dipping structure branches from the east dipping Western Fault at ca. 5 km depth. This, and the opposite polarity West Boundary Fault, together describe a triangle zone geometry above the culmination in the Western Fault.
- Mehuse Fault: this dips eastwards with a listric geometry and merges with the Western Fault at *ca.*10 km depth. It is similar to the Mouchong Fault, in that it carries an ultramafic slab in its footwall.
- Mt Dryden Fault: this is essentially parallel to the Mehuse Fault, and represents an upper surface detachment to the slice of ultramafic material.
- Moyston Fault: this is interpreted as an east-dipping surface that rejoins the Mt Dryden Fault both to the north and to the south. It is considered as part of a family of faults in this region, rather than being the dominant crustal feature (Korsch *et al.* 2002; VandenBerg *et al.* 2000).
- Illawarra Fault: this is modelled as a steep to moderate east-dipping feature that joins the Western Fault at ca.12 km depth. This interface at depth corresponds with a steepening of the east-dipping Western Fault. There is a 2 km dextral deflection of the fault through the region occupied by the Stawell granite.
- Pleasant Creek Fault: this is sub-parallel to the Moyston Fault for most of the strike length of the model in the south, but continues northwards beyond the Moyston/Mt Dryden intersection. South of the Stawell granite, it is linked with an un-named fault immediately west of the Mt Ararat Fault.
- Coongee Fault: this is represented as a west-dipping, steeply inclined to sub-vertical feature. The downdip extent is interpreted to truncate the Pleasant Creek and Moyston Faults at *ca.*12 km depth in the southern parts of the model, and there is a gradual divergence between these structures northwards. On the basis that the Coongee Fault has undergone strike slip re-activation during the Tabberabberan, it is interpreted to intersect and may cut the downdip position of

the Western Fault below 12 km. The shortening strain accommodated by reverse displacement in the Tabberabberan still retains a grossly normal sense of stratigraphic offset across the Coongee Fault, the eastern footwall of which is in a broad gravity low. This is may be accounted for by a thick sediment pile (St Arnaud Beds) that accumulated, possibly during growth faulting on the Coogee and/or Moyston system in the Cambrian. The St Arnaud Group extends eastwards to the Avoca Fault (Figure 5-1) and is contained by a relatively flat lying enveloping surface, cut by a number of strike parallel faults (Leader *et al.* this volume). The rocks in the hanging wall of the Coongee Fault comprise the poly-deformed Moornambool Metamorphic Complex (Phillips *et al.* 2002). Whereas, the rocks east of the Coongee Fault are greenschist facies and are less structurally complex (Miller *et al.*, sumitted).

- Coongee North Fault: This structure is modelled north of 5950000N as a fault strand along the western margin of the Coongee Fault. It has a similar dip as the Coongee Fault and joins along an inferred sub-horizontal branch line at *ca.*7 km depth.
- South Fault: this is a gentle to moderate NE dipping structure that cross cuts the Pleasant Creek and Coongee Faults and appears to link into the Illawarra and Concongella Faults at its western and eastern ends respectively. There is an apparent gradient in metamorphic grade, decreasing from south to north in rocks west of the Coongee Fault in this region, but it is unclear if this can be related to the South Fault as it is currently expressed as a late structure.
- Concongella Fault: this is represented as a moderate to steep east dipping fault, sub-parallel to the Coongee Fault, and extending to *ca.*14 km depth where it is truncated by the west dipping Landsborough Fault
- Burrom Fault: this is sub-parallel to the Concongella Fault, and is terminated by the Landsborough Fault at ~8 km depth (Leader *et al.*, Chapter 6).
- Landsborough Fault: this is modelled as a steep to moderate west-dipping feature, with the Burrom and Concongella as antithetic faults in its hanging wall. The downdip extent of the Landsborough Fault is interpreted to merge with the Avoca Fault at *ca.* 16km depth.
- Paradise Fault: this is defined in the aeromagnetic worms as a strike extensive structure with a moderate to steep west-dip. It is modelled as linking with the Avoca Fault at depth.
- Percydale Fault: this is portrayed as a moderate west-dipping structure that joins the Avoca Fault at *ca.* 10 km in the south of the model, and this interface deepens to *ca.*15 km in the north.
- Avoca Fault: this regional scale stucture has a dominant north strike, divergent from other regional scale structures. It is interpreted as having a listric, west-dipping geometry and represents a major lower bounding surface in the model. An interface with the east dipping Moyston and Western Faults is inferred at *ca.*18 km depth, and this is sited close to the updip position of the Coongee Fault. Our model interprets the Avoca Fault as truncating the Western-Moyston Fault interface, this being the eastern extend of the sub-Delamerian crustal element.

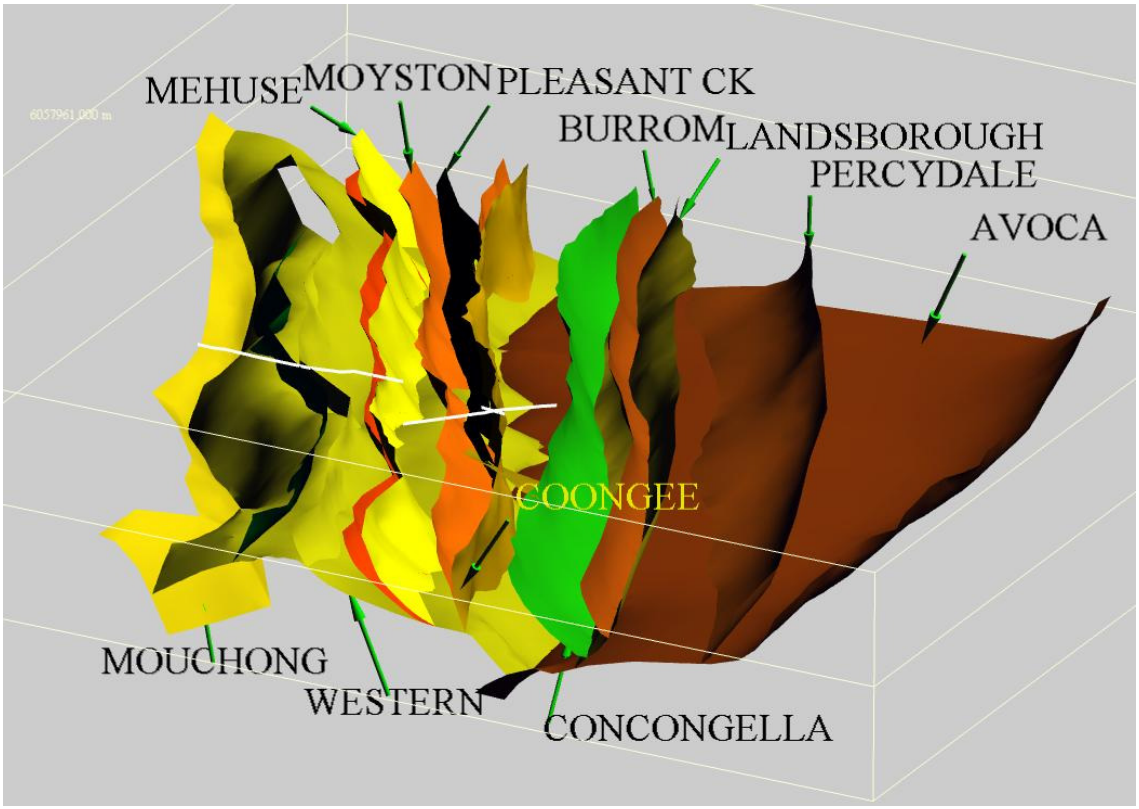

Figure 5-14: Image of major faults in 3D model, perspective view from SE. Positions of seismic tranverses shown as white lines. Vertical grid at 10km spacing.

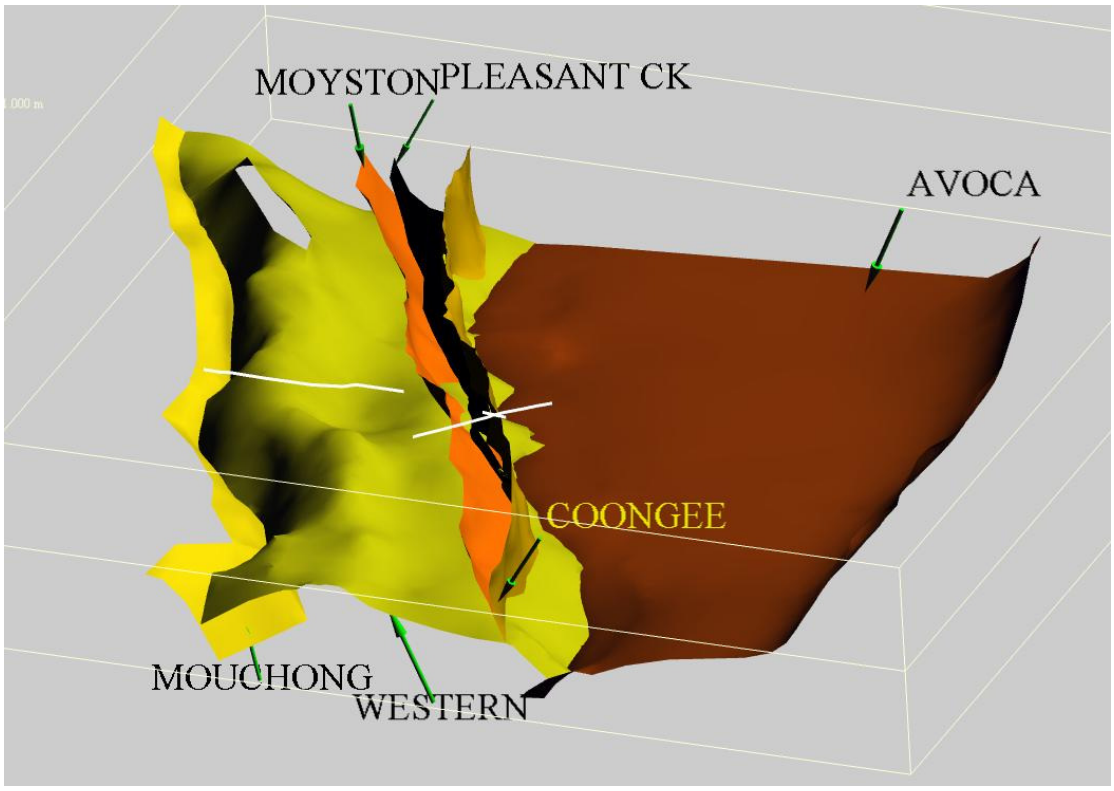

Figure 5-15: Image of selected major faults in 3D model, perspective view from SE, to show relationship of Western Fault arch-like geometry and inferred void where this is cut by the erosion surface in north. Positions of seismic tranverses shown as white lines. Vertical grid at 10km spacing.

Mineral potential mapping

In many mineralised terrains, large dimension faults appear to play a role in the localisation of ore deposits, perhaps by intersecting a variety of fluid reservoirs and thermal gradients. Recent examples using geostatistical analysis of gold distributions in the Yilgarn region (Bierlein *et al*. in review) and in Tasmania (Murphy *et al*. 2004) show a correlation with long wavelength potential field gradients that are attributed to depth extensive faults. In both instances, it appears that the second order faults proximal to first order features are more metal prone. In western Victoria, major faults are known to influence the distribution of orogenic gold deposits, particularly in the hanging wall of the west-dipping Coongee Fault along the northwest- trending Stawell corridor (Figure 5-1). A number of new prospects have already been defined by Leviathan Resources, successfully targeting basaltic domes along this trend.

To evaluate this relationship further, the gold-associated locations (from Geoscience Australia's MinOcc and Leviathan Resources data) were ranked qualitatively by occurrence type to portray a size distribution, according to: 1- unspecified, 2- alluvial, 3 – hard rock prospect, 4- advanced prospect (old shaft or mine or advanced target, 5 – Defined resource or operating mine (Magdala and Wonga mines). This data represents a mixed population of gold mineralising events, each with different controls, including early orogenic-related Magdala type deposits (Miller & Wilson 2002) and later intrusive-related Wonga type deposits (Miller & Wilson 2004). These deposit types can be overlapping in space, as at Stawell. The data are plotted as a whole in relation to the total edge length distributions (Figure 5-13), from which some broad empirical relationships may be drawn. It is evident that the Magdala type gold occurrences are spatially related to the trace of the Coongee Fault. The distribution of basalt domes, based on aeromagnetic interpretation, suggests some greenfields targets exist in the northern extents of the Coongee Fault.

If this is a real association, rather than a sampling bias, why then is proximity to this fault more prone to localising gold? A factor that we suggest may be significant is the dip direction, considering that this fault has a steep west dip compared to the east-dipping faults around it. Its geometry suggests a back-thrust developed above a deep crustal ramp. This may perturb the regional flow paths of mineralising fluids. The source of gold bearing fluid is not well constrained in the orogenic deposit type and, rather than being locally sourced, deeper sources in the crust, such as bonninites (Crawford *et al.* 1989), are considered possible. Therefore, the depth to which the Coongee Fault has to extend to intersect such source regions is at least to the interface with the Pleasant Creek-Illawarra-Moyston system at *ca*. 12 km depth. In our 3-D model this broadly overlies the leading edge of the inferred Proterozoic crustal element, and is perhaps the ultimate driver for gold bearing fluids (Rawling *et al.* Chapter 3).

Conclusions

Our analysis is an interpretation of regional scale 3-D geology that has been constructed so as to derive some exploration targeting concepts. An inferred Proterozoic block is central to this modelling, interpreted as a continental ribbon during the early Palaeozoic history of the region, and regarded as an outboard fragment of the Rodinian continent. It is currently allochthonous with respect to the

Delamerian shear zones that enclose it, and along which fore arc or back arc mafic to ultramafic material was emplaced westwards. Parallels can be drawn with western Tasmania where Proterozoic rocks are dissected by ultramafic-associated fault slivers. The geometry of the 3-D model suggests there is a substantial volume and large lateral extent of fore arc or back arc elements in the middle crust. Such rocks may provide a viable source region for gold bearing fluids. The spatial distribution of orogenic gold deposits with certain penetrative faults is here related to the position of the leading edge to the Proterozoic block at depth, as a driver for fluid flow during orogenic convergence.

References

ARCHIBALD N. J., GOW P. & BOSCHETTI F. 1999. Multiscale edge analysis of potential field data. *Exploration Geophysics* **30**, 38-44.

ARCHIBALD N. J., HOLDEN D., MASON R., POWER B., BOSCHETTI F., HOROWIT, F. & HORNBY, P. 2001. There's a worm in my soup: wavelet based analysis for interpretation of crustal scale potential field data and implications fore identification of giant hydrothermal ore systems. *Abstract in 2001- A Hydrothermal Odyssey, Townsville, Queensland, p5-7.*

BIERLEIN F. P., LEES T. C., MURPHY F. C. & WEINBERG R. in review. Orogenic gold deposits and major fault zones: Targeting tools applied to the Eastern Goldfields, Yilgarn craton, Western Australia. *Mineralium Deposita.*

BETTS P. G. & LISTER G. S. 2002. Geodynamically indicated targeting strategy for shale-hosted massive sulphide Pb-Zn-Ag mineralisation in the Western Fold Belt, Mt Isa terrane. *Australian Journal of Earth Sciences* **49**, 985-1010.

CRAWFORD A., FALLOON T. J. & GREEN D. H. 1989. Classification, petrogenesis and tectonic setting of bonninites. *In*: Crawford, A. J. ed. *Bonninites and related rocks*, pp1-49, Unwin Hyman, London.

DENWER K., KEELE R., SEYMOUR D. & MURPHY B. 2004. Geoscientific data compilation and three-dimensional geological model of Tasmania. Abstract *in* 17th AGC, Hobart, **73**, p66.

DIREEN N. G. 1999. Geology and geophysics of the Koonenberry Belt, far western New South Wales, and eastern Australian correlates: timing, development and prospectivity of the Late Neoproterozoic-Plaaeozoic Gondwana margin. Unpublished PhD thesis, University of Tasmania.

GRAEBER F. M., HOUSEMAN G. A. & GREENHALGH S. A. 2002. Regional teleseismic tomography of the western Lachlan Orogen and the Newer Volcanic Province, southeast Australia. *Geophysical Journal International* **149**, 249-266.

HOBBS B. E. H., ORD A., ARCHIBALD N. J., WALSHE J. L., ZHANG, Y., BROWN M. & ZHAO, C. 2000. Geodynamic modelling as an exploration tool. *in After 2000- The Future of Mining, Sydney, p34-49.*

HOLDEN D., ARCHIBALD N. J., BOSCHETTI F. & JESSELL, M. W. 2000. Inferring geological structures using wavelet-based multiscale edge analysis and forward models. *Exploration Geophysics* **31**, 617-621.

HORNBY P., BOSCHETTI F. & HOROWITZ F. 1999. Analysis of potential field data in the wavelet domain. *Geophysics Journal International*, **137**, 175-196.

KORSCH R. J., BARTON T. J., GRAY D. R., OWEN A. J. & FOSTER D. A. 2002. Geological interpretation of a deep seismic-reflection transect across the boundary of the Delamerian and Lachlan Orogens, in the vicinity of the Grampians, western Victoria. *Australian Journal of Earth Sciences* **49**, 1057-1075

LEADER L. D., RAWLING T. J. & WILSON, C. J. L. (this volume) Forward modelling of geophysical data arcoss the St Arnaud Group, western Victoria.

MILLER J. MCL. & WILSON C. J. L. 2002. The Magdala Lode System, Stawell, southeastern Australia: structural style and relationship to gold mineralization across the western Lachlan Fold Belt. *Economic Geology*, **97**, 325-349.

MILLER J. MCL. & WILSON C. J. L. 2004. Stress controls on intrusion-related gold lodes: Wonga gold mine, Stawell, Western Lachlan Fold Belt, southeastern Australia. *Economic Geology*, **99,** 941-963.

MILLER, J. MCL, PHILLIPS, D., WILSON C. J. L. & DUGDALE L. J. in press, Evolution of a reworked orogenic zone: the boundary between the Delamerian and Lachlan Orogens, SE Australia. *Australian Journal of Earth Sciences*.

MILLER J. MCL, WILSON C. J. L. & DUGDALE L. J. submitted Ordovician to Early Devonian structural evolution of the western Victorian gold deposits. *Australian Journal of Earth Sciences*.

MOORE D.H., 2003. St Arnaud 1:250000 map: a geological interpretation of the geophysical data. *Victoria Initiative for Minerals and Petroleum, Report* **8x**. *Department of Primary Industries, Victoria.*

MURPHY F. C., DENWER K., KEELE R., GREEN G., KORSCH R. J., & LEES T. C. 2004. Prospectivity analysis, Tasmania: where monsters lurk? Abstract *in* 17th AGC, Hobart, **73**, p. 102.

O'DRISCOLL E. S. T. 1990. Lineament tectonics of Australian roe deposits, *in* Hughes, F.E., ed., Geology of Australian and Papua New Guinean Mineral Deposits. *The Australian Institute of Mining and Metallurgy*, Melbourne, 33-41.

PHILLIPS G., MILLER J. MCL & WILSON C.J.L. 2002. Structural and metamorphic evolution of the Moornambool Metamorphic Complex, western Lachlan Fold Belt, southeastern Australia. *Australian Journal of Earth Sciences*. **49**, 891-913.

RAWLING T.J., SCHAUBS P.M., DUGDALE L.J., WILSON C.J.L. & MURPHY F.C. this volume. Application of 3-D models and numerical simulations as a predictive exploration tool in western Victoria. *Australian Journal of Earth Sciences*.

SCHAUBS P.M., RAWLING T.J., DUGDALE L.J., WILSON C.J.L. this volume. Factors controlling the location of gold mineralisation around basalt domes in the Stawell corridor: insight from 3-D deformation – fluid-flow numerical models. *Australian Journal of Earth Sciences*.

VANDENBERG A. H. M., WILLMAN C.E., MAHER S., SIMONS B. A., CAYLEY R. A., TAYLOR D. H., MORAND, V. J., MOORE D. H. & RADOJKOVIC A. 2000. The Tasman Fold Belt System in Victoria. *Geological Survey of Victoria Special Publication*. East Melbourne, Victoria, pp. 462.

Chapter 6 : Structural transect and forward modelling of geophysical data across the St Arnaud Group, Victoria.

L.D. Leader, T.J. Rawling and C.J.L.Wilson

Summary

The integration of detailed field mapping with 2.75-D forward modelling and worming of potential field datasets has constrained the 3-D geometry of regionally significant faults and allowed a detailed understanding of the crustal scale architecture of the St Arnaud Group in the Stawell Zone. The forward modelling has also highlighted the existence of a major west-dipping, non-outcropping fault, the Burrom Fault, between the Concongella and Landsborough Faults. The structure of the upper crust is characterised major reverse faults. These faults originate from a basal décollement that is located within mafic volcanics underlying the St Arnaud Group. Deformation has resulted in slices of these mafic volcanics being ramped up along the traces of the major faults.

Introduction

The St Arnaud Group of sediments in the Stawell Zone extends from the Coongee Fault to the Avoca Fault and consists of folded and faulted quartz-rich Cambrian turbidites (Miller et al. this volume). On the basis of sand to silt ratios, the St Arnaud Group is subdivided into the Warrak, Beaufort and Pyrenees Formations (Cayley & McDonald 1995; Cayley & Taylor 2001). The Warrak Formation extends from the Coongee Fault to the west-dipping Landsborough Fault and is dissected by the east-dipping Concongella Fault (Figure 6-1). The Beaufort Formation outcrops to the east of the Landsborough Fault and has been faulted against the Pyrenees Formation by the west-dipping Percydale Fault (Cayley & McDonald 1995; Cayley & Taylor 2001). The grade of metamorphism to the east of the Coongee Fault, a reverse fault dipping approximately 45∞ west, is low greenschist facies, with higher metamorphic grade rocks of the Moornambool Metamorphic Complex to the west (Phillips et al. 2002).

In this region of Western Victoria there is a poor preservation of the St Arnaud Group and the crustal architecture underlying this sequence remains unknown. It has been suggested that there is mafic crust beneath the St Arnaud Group and slices of this mafic crust have been ramped up along faults during east-west compression events (Cayley & McDonald 1995; Cayley & Taylor 2001). It has also been suggested that underlying this mafic crust is Proterozoic meta-sediments and ultramafic crust (Cayley & Taylor 2001; Miller et al. in press).

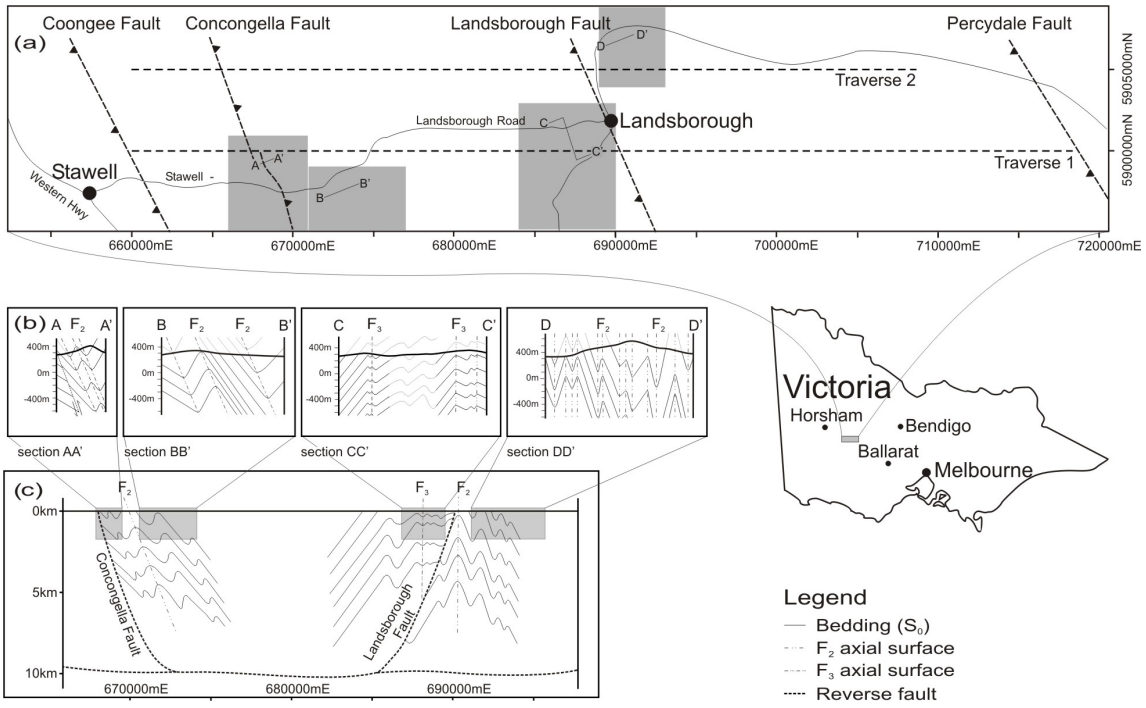

Figure 6-1: Location and crustal profiles through the Stawell Zone. (a) Trace of the Landsborough and Concongella Faults, the east-west transects (dashed lines) and areas where detailed structural data was collected (shaded grey). (b) Structural sections AA', BB', CC' and DD'. (c) Regional scale cross section, from the Concongella Fault to the east of the Landsborough Fault at a northing of 5900000mN. Sections AA', BB', CC' and DD' have been moved parallel to strike for this interpretative section. Vertical exaggeration = 1.36.

In this paper structural and lithological mapping of the St Arnaud Group (Figure 6-1b) has been used to construct a regional scale transect from the Concongella Fault to the east of the Landsborough Fault (Figure 6-1c). This regional scale east-west transect was then used to constrain the geometry for 2.75-D geophysical forward modelling to provide a better understanding of the crustal structure in an area of poor outcrop. We constrain the geometry of the section using interpretation and forward modelling of potential-field datasets.

Structure in transect

The Concongella Fault strikes northwest - southeast and dips steeply towards the northeast (Figure 6-1). The Landsborough Fault also strikes northwest-southeast but dips steeply towards the southwest. The first deformation event (D1) can be observed within the hanging-walls of the Concongella and Landsborough Faults as a bedding parallel cleavage. In the hanging-wall of the Concongella Fault S2 is the dominant fabric that is related to F2 folds. A third deformation event (D3) was only observed in the hanging-wall of the Landsborough Fault. The intensity of these D3 structures decreases westward away from the Landsborough Fault with only a single deformation event observed west of section CC' (Figure 6-1b).

The Concongella Fault is a high-strain zone (section AA' Figure 6-1b) located in an east-dipping limb of a regional scale F2 fold. The Concongella and Landsborough Faults probably originate from a basal décollement at a depth of approximately 10 km. It is interpreted that this basal décollement is located within the mafic volcanics

that underly the St Arnaud Group sediments (Vandenberg et al. 2000, Cayley & Taylor 2001, Gray et al. 2003, Miller et al. submitted).

Sections CC' and DD' (Figure 6-1b) show F3 folds with a sub-vertical axial surface folding bedding and a bedding parallel cleavage (S1). As the bedding and cleavage is dominantly west-dipping; then the F3 folds are believed have formed in a west-dipping limb of a regional scale F2 fold. Further evidence supporting this is that beyond the high-strain zone associated with the Landsborough Fault the S1 cleavage remains parallel to bedding that continues to dip towards to the west. Due to the lack of outcrop to the west, it is not possible to determine any change in the orientation of the bedding and cleavage or infer the wavelength and amplitude of this regional scale F2 fold.

Section DD' (Figure 6-1b) lies within the footwall of the Landsborough Fault and shows that the enveloping surface of the folds is sub-horizontal and is located in the hinge zone of a regional scale fold. Although the trace of the enveloping surface of these folded sediments is sub-horizontal, it increases in elevation towards the west implying that the regional scale fold is an anticline. The inferred amplitude of these regional scale folds is approximately 5 km with a wavelength of approximately 10 km.

Modelling of Gravity and Magnetic Data

Gravity and magnetic data was forward modelled using the GM-SYS modelling software (Northwest Geophysical Associates, 2004) in order to test the validity and to extend the depth of the interpretative crustal scale cross section (Figure 6-1c). GM-SYS is a two and three quarter dimensional software program that allows the geometry of rocks to be constrained by their geophysical response. The forward modelling process involves the construction of a geological cross section, constrained by field observations, and calculating a geologically constrained anomaly of the cross section and comparing this to the observed anomaly derived from the potential field data (e.g. McLean & Betts 2003). The potential field data (Figure 6-2) was extracted for two east west oriented transects, 660000mE 5900000mN to 720000mE 5900000mN (Traverse 1 in Figure 6-1a) and 660000mE 5905000mN to 700000mE 5905000mN (Traverse 2 in Figure 6-1b), from the VIMP airborne magnetic and Bouguer gravity data-set grids (Moore, 2003). The airborne magnetic survey was flown east west with a line spacing of 250 m and a sample spacing of 20 m. The gravity ground-survey was conducted by the Geological Survey of Victoria at a nominal 1.5 km station spacing and has been Bouguer corrected to remove the effects of topography (Moore, 2003). The regional scale cross section (Figure 6-1c) was used as a basis for this modelling. For the purposes of modelling, the regional scale signatures were edited so that they only extended from 660000mE to 716000mE (Figure 6-2).

Models in GM-SYS are built using polygons that represent different rock types and are assigned rock property data such as density and magnetic susceptibility (Table 6-1). Magnetic remanence values can also be assigned to polygons, however, the magnetic remanence of the St Arnaud Group sediments is poorly understood. This means that some of the rock units have been assigned a negative magnetic susceptibility to approximate the effect of remanent magnetisation. Once the densities

and magnetic susceptibilities have been assigned, GM-SYS calculates the geophysical response.

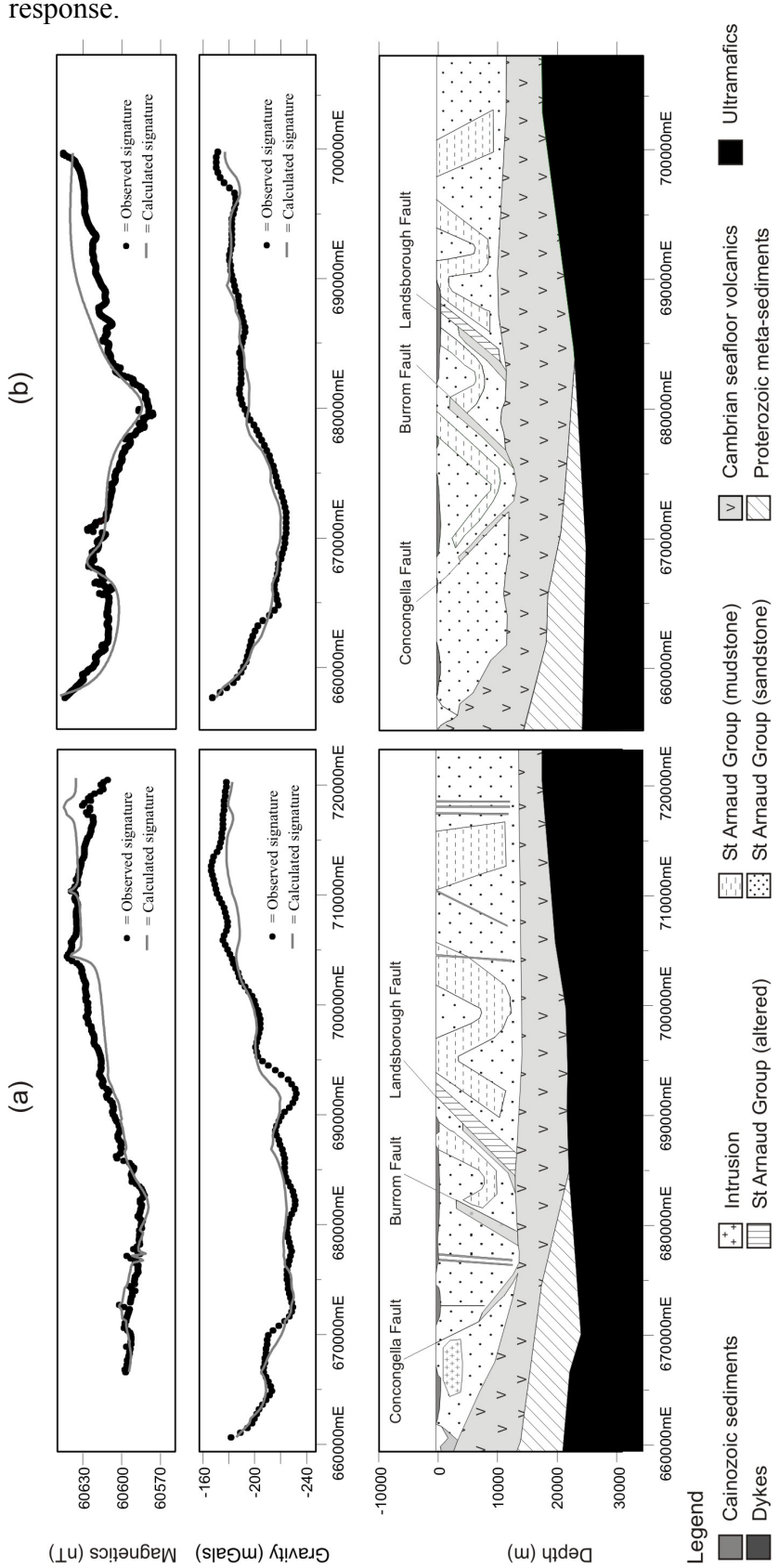

Figure 6-2: The observed and calculated magnetic and gravity signatures and the interpretative geological cross-sections constructed with GM-SYS. (a) 5900000mN east-west transect. (b) 5905000mN east-west transect. Vertical exaggeration = 0.55.

This can then be compared with the observed geophysical response. The calculated response changes in real time as the model is varied so that the effects of geometrical changes to the polygons and the rock properties associated with them can be easily and quickly observed.

The gravity and magnetic data was also 'wormed' (Archibald et al. 2001) where a wavelet analysis (an alternative to Fourier analysis) was used to detect edges, at different heights above the source of the anomalies, in two-dimensional images of potential field data (Hornby et al. 1999). If the wavelet-scale (different heights above the source) is used to represent the third dimension, then 2-D edges form surfaces (Archibald et al. 1999) that describe how the magnetic and gravity responses of geological bodies change with depth (Murphy & Lees 2004). The shapes of these surfaces represent the subsurface locations of contacts between bodies of different magnetic susceptibility and density, and can therefore be used to delineate the geometries of the geological structures (Archibald et al. 1999).

Rock Type	Density range. (Kg / m^3)	Magnetic susceptibility range. (SI units)
Cainozoic sediments	1800-2400	1×10^{-6}
Intrusion	2900	1000×10^{-6}
St Arnaud Group (sandstone)	2550-2650	10×10^{-6}
St Arnaud Group (mudstone)	2700-2800	10×10^{-6}
St Arnaud Group (altered)	2350	10×10^{-6}
Mafic Dykes	3100	$2000 - 5000 \times 10^{-6}$
Mafic volcanics	3100	$10000 - 20000 \times 10^{-6}$
Proterozoic meta-sediments	2850	10×10^{-6}
Ultramafics	3500	10000×10^{-6}

Table 6-1: Density and magnetic susceptibility values used for the GM-SYS models. These data were obtained from Cayley & Taylor (2001), McDonald & Whitehead (1996), Telford *et al.* (1976) and from field measurements.

Modelling results

The results of the models are shown in Figures 6-2 and 6-3. Geological components, faults and different lithologies, of both the models are discussed separately.
Field observations determined that along traverse 2 the Concongella Fault is at a position of 669000mE. This position corresponds with two positive asymmetric magnetic anomalies that have an amplitude of 6 nT (Figure 6-2b). Along traverse 1 the location of the Concongella Fault coincides with an observed positive gravity anomaly between 664500mE and 670000mE (Figure 6-2a) has an amplitude of 15 mgals. These observed gravity and magnetic anomalies were modelled as a mafic body that has been ramped up along the trace of the fault.

The Landsborough Fault does not outcrop in the field but its inferred position on traverses 1 and 2 coincide with negative gravity anomalies. Between 688500mE and 691700mE on traverse 1 (Figure 6-2a), a negative gravity anomaly with a half

wavelength of 3200 m and amplitude of 22 mgals matches the inferred position of the Landsborough Fault. This negative gravity anomaly represents material of a lower density and can be modelled by a 1500 m wide alteration zone in the footwall of the Landsborough Fault. This alteration zone is postulated from analogies with other faults in western Victoria where there has been extensive sericite-carbonate alteration (Dugdale *et al.* this volume). This alteration zone would extend to the same depth as the fault and has been assigned a density of 2400 kg/m^3.

Along traverse 2, the inferred position of the Landsborough Fault matches a negative symmetric gravity anomaly with a half wavelength of 3 km and amplitude of 10 mgals between 685000mE and 688000mE (Figure 6-2b). This anomaly also represents a low density material and can be modelled by Cainozoic sediments that overly the Landsborough Fault. The Cainozoic sediments have a density range of 2100 – 2300 kg/m3, which is lower than the density range of the surrounding sediments of the St Arnaud Group (2600 – 2700 kg/m^3) thus contributing to the observed negative gravity anomaly.

The Landsborough Fault also coincides with asymmetric, east verging, positive and negative magnetic anomalies that have half wavelengths of 800 m and amplitudes of 10 nT (Figure 6-2b). The vergence of these magnetic anomalies suggests that there is a magnetic body that dips to the west. A good correlation between the observed and calculated signatures was obtained when these anomalies were modelled as resulting from a slice of mafic material that have been ramped up along the trace of the Landsborough Fault (Figure 6-2). This mafic body that would extend from a depth of 3 km to 12 km, has been assigned a density of 3100 kg/m^3 and a magnetic susceptibility of -10000 x 10^{-6} (SI units).

Figure 6-2 shows a third fault, the Burrom Fault (Moore 2003), between the Concongella and Landsborough Faults. The Burrom Fault does not outcrop in the field but was incorporated into the models to account for the most notable feature of the observed magnetic signature along traverse 2 (Figure 6-2b), a broad asymmetric negative magnetic anomaly between 672300mE and 685300mE. This magnetic anomaly verges to the east, has an amplitude of 40 nT, a half wavelength of 12 km and is overprinted by smaller scale asymmetric positive and negative anomalies that verge both to the east and the west. The smaller scale magnetic anomalies have an average half wavelength of 300 m and amplitude of 5 nT. The broad negative anomaly was modelled as a west dipping reverse fault with a mafic body that has been ramped up along the surface of the fault. The mafics were modelled to be approximately 600 m thick, extending from a depth of 2 km to 12 km and have been assigned a density of 3100 kg/m^3 and a negative magnetic susceptibility of -15000 x 10^{-6} (SI units) to compensate for remanence.

The existence of the Burrom Fault can be confirmed by modelling the St Arnaud Group without the fault (Figure 6-3a). In this case there is a poor correlation between the observed and calculated gravity and magnetic signatures. The wormed data sets (Figure 6-4) also show evidence for the existence of the Burrom Fault.

The dip direction of the Burrom Fault is speculative because conflicting dip directions arise from different data-sets. The asymmetry of the anomaly along traverse 2 across the Burrom Fault (Figure 6-2b) suggests a westerly dip. The orientations of the

gravity and magnetic worms (Figure 6-4) are ambiguous because they can be interpreted as representing either an east-dipping or west-dipping fault. Moore (2003) inferred that the Burrom Fault dips towards the east based upon the offset of magnetic marker beds within the St Arnaud Group sediments.

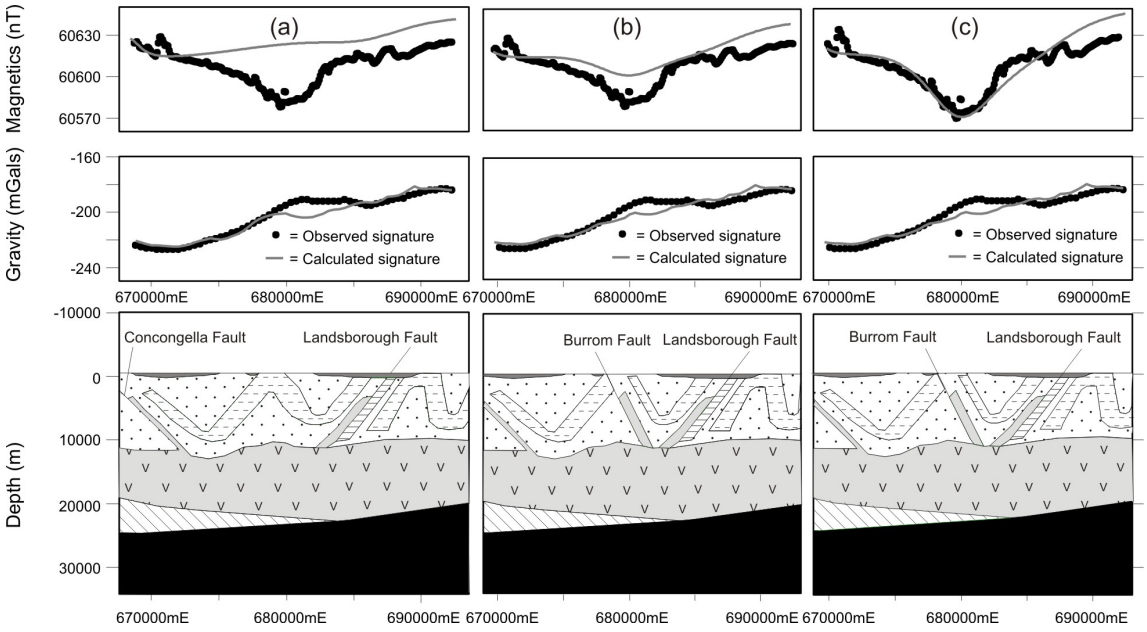

Figure 6-3: Alternative models of the geophysical data support the conclusion that the Burrom Fault exists and is a west-dipping fault. Refer to Figure 6-2 for legend. (a) When the magnetic and gravity data is modelled without the fault there is a relatively good correlation between the observed and calculated gravity signatures but a very poor correlation between the observed and calculated magnetic signatures, therefore the presence of the fault is implied by the observed magnetic signature. (b) Burrom Fault modelled as an east-dipping fault results in a relatively poor correlation between the amplitude of the observed and calculated magnetic anomaly. (c) Burrom Fault modelled as an east-dipping fault results in a relatively good correlation between the observed and calculated gravity and magnetic signatures when the mafic volcanics along the trace of the fault are assigned a magnetic susceptibility of –40000 x 10^{-6} (SI units). Vertical exaggeration = 0.55.

When the Burrom Fault is modelled as an east-dipping fault (Figure 6-3b) the amplitude of the calculated magnetic anomaly does not correlate with the amplitude of the observed magnetic anomaly. This poor correlation may be due to remanence. To account for this the mafic bodies along the trace of the fault were modelled with a higher magnetic susceptibility (-40000 x 10-6 SI units) (Figure 6-3c) resulting in a good correlation between the observed and calculated magnetic anomalies. However, a magnetic susceptibility of this magnitude is unreasonable, as the mafics that are associated with the Landsborough and Concongella Faults were assigned a magnetic susceptibility of 10000 x 10-6 (SI units). Further evidence that suggests a magnetic susceptibility of this magnitude is unreasonable is that along traverse 1 (Figure 6-2a) a good correlation between the observed and calculated magnetic signatures was obtained when the mafics associated with the Burrom Fault were assigned a magnetic susceptibility of 10000 x 10-6 (SI units). It is unlikely that there would be a large variation in magnetic susceptibility over such a short distance.

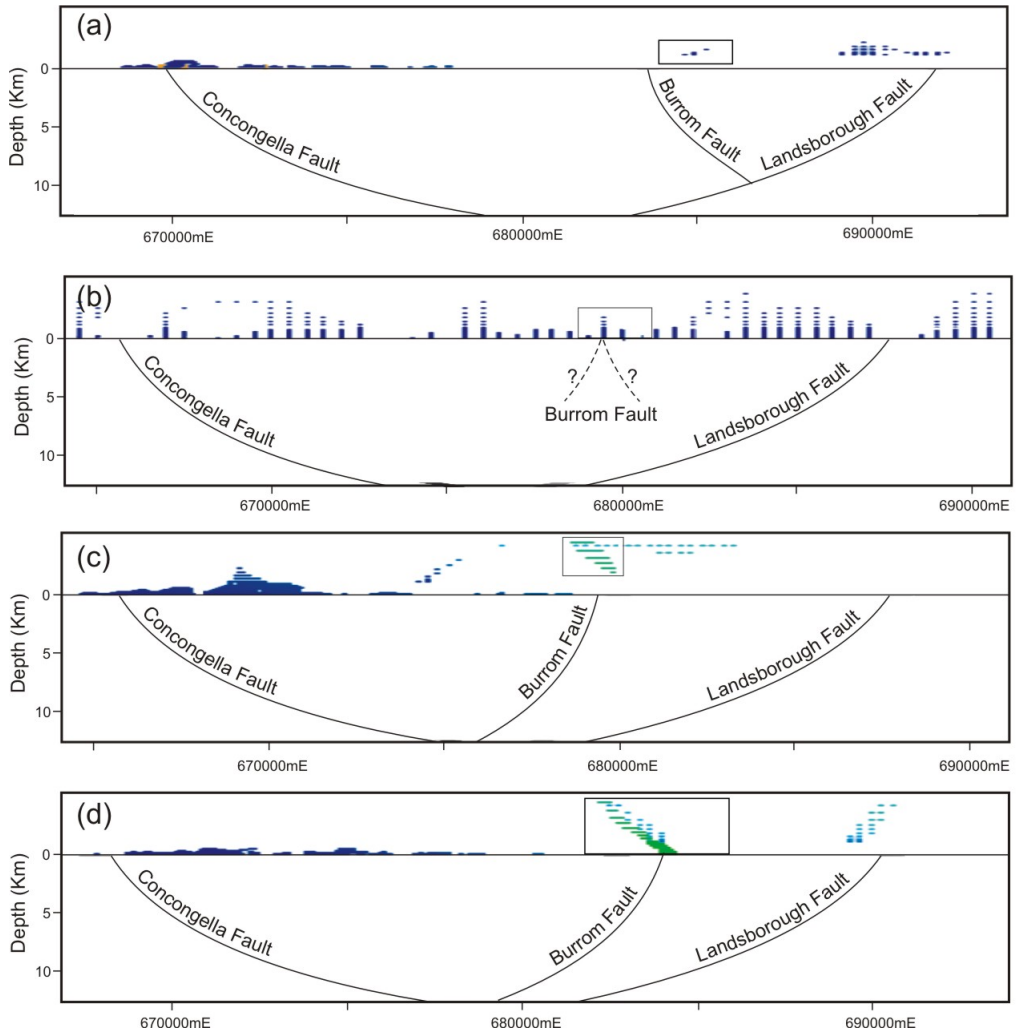

Figure 6-4: (a) Magnetic worms from an east west transect at 5895000mN. The magnetic worms that are outlined by a black square imply that the Burrom Fault dips towards the east. (b) Gravity worms from an east west transect at 5905000mN. The gravity worms that are outlined by a black square give no indication of the dip direction of the Burrom Fault. (c) Magnetic worms from an east west transect at 5905000mN. The magnetic worms that are outlined by a black rectangle imply that the Burrom Fault dips towards the west. (d) Magnetic worms from an east west transect at 5910000mN. The magnetic worms that are outlined by a black rectangle imply that the Burrom Fault dips towards the west. These sections are modified versions of wider sections from Murphy (written comm.). Vertical exaggeration = 0.33

Along traverses 1 and 2 (Figure 6-2) there are Cainozoic sediments overlying the St Arnaud Group sediments. The Cainozoic sediments were observed within low-lying regions of the field area. The location of these sediments coincides with the location of negative gravity anomalies such as the anomaly at 682000mE along traverse 1 (Figure 6-2a).

In Figure 6-2 there is a series of polygons that represent St Arnaud Group mudstones. These have been used to model some of the observed positive gravity anomalies of traverses 1 and 2. For example, adjacent to the negative gravity anomaly that was modelled as an alteration zone in the footwall of the Landsborough Fault (Figure 6-2a) is an asymmetric, positive gravity anomaly that has a half wavelength of 2400 m

and amplitude of 10 mgals. This anomaly verges to the west and was modelled as an east dipping, 3.5 km thick body that extends the entire depth of the St Arnaud Group. This body was assigned a density of 2750 kg/m3 and represents a package of sediment, with a higher mud content, and therefore higher density, than the surrounding sediments of the St Arnaud Group and may be an equivalent of the Leviathan Formation (Squire & Wilson 2005). The body traces out an east dipping limb of a regional scale syncline that has a wavelength of 16 km and amplitude of 12 km. Further east, at approximately 698000mE the west dipping limb of this regional syncline produces another asymmetric positive gravity anomaly with a half wavelength of 2000 m and amplitude of 10 mgals.

To the west of the Concongella Fault along traverse 1 (Figure 6-2a) there is a positive gravity anomaly that has a half wavelength of 4000m and amplitude of 10mgals. This gravity anomaly can be modelled by an intrusive body that has a magnetic susceptibility of 1000 x 10-6 (SI units) and a density of 2900 kg/m3. The average density ranges for granite and diorite are 2500 - 2800 kg/m3 and 2720 -2990 kg/m3 (Telford et al. 1976). Therefore it is proposed that the modelled intrusive body is a composite intrusion consisting of granite and diorite. This is analogous to the relationship between the Ararat granodiorite and the Curtis diorite in which the diorite is interpreted to be an early intrusive phase (Cayley & Taylor, 2001).

Mafic dykes were observed in the field and have been incorporated into the model. Short wavelength magnetic anomalies at 672500mE, 677300mE and 704500mE can be modelled by mafic dykes that have intruded the St Arnaud Group sediments.

Cambrian seafloor volcanics, the Magdala Basalt (Wilson et al. 1992), have been observed at Stawell. An excellent correlation between the observed and calculated gravity and magnetic signatures was obtained when the top of the Cambrian volcanic unit was interpreted to extend through traverses 1 and 2 at a depth of approximately 10 km (Figure 6-2).

A unit of Proterozoic meta-sediments extending from the west to approximately 680000mE at a depth of 20 km (Figure 6-2) is based on the model of Miller et al. in press) and was assigned a density of 2850 kg/m3. If this unit, which has a lower density and magnetic susceptibility than the overlying Cambrian seafloor volcanics, was not incorporated into the model then there would be a poor correlation between the observed and calculated gravity and magnetic signatures.

Conclusions

The potential field modelling results were consistent with the regional scale structural mapping and provided evidence for the existence of a major crustal scale fault between the Landsborough and Concongella Faults. This fault has been previously recognised and termed the Burrom Fault (Moore 2003). The magnetic and gravity worm data associated with this fault implies that the fault dips towards the west and the east and therefore cannot be used to infer the dip direction of the fault. The modelling presented in this paper implies that the Burrom Fault dips towards the west (Figure 6-5). Moore (2003) inferred that the Burrom Fault dips towards the east based upon the offset of magnetic marker beds within the St Arnaud Group sediments.

The magnetic and gravity anomalies associated with the major faults can be modelled by mafic volcanic slices that have been ramped up along the faults during deformation.

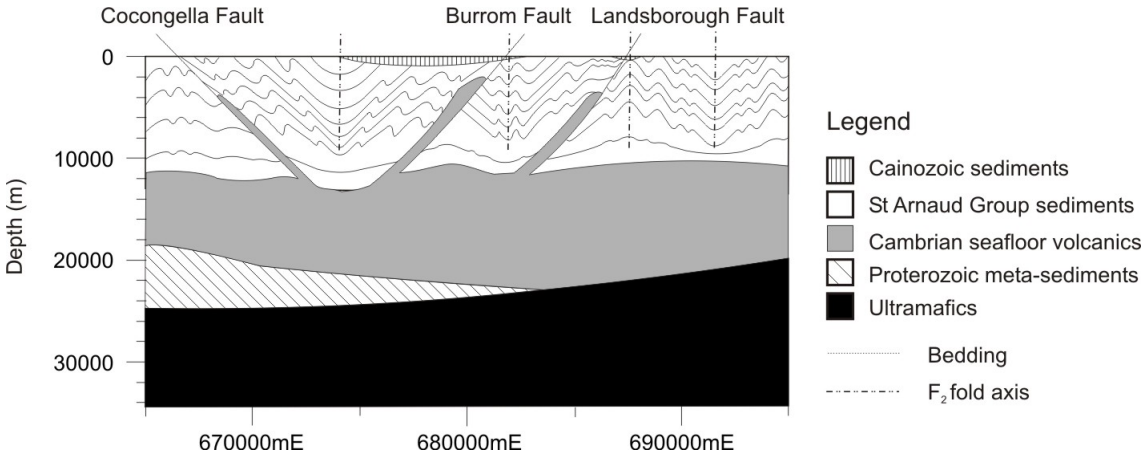

Figure 6-5: Crustal scale cross section that combines the field observations and the results of the potential field forward modelling. This figure shows that the folded St Arnaud Group sediments have been faulted by crustal scale reverse faults that extend from a basal décollement within mafic volcanics at a depth of 10-12km. Mafic volcanics that lie above the basal décollement have been ramped up along the reverse faults. Vertical exaggeration = 0.47

Modelling of the potential field data of the St Arnaud Group sediments has also implied that there is a folded package of sediments with a higher mud content contained within the sequence of these sediments. These results have led to a greater detailed understanding of the 3-D geometry of a poorly exposed region that is adjacent to a major gold bearing belt in western Victoria.

References

ARCHIBALD N., GOW P. & BOSCHETTI F., 1999. Multiscale edge detection analysis of potential field data. *Exploration Geophysics,* **30**, 38-44.

ARCHIBALD N., HOLDEN D., MASON R., POWER B., BOSCHETTI F., HOROWITZ F., & HORNBY P., 2001. "There's a Worm in my Soup": Wavelet based Analysis for Interpretation of Crustal Scale Potential Field Datasets and Implications for Identification of Giant Hydrothermal Ore Systems. *2001 – A Hydrothermal Odyssey: Townsville May 17-19, 2001. James Cook University EGRU.*

CAYLEY R.A. & MCDONALD P.A., 1995. Beaufort 1:100 000 map geological report. *Geological Survey of Victoria Report 104.*

CAYLEY R.A. & TAYLOR D.H., 2001. Ararat 1:100 000 map area geological report. *Geological Survey of Victoria Report 115.*

DUGDALE A.L.& WILSON C.J.L. Hydrothermal alteration of an atypical turbidite-hosted orogenic gold deposit: the Magdala system, Stawell, western Victoria. *Australian Journal of Earth Sciences.* Submitted.

GRAY D.R., FOSTER D.A., MORAND V.J., WILLMAN C.E., CAYLEY R.A., SPAGGIARI C.V., TAYLOR D.H., GRAY C.M., VANDENBERG A.H.M., HENDRICKX M.A. & WILSON C.J.L., 2003. Chapter 2: Structure, metamorphism, geochronology, and tectonics of Palaeozoic rocks. *In* Birch, W.D. (ed.) Geology of Victoria. *Geological Society of Australia Special Publication 23. Geological Society of Australia (Victoria Division),* 15-71.

HORNBY P., BOSCHETTI, F. & HOROWITZ, F. 1999. Analysis of potential field data in the wavelet domain. *Geophysical Journal International*, **137**, 175-196.

MCDONALD, P.A. & WHITEHEAD, M.L. 1996. Geological interpretation of geophysical data over the Ararat 1:100 000 map sheet. *Victorian Initiative for Minerals and Petroleum Report 38.* Department of Natural Resources and Environment.

MCLEAN M.A. & BETTS P.G. 2003. Geophysical constraints of shear zones and geometry of the Hiltaba Suite granites in the western Gawler Craton, Australia. *Australian Journal of Earth Sciences,* **50,** 525-541.

MILLER J.MCL., PHILIPS D., WILSON C.J.L. & DUGDALE L.J., IN PRESS. Evolution of a reworked orogenic zone: the boundary between the Lachlan and Delamerian Orogens, SE Australia. *Australian Journal of Earth Sciences.*

MURPHY B. & LEES T., 2004. Habitat of Yilgarn gold – from fault and worm analysis. *Predictive mineral Discovery CRC Conference Abstracts, Barossa Valley 1-3 June 2004.*

MURPHY B. (personal communication). Supply of 'wormed' data sections.

MOORE D.H., 2003. St Arnaud 1:250000 map: a geological interpretation of the geophysical data. *Victoria Initiative for Minerals and Petroleum, Report 8x. Department of Primary Industries, Victoria.*

NORTHWEST GEOPHYSICAL ASSOCIATES, 2004. GM-SYS is developed by Northwest Geophysical Associates (NGA).

PHILIPS G., MILLER J.MCL. & WILSON C.J.L., 2002.Structural and metamorphic evolution of the Moornambool Metamorphic Complex, western Lachlan Fold Belt, southeastern Australia. *Australian Journal of Earth Sciences,* **49**, 891-913.

SQUIRE R.J. & WILSON C.J.L., 2005. Tectonic responses to super-continent formation: correlation of Cambrian geological events along the proto-Pacific margin of East Gondwana. *Journal of the Geological Society, London*, **162**, 1-13.

TELFORD W.M., GELDART L.P., SHERIFF R.E. & KEYS D.A., 1976. Applied Geophysics.

VANDENBERG, A.H.M, WILLMAN, C.E., MAHER, S., SIMONS, B.A., CAYLEY, R.A., TAYLOR, D.H., MORAND, V.J., MOORE, D.H., & RADOJKOVIC, A., 2000. The Tasman Fold Belt System in Victoria. *Geological Survey of Victoria Special Publication.* East Melbourne, Victoria, pp. 462

WILSON C.J.L., WILL T.M., CAYLEY R.A., & CHEN S., 1992. Geologic framework and tectonic evolution in Western Victoria. *Tectonophysics,* **214**, 93-127.